ABSTRACT

ALOMARI, ABDULLAH SAUD. Serrated Yielding and Creep Properties of an Advanced Austenitic Stainless Steel (Alloy 709) – Application to Next Generation Sodium Fast Reactors. (Under the direction of K. L. Murty).

Advanced structural materials are needed for next-generation Sodium Fast Reactors (SFR) to withstand higher operating temperatures, enable longer lifetimes and improve the safety, flexibility, and economics as well. Alloy 709, an advanced austenitic stainless steel with base Fe-20Cr-25Ni (wt.%), is an excellent candidate for SFR structural material due to desired set of properties relative to other conventional stainless steels. However, significant degradation of mechanical properties may occur due to serrated yielding associated with solute-dislocation interactions. In addition, understanding the rate controlling creep mechanisms for such newly developed stainless steel is essential not only for predicting the life of the Alloy 709 but also for developing more creep-resistant microstructures.

To understand micromechanics of plastic deformation in the Alloy 709, uniaxial tensile tests were carried out at temperatures ranging from 298 – 1073 K and nominal strain rates from $10^{-5} - 10^{-3}$ s^{-1} followed by microstructure evaluation. The alloy exhibited serrated yielding, a manifestation of dynamic strain aging (DSA), in two temperature regimes; low-temperature serrated flow (LT-SF) from 498 to 648 K and high-temperature serrated flow (HT-SF) from 648 to 973 K. Different methods were employed for the determination of activation energy of the serrated flow that yielded values of 103 ± 13 kJ/mole and 204 ± 11 kJ/mole for the LT-SF and HT-SF regimes, respectively. Within the LT-SF and HT-SF regimes, the serrations were observed to commence only after a critical amount of plastic strain, ε_c that was found to decrease as temperature increases and increase as strain rate increases. The dependence of the strain rate on the ε_c followed an exponential function with an exponent $(m + \beta)$ of 0.78 ± 0.1

and 1.56 ± 0.2 for the LT-SF and HT-SF regimes respectively. Based on the activation energy values and the exponents $m + \beta$, diffusion of interstitial atoms such as nitrogen and/or carbon has been suggested to be responsible for serrated flow in the LT-SF regime while the diffusion of substitutional atoms such as Cr is responsible for serrations in the HT-SF regime. During serrated follow regimes, peaks and/or plateaus in flow stresses, negative strain rate sensitivity, increase in work hardening rates and planar substructure are noted and considered as other manifestations of the DSA. Contrary to the commonly observed embrittlement during dynamic strain aging, a distinct enhancement in ductility is observed in the Alloy 709 at intermediate temperatures where serrated flow is noted. This observation was rationalized based on of the influence of strain hardening parameters and strain rate sensitivity on uniform elongation and ductility, respectively. Further, the fraction of low angle grain boundaries for the deformed samples exhibits a valley at intermediate temperatures believed to be another manifestation of the DSA.

Additionally, creep tests were performed in the Alloy 709 at temperatures ranging from $973 - 1073$ K and $40 - 275$ MPa followed by microstructural characterization. The apparent stress exponent and activation energy were determined to be 6.81 ± 0.4 and 421 ± 38 kJ/mole respectively. Crept samples showed three types of precipitates identified as Nb(C, N), and Z-phases of sizes between $20 - 200$nm within the matrix and $M_{23}C_6$ with sizes between $200 - 700$ nm within the matrix and on grain boundaries. The concept of threshold stress was invoked to rationalize the higher activation energy comparing to that of lattice self-diffusion in Fe-25Ni-20Cr steels. Using a linear extrapolation method, threshold stresses were estimated to be 42.7 ± 10.2 MPa, 33.6 ± 2.4 MPa and 17.2 ± 1.9 MPa at 973 K, 1023 K and 1073 K respectively. The true stress exponent and activation energy after application of threshold

stresses were found to be 4.9 ± 0.2 and 299 ± 15 kJ/mole, respectively. Therefore, together with the microstructural evidence, the rate-controlling mechanism in the Alloy 709 was conclusively determined to be the high-temperature dislocation climb. Further, creep rupture tests at higher stresses (> 100 MPa) in the Alloy 709 were analyzed in terms of Larson-Miller parameter, Monkman–Grant and modified Monkman–Grant relationships and display a high creep damage tolerance factor of ~ 5. Considering the Larson-Miller parameter, the Alloy 709 exhibits superior creep strengths relative to the other advanced austenitic steels.

المنارة للاستشارات

www.manaraa.com

Serrated Yielding and Creep Properties of an Advanced Austenitic Stainless Steel (Alloy 709) – Application to Next Generation Sodium Fast Reactors

by
Abdullah Saud Alomari

A dissertation submitted to the Graduate Faculty of
North Carolina State University
in partial fulfillment of the
requirements for the degree of
Doctor of Philosophy

Nuclear Engineering

Raleigh, North Carolina

2019

APPROVED BY:

_____   _____
Dr. K. L. Murty   Dr. Jacob Eapen
Committee Chair

_____   _____
Dr. Mohammed Bourham   Dr. Ronald Scattergood

DEDICATION

To
Saud: father and son.
Saffia: mother and daughter.
Alwa: wife.
Leen and Layan: twin daughters.

BIOGRAPHY

Abdullah Alomari was born in Bani Assem, a village located in Al-Bahah region in Saudi Arabia in 1987. He had his schoolings until 12th grade in Mecca, Saudi Arabia. Abdullah graduated from Umm Al-Qura University with Bachelor degree of Electrical Engineering in 2009 with second honors. During his Bachelor, he went to many internship and fellowship programs such as Saudi Oil Company (Aramco), Saudi Electricity Company and International Atomic Energy Agency (IAEA). In 2010, Abdullah joined the Atomic Energy Research Institute for academic research in King Abdulaziz City for Science and Technology (KACST) in Riyadh, Saudi Arabia. He then continued his higher education in nuclear engineering where he earned his Master degree in Nuclear Engineering from Missouri University of Science and Technology in Rolla, Missouri in 2012. After that, Abdullah went to Argentina for fellowship with INVAP Company for six months to participate on designing a neutron imaging facility of a low power research reactor. In 2013, Abdullah joined the department of nuclear engineering at North Carolina State University for a PhD program. He then joined nuclear material group under guidance of Dr. K. L. Murty and worked towards his PhD on high temperature mechanical properties for structural materials of next-generation nuclear reactors.

ACKNOWLEDGMENTS

All thanks and praises to God (ALLAH) for providing me with the power and patience to have this work accomplished.

My heartfelt gratitude goes to my PhD advisor Prof. K. L. Murty for his invaluable support, encouragement and guidance. I am deeply grateful for his advices that enlightened me to explore, present and publish scientific works. His contentious supervision and supportive remarks have paved the way for me towards my future scientific contributions. It was an honor to pursue my PhD under the direction of Prof. Murty.

My gratitude and appreciation are also extended to the committee members: Prof. Jacob Eapen, Prof. Mohamed Bourham, and Prof. Ronald Scattergood for their invaluable time, helpful discussion and constructive feedback.

Special thanks to Dr. Nilesh Kumar (now an assistant professor at the University of Alabama) for his assistance, useful guidance and persistent help that were crucial to get this work completed.

I also would like to thank several colleagues, friends and staff who supported and helped me at various stages throughout my time at NC State University; Xiaotian Fang, Yassir Abdalla, J. D. Ellisor, Ervin Miller, Chris Sanford, Emad Tawardrous, Qingsheng Cai, to name a few . Thanks are also given to those people whose names are not listed but provide a great help through my PhD study. Financial support from the Government of Saudi Arabia represented by King Abdulaziz City for Science and Technology (KACST) for funding my PhD degree is also fully acknowledged.

This work is a product of a lot of love and sacrifice made by all my family members here and abroad. No enough words are exist to be expressed towards my parents; Saud and

TABLE OF CONTENTS

LIST OF TABLES

LIST OF FIGURES

DISSERTATION OVERVIEW

The primary objective of this research work is to elucidate the serrated yielding and creep properties in a Fe-20Cr-25Ni (wt.%) advanced austenitic stainless steel (Alloy 709), which is a candidate structural material for next-generation Sodium-cooled Fast Reactor, by conducting a series of tensile and creep tests at various temperatures followed by microstructural evaluation.

Chapter 1 firstly give a brief introduction about the next generation Sodium Fast Reactors and the importance of developing advanced structural materials for such reactor systems. Following that, a short description of the advanced austenitic stainless steel (Alloy 709) and the motivation for conducting this study are mentioned.

 Chapter 2 starts with a concise definition about the austenitic stainless steels along with their major alloying elements and common precipitates found in advanced austenitic stainless steels. Then, a background related to the serrated yielding, various models for the serrated flow and the impact of serrations on the mechanical properties are presented and followed by extensive literature survey about the serrated yielding in austenitic stainless steels. Flowing that, general description about creep and the creep mechanisms are reported followed by a comprehensive review of the creep behavior in austenitic stainless steels.

Chapter 3 is dedicated for describing the material and experimental procedure for mechanical and microstructural examination employed in this study including tensile tests, creep tests, transmission electron microscopy, and electron backscatter diffraction technique.

Chapter 4 is focused on the serrated yielding behavior for the Alloy 709 where characteristics of serrations, activation energy, and associated mechanisms for the serrated flow, the influence of the serrated yielding on the tensile properties and the microstructures are

presented and discussed. This chapter is published in journal of *Materials Science and Engineering: A*.

Chapter 5 provides detailed results and discussions regarding creep behavior and microstructural evolution of the Alloy 709 at elevated temperatures. It includes initial microstructure, creep curves and minimum creep rate properties, microstructural examination of crept samples and creep rupture properties of the Alloy 709. This chapter is published in journal of *Metallurgical and Materials Transactions A*.

Chapter 6 concludes the general remarks regarding the serrated yielding and creep properties obtained in the Alloy 709. This chapter will end with the future works intended to be conducted on the Alloy 709 including fracture toughness in the dynamic strain aging regime and creep-fatigue interaction properties.

The dissertation is also tailed with four appendices. Appendix A shows the list of selected presentations and publications given by the author during his Ph.D study. In Appendix B, a short communication published in *Mater. Sci. Eng. A* about the ductility enhancement in dynamic strain aging in the Alloy 709 is impeded. Two published papers regarding the creep-fatigue properties in the Alloy 709 are given in Appendix C and Appendix D.

1. INTRODUCTION

Among the six Generation-IV (Gen-IV) nuclear reactor designs chosen over others for further research and development by Gen-IV International Forum (GIF), Sodium-cooled Fast Reactor (SFR) has the highest technology readiness level for deployment due to vast worldwide experiences gained over past decades [1]. A diagram of a typical SFR design is shown in Figure 1.1. As the name implies, SFR uses sodium (in the liquid phase) as a reactor coolant and fast neutron spectrum to induce nuclear fission and convert fertile material into fissile as well. Thus, SFR has a two-fold mission; the management of high-level wastes, in particular, management of plutonium and other actinides providing a closed fuel cycle, and electricity production supporting the needs of clean energy (no CO_2 emissions) with improved thermal efficiency [2, 3]. The main obstacles for not building commercial size SFRs in the past were the insufficient plant availability and high cost [3]. With the help of material research and development, advanced structural materials for SFR could withstand the harsh operating conditions allowing for enhanced plant efficiency and cost reduction [3].

Austenitic stainless steels are extensively utilized in both conventional and nuclear power plants owing to their excellent corrosion resistance and mechanical properties at elevated temperatures. In SFR applications, austenitic stainless steels have been widely considered as the major structural materials in the reactor core, reactor vessel, grid plate, sodium piping, primary heat exchangers, and sodium pumps etc. all over the world [4] attributed to their adequate high temperature mechanical properties, compatibility with liquid sodium coolant, better rupture strength and oxidation resistance [5]. However, advanced austenitic stainless steels are needed to withstand higher operating temperatures for longer service and to improve the safety, flexibility, and economics for SFRs [2, 6-8].
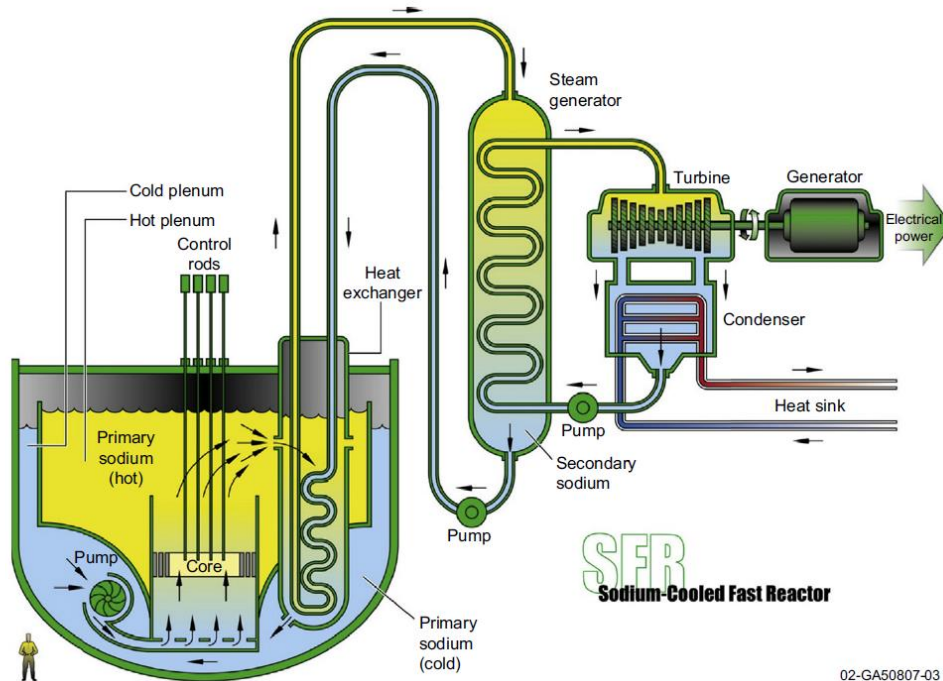
3

Figure 1.1. A schematic for a typical Sodium-cooled Fast Reactor [1].

The improvement of economics in the SFR could occur by reducing the commodities and the raw materials required for the same structural components through designing higher-strength materials or increasing the thermal efficiency by designing materials that operate at higher temperatures, assuming all other designing factors are still adequate [6, 7, 9]. For example, Busby [7] has shown that advanced austenitic stainless steels such as alloy D9 and high temperature ultra-fine precipitate steel (HT-UPS) can clearly impact the cost relative to the conventional stainless steel of type 316 by using thinner pipe wall as shown in Figure 1.2 [7], assuming a design temperature of 500 °C which is typical core outlet temperature for SFR. In addition, improved thermal efficiency could be obtained by increasing the reactor operating temperature. For example, an increase of about 150 °C is possible with no reduction in design stress in the case of HT-UPS relative to type 316 steel (Figure 1.2. [7]), assuming no other design factors or limitations intervene.
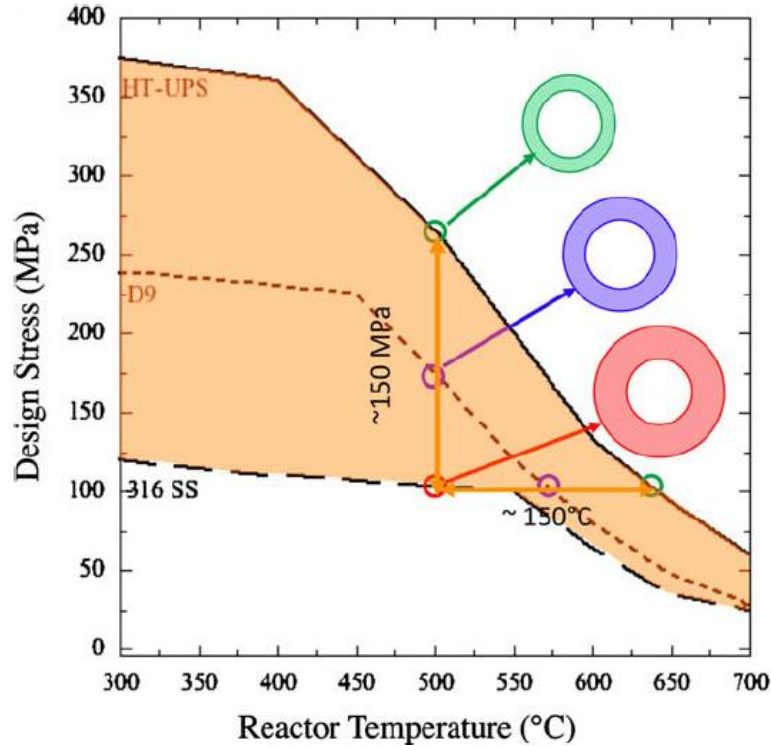
Figure 1.2. Comparison of design stresses and sectional views of pipes for the conventional austenitic stales steel 316 relative to advanced austenitic steels, alloy D9 and HT-UPS [7] indicating the impact of the advanced steels on material commodities and thermal efficiency. (Assuming design temperature of 500 °C).

One of the newly developed advanced austenite stainless steels is the Nb-containing and nitrogen-stabilized Fe-25%Ni-20%Cr (along with other minor elements) austenitic steel (here afterward referred to as Alloy 709) [10]. Preliminary investigations showed that the Alloy 709 is an excellent candidate material for the structural applications in the SFR due to its high temperature strength, corrosion resistance, sodium compatibility, and thermal stability and creep properties relative to code-approved conventional 300-series austenitic steels [11, 12]. Historically, Nb/Ti-stabilized 20%Cr-25%Ni austenitic stainless steels have been used as a fuel-cladding material for advanced gas-cooled reactors during the 1960s – 1990s in the UK where improved mechanical properties were achieved by forming the Nb(C, N) and TiN precipitates in these alloys [13-15]. This steel was further alloyed with other minor elements and designated as NF 709 by Nippon Steel Corporation during the mid-1980s to be used as

5

superheater tubes of the ultra-supercritical steam power plants [16, 17]. Recently, the 20%Cr-25%Ni austenitic stainless steel was furtherly developed by Oak Ridge National Laboratory [18] which has been down-selected as one of the SFR candidate materials for further assessment [10-12].

Serrated yielding resulting from the dynamic strain aging, DSA is considered as an important damage mechanism which can reduce or limit the life of many engineering components in current and future nuclear reactors [19]. Significant degradation of mechanical properties including fatigue life [20], fracture toughness [21], and ductility [22-26] may occur due to DSA associated with solute-dislocation interactions, especially for those materials operating within the temperature range of DSA regime [27]. Hence, an investigation into this phenomenon for such newly developed austenitic stainless steels should be carried out comprehensively for design and safety considerations.

Further, creep properties and characteristics govern the useful life of many engineering structures and play a major rule for design criteria in high-temperature applications. Hence, understanding the creep mechanisms along with their constitutive equations are essential for predicting the life of the materials in question and developing more creep-resistant microstructures as well.

In this dissertation, serrated yielding in the Alloy 709 has been examined by conducting a series of tensile tests at wide ranges of temperatures and strain rates followed by microstructural characterization. The nature of serrations, possible mechanisms causing the serrated yielding, the influence of serrated yielding on tensile properties, links between microstructure and the DSA in the Alloy 709 are thoroughly examined and discussed. Additionally, the creep properties and microstructural evolution of the Alloy 709 have been

investigated by conducting constant load creep tests at elevated temperatures followed by microstructure evaluations. Creep deformation mechanism, microstructural evolution and creep rupture properties for the Alloy 709 are investigated and compared with other advanced austenitic stainless steels.

1.1. References

[1] I.L. Pioro, Introduction: Generation IV International Forum, in: I.L. Pioro (Ed.), Handbook of Generation IV Nuclear Reactors, Woodhead Publishing 2016, pp. 37-54.

[2] K.L. Murty, I. Charit, Structural materials for Gen-IV nuclear reactors: Challenges and opportunities, J. Nucl. Mater. 383 (2008) 189-195.

[3] W. Hoffelner, Materials for Nuclear Plants From Safe Design to Residual Life Assessments, 1st ed., Springer, Switzerland, 2013.

[4] M.D. Mathew, Evolution of creep resistant 316 stainless steel for sodium cooled fast reactor applications, Transactions of the Indian Institute of Metals 63(2) (2010) 151-158.

[5] B. Raj, S.L. Mannan, P.R.V. Rao, M.D. Mathew, Development of fuels and structural materials for fast breeder reactors, Sadhana 27(5) (2002) 527-558.

[6] T.R. Allen, K. Sridharan, L. Tan, W.E. Windes, J.I. Cole, D.C. Crawford, G.S. Was, Materials Challenges for Generation IV Nuclear Energy Systems, Nucl. Technol. 162(3) (2008) 342-357.

[7] J.T. Busby, Economic benefits of advanced materials in nuclear power systems, J. Nucl. Mater. 392(2) (2009) 301-306.

[8] J.S. Cheon, C.B. Lee, B.O. Lee, J.P. Raison, T. Mizuno, F. Delage, J. Carmack, Sodium fast reactor evaluation: Core materials, J. Nucl. Mater. 392(2) (2009) 324-330.

[9] P.J. Maziasz, Development of Creep-Resistant and Oxidation-Resistant Austenitic Stainless Steels for High Temperature Applications, JOM 70(1) (2018) 66-75.

[10] T.-L. Sham, K. Natesan, Code Qualification Plan for an Advanced Austenitic Stainless Steel, Alloy 709, for Sodium Fast Reactor Structural Applications, International Conference on Fast Reactors and Related Fuel Cycles: Next Generation Nuclear Systems for Sustainable Development (FR17), IAEA, Yekaterinburg, Russian Federation, 2017.

[11] W. Corwin, Advanced Structural Materials (RC-3), Nuclear Energy University Programs (NEUP), Fiscal Year (FY) 2015 Annual Planning Webinar, DOE, 2014.

[12] T.-L. Sham, L. Tan, Y. Yamamoto, Development of Advanced 9Cr Ferritic-Martensitic Steels and Austenitic Stainless Steels for Sodium-Cooled Fast Reactors, Fast Reactors and Related Fuel Cycles: Safe Technologies and Sustainable Scenarios (FR13), IAEA, Vienna, 2015, pp. 1-9.

[13] J.D. Cook, D.R. Harries, A.C. Roberts, Some factors affecting the creep strength of 20%Cr-25%Ni-Nb austenitic steel at 750 °C, Creep Strength in Steels and High Temperature alloys, The Metals Society, London, 1972, p. 91.

[14] H.E. Evans, D.A. Hilton, Structure and properties of nitrided stainless steel fuel cladding for use in advanced gas-cooled reactors, Nucl. Energy 18 (1973) 33-38.

[15] G. Knowles, The creep strenghth of a 20%Cr-25%Ni-Nb steel containing controlled particle dipersion, Met. Sci. 11 (1977) 117-122.

[16] M. Kikuchi, M. Sakakibara, Y. Otoguro, H. Mimura, S. Araki, T. Fujita, An Austenitic Heat Resisting Steel Tube Developed for Advanced Fossil-Fired Steam Plants, High Temperature Alloys, Their Exploitable Potential, Elsevier, London, 1985, pp. 267-276.

[17] T. Takahashi, M. Sakakibara, M. Kikuchi, T. Ogawa, H. Sakurai, S. Araki, K. Nagao, H. Yasuda, Development of High-Strength 20Cr-25Ni (NF709) Steel for USC Boiler Tubes,, Nippon Steel Corporation, 1988.

[18] P.J. Maziasz, J.P. Shingledecker, N.D. Evans, Y. Yamamoto, K.L. More, R. Trejo, E. Lara-Curzio, Creep Strength and Microstructure of AL20-25+Nb Alloy Sheets and Foils for Advanced Microturbine Recuperators, Journal of Engineering for Gas Turbines and Power 129(3) (2006) 798-805.

[19] P. Rodriguez, Dynamic Strain Ageing: Is it really a damage mechanism?, in: B. Raj, K.B.S. Rao, T. Jayakumar, R.K. Dayal (Eds.) Proceeding of International Symposium on Materials Ageing and Life Management, Allied Publishers Limited, Kalpakkam, India, 2000, pp. K1-K14.

[20] V.S. Srinivasan, M. Valsan, R. Sandhya, K. Bhanu Sankara Rao, S.L. Mannan, D.H. Sastry, High temperature time-dependent low cycle fatigue behaviour of a type 316L(N) stainless steel, Int. J. Fatigue 21(1) (1999) 11-21.

[21] Y.H. Jung, K.L. Murty, Effect of Temperature and Strain Rate on Upper Shelf Fracture Behavior of A533B Class 1 Pressure Vessel Steel, in: T.A. Cruse (Ed.), Fracture Mechanics: Nineteenth Symposium, ASTM, STP 969, Philadelphia, 1988, pp. 392-401.

[22] M. Doner, H. Conrad, Deformation mechanisms in commercial Ti (0.5 at. pct oineq) at intermediate and high temperatures (0.3 - 0.6 tinm), Metall. Trans. 4 (1973) 2809-2817.

[23] S.I. Hong, W.S. Ryu, C.S. Rim, Elongation Minimum and Strain Ram Sensitivity Minimum of Zircaloy-4 J. Nucl. Mater. 116 (1983) 314-316.

[24] E. Bouchaud, L. Kubin, H. Octor, Ductility and dynamic strain aging in rapidly solidified aluminum alloys, Metallurgical Transactions: A 22 (1991) 1021-1028.

[25] C. Gupta, J.K. Chakravartty, S.L. Wadekar, J.S. Dubey, Effect of serrated flow on deformation behaviour of AISI 403stainless steel, Mater. Sci. Eng., A 292 (2000) 49-55.

[26] B.K. Choudhary, Influence of Strain Rate and Temperature on Tensile Deformation and Fracture Behavior of Type 316L(N) Austenitic Stainless Steel, Metall. Trans. A 45 (2014) 302-316.

[27] K.L. Murty, E.O. Hall, Dynamic Strain-Aging and Neutron Irradiation in Mild Steel in: Irradiation Effects on the Microstructure and Properties of Metals, ASTM STP 611,1976, pp. 53-71.

2. BACKGROUND AND LITERATURE REVIEW

2.1. Austenitic stainless steel

Austenitic stainless steels are extensively utilized in many engineering applications including conventional and nuclear power plants owing to their excellent mechanical properties at high temperatures coupled with corrosion/oxidation resistance [1]. Austenitic stainless steels are based on the Fe-Ni-Cr ternary system [2]. Their major constituent elements are Fe together with some amount of dissolved C, about 0.03 – 0.15%, occupying interstitial sites in the iron lattice [3]. They are stainless because they contain at least about 13 wt.% of Cr that forms the self-healing chromium oxide on their surfaces providing absence of staining, rusting and corroding in various aqueous or corrosive chemical environments; higher chromium (> 18 wt.%) is usually added for more hostile environments [4]. They are austenitic because of the closed pack crystal structure of a face-cantered-cubic (FCC) even at room temperature (not like ferritic steel which has a body-centered cubic, BCC) owing to higher Ni contents; other alloying elements such as N, C and Mn may replace Ni as an austenite stabilizers [5]. Conventional and advanced austenitic stainless steels are alloyed with varying additions and combinations of elements (either interstitial or substitutional), which directly influence the mechanical properties over a wide range of temperatures.

2.1.1. Alloying elements in austenitic stainless steels

A brief description of some of the major alloying elements and their impact on the mechanical properties at elevated temperatures are given below.

- *Chromium*

Chromium is mainly added to provide corrosion and oxidation resistance by creating a protective layer of chromium oxide (passivation) although it is also considered a ferritic

11

stabilizer and other elements have to be added to stabilize the austenite structure [4, 5]. Additionally, chromium is a carbide former which can enhance formation of carbide precipitates providing higher strength of austenitic stainless steels at elevated temperatures [6].

- *Nickel*

Nickel is an essential element in most of the austenitic stainless steels to stabilize the austenite structure at all temperatures and together with chromium, it imparts most of the physical and high-temperature strength properties to these austenitic steels [3, 5, 7].

- *Carbon*

Carbon also stabilizes the austenite phase and enhances the formation of chromium carbides [8]. It can provide higher creep strength via both solid solution and precipitation strengthening [5]. It has, however, a negative effect on the corrosion resistance and it is usually kept below about 0.03% to improve stress corrosion cracking resistance [9].

- *Nitrogen*

Nitrogen is a major interstitial alloying element in conventional and advanced austenitic stainless steels [9]. It is considered as a replacement for carbon since it is a stronger austenite stabilizer [9, 10]. Nitrogen enhances creep strength at higher temperatures due to (i) solid solution strengthening, (ii) precipitation strengthening, (iii) formation of interstitial solute complexes and (iv) decrease in stacking fault energy [11, 12]. However, a high amount of nitrogen will reduce the creep ductility [5].

- *Niobium and Titanium*

Niobium and Titanium are ferrite stabilizer elements, and strong carbide and nitride formers which can enhance the corrosion properties by reducing the matrix carbon contents and hence retarding some harmful carbides [2, 5]. Small additions of such elements greatly reduce the minimum creep rates due to the formation of Nb(C, N) and Ti(C, N) particles in

12

austenitic stainless steels [13-15]. However, the ratio to carbon and nitrogen is important to maximize the strengthening effect [5, 13-15]; a higher amount of niobium, greater than 0.3 wt.%, may reduce the creep strength [15].

- *Molybdenum*

Molybdenum is also a ferrite stabilizer and it must, therefore, be optimized with austenite stabilizers to maintain the austenitic phase [5]. It improves creep strength due to solid solution strengthening [5]. Molybdenum can also facilitate carbide precipitates and enhance resistance against corrosion [4].

- *Manganese*

Manganese is, on the other hand, an austenite stabilizer and is usually used as a substitute for nickel [5]. However, higher manganese contents may undesirably exhibit less corrosion resistance [2].

- *Silicon, Phosphor, Sulphur and Boron*

Silicon, phosphor, sulfur and boron are usually added to austenitic stainless steels with less than 0.5 wt. % to promote oxidation, increase machinability, improve the hot workability and increase the corrosion resistance [16]. It should be noted that a very small amount of such minor elements could affect the creep strength or ductility dramatically. For example, the creep rupture time increased by about three orders of magnitude with 40 ppm boron in austenitic stainless steels [17]. This may be attributed to the influence of these minor elements on enhancing or retarding the intermetallic phases formed in the austenite matrix such as sigma or Laves phases [18].

Note that other alloying elements (not discussed above, such as Al, V, Cu, W etc.) may be added in austenitic stainless steels to give desired properties depending on the applications.

13

2.1.2. Common precipitates in advanced austenitic stainless steels

High temperature strengthening in the majority of advanced austenitic stainless steels originates from the fine scale precipitates formed during service [2, 5, 13, 15, 19]. In this section, the common types of precipitates employed in the creep-resistant austenitic stainless including $M_{23}C_6$, M (C, N), M_6C and Z-phase are emphasized in terms of their primary properties and influence on high temperature creep strength. It should be noted that intermetallic phases (Sigma phase, Laves phase, G phase etc.) may also form in advanced austenitic stainless steels that can directly affect the high temperature mechanical properties.

- $M_{23}C_6$

$M_{23}C_6$ carbide is the most predominate precipitate which occurs nearly in all austenitic stainless steels. M refers to carbide former element, mainly Cr but other metallic elements like Fe, Mo, and Ni can also partially substitute for Cr [4, 5, 16, 20]. It has an FCC crystal structure with lattice parameter about three times larger than that of the austenite matrix [5, 16, 20]. The orientation of the $M_{23}C_6$ carbide with respect to the austenite matrix (γ) has been usually reported to have a cube-to-cube relationship as follows [5, 16, 20],

$$\{0\ 0\ 1\}_\gamma \parallel \{0\ 0\ 1\}_{M_{23}C_6}$$
$$\langle 1\ 0\ 0\rangle_\gamma \parallel \langle 1\ 0\ 0\rangle_{M_{23}C_6}$$

The occurrence of the $M_{23}C_6$ carbides within matrix and grain boundaries have been reported to enhance high temperature creep strength by restricting the movement of dislocations and making grain boundary sliding more difficult respectively [6, 20]. However, $M_{23}C_6$ carbides have relatively high coarsening rates resulting in the disappearance of precipitate strengthening which made it not so attractive to be a primary strengthening precipitate for high temperature applications [16, 19]. Further, $M_{23}C_6$ carbides have detrimental effects on corrosion resistance, ductility and toughness [2, 5]. Thus, nitrogen and niobium are

14

usually added to austenitic stainless steels to retard the formation of $M_{23}C_6$ carbides by either reducing the solubility of carbon [16] or forming more stable carbonitrides [5] whose effects are described in the following paragraphs.

- *M(C, N)*

When austenitic stainless steels are stabilized with strong carbide/nitride formers such as Nb, V or Ti, carbonitrides precipitates of type M(C, N) invariably occur where M stands for the stabilizing carbide/nitride formers [2, 5, 13, 15]. M(C, N) has also an FCC crystal structure with lattice parameter slightly larger than that of the austenite matrix [5, 16, 20]. The orientation of the M (C, N) carbonitrides with respect to the austenite matrix (γ) has also a cube-to-cube relationship as follows [5, 16, 20],

$$\{0\ 0\ 1\}_\gamma \parallel \{0\ 0\ 1\}_{M(C,N)}$$
$$\langle 1\ 0\ 0 \rangle_\gamma \parallel \langle 1\ 0\ 0 \rangle_{M(C,N)}$$

M(C, N) carbonitrides occur frequently within the matrix and can reduce the possibility of intergranular corrosion [2, 4, 7]. They are more stable than $M_{23}C_6$ carbides at high temperature and thus are considered the most effective precipitates for creep resistant austenitic stainless steels [5, 13, 19, 21].

- *Z-phase*

The Z-phase is known as a stable fine dispersed complex carbonitride which occurs in austenitic stainless steels containing both niobium and nitrogen with suggested chemical composition of CrNb(C, N), and Fe may replace Cr and Mo may substitute for Nb in the lattice [4, 5, 19]. The Z-phase has a tetragonal crystal structure and its orientation with respect to the austenite matrix (γ) has the following relationship [4, 5, 22],

$$(0\ 0\ 1)_\gamma \parallel (0\ 0\ 1)_{Z-phase}$$
$$[1\ 0\ 0]_\gamma \parallel [1\ \overline{1}\ 0]_{Z-phase}$$

The high stability of the Z-phase at high temperatures (more stable than M(C, N) phase) makes it an attractive phase in the advanced austenitic stainless steels for enhancing high temperature mechanical properties [15, 19, 21-23].

2.2. Serrated yielding

Serrated yielding phenomenon can be defined as an instability in the stress-strain curves during tensile tests within a certain regime of temperatures and strain rates. The phenomenon was first investigated systematically by Portevin and Le Chatelier almost a century ago [24], nevertheless, it is still being continually received regular attention in the literature in terms of both experimental and theoretical aspects. Serrated yielding is also interchangeably called Portevin and Le Chatelier effect (PLE), discontinuous yielding, and jerky flow or repeated yielding in the literature. The instability in the stress-strain curves results from the sudden increase in the stress or the plastic strain leading to the inhomogeneous plastic deformation. There are several physical processes that can cause a sudden increase in the plastic strain during tensile deformation, summarized by Rodriquez [25] as follows:

1- During dislocation glide, the plastic strain rate, $\dot{\varepsilon}$ can be described by Orowan's equation, as follows,

$$\dot{\varepsilon} = \rho_m b \, \bar{v} \tag{2.1}$$

where ρ_m the density of mobile dislocations, b Burger's vector and $\bar{v}$ average velocity of mobile dislocations. Therefore, the instantaneous increase in the plastic strain rate for a given material will occur by a sudden change in ρ_m or in $\bar{v}$ or in both. The dynamic interaction of the moving dislocation with solute atoms, which is termed the Dynamic Strain Aging (DSA), can lead to a sudden increase in ρ_m and/or in $\bar{v}$. The DSA will result in intermittent pinning and release (repeatedly locking and unlocking), between dislocations and solute atoms during

16

plastic deformation and hence serrated flow.

2- In ordered alloys, the interaction of the moving dislocations with order-disorder transformations, modulations or gradients in order can result in serrated flow [26-28].

3- In low stacking fault alloys, deformation due to continual mechanical twining can also cause serrations resulting in negative strain sensitivity [29, 30].

4- Stress or strain induced phase transformations can result in serrated yielding as well [31].

5- At very low temperatures, the sudden increase in the plastic strain during deformation can be attributed to the sudden increase in the temperature due to the adiabatic heating leading to serrated yielding [32, 33].

In both interstitial and substitutional solid solution alloys, the most widely accepted process for the serrated yielding is the dynamic strain aging (DSA) originating at the dislocation scale from the interaction between the moving dislocation and solute atoms [34]. This particular phenomenon will be mainly examined in this research work. The phenomenon of DSA is to be distinguished from the static strain aging (SSA) which refers to the sharp yield point for samples partially prestrained and aged for a prescribed time and then reloaded [35]. Unlike the DSA, the solute atoms diffuse to the dislocation core in SSA during the aging process and not during deformation. The occurrence of dynamic strain aging depends upon the rate of solute diffusion and the dislocation velocity, which are functions of temperature and strain rate. Although DSA and the serrated yielding have been interchangeably used in the literature, the serrated yielding is a manifestation of the occurrence of the DSA.

2.2.1. Types of serrations

During serrated yielding, a series of shear bands appears sequentially with sometimes regular spacing or as a set of bands generated at one end of the specimen propagating to the

other end [25, 36, 37]. The repeated and systematic fluctuations in the stress strain curves during tensile deformation have been classified according to their apparent oscillations and associated deformation characteristics. Based on the accepted nomenclature in the literature, five types of serrations have been identified; Types A, B, C, D and E [25, 36, 37] and Figure 2.1 shows a schematic of the segments of stress-strain curves illustrating the various types of serrations. The characteristics of the different types of serrations, associated deformation characteristics and the experimental conditions that produce them are as follows.

- *Type A*

    Type A serrations are large regularly spaced serrations characterized by a sharp rise in the stress followed by a discontinuous drop below the general level of the stress-strain curves (see Figure 2.1). They result from the repeated locking and unlocking of moving dislocations leading to repeated deformation bands initiating at one end of the specimen and propagating in the straining direction along the gauge length [25, 36, 37]. Type A serrations usually occur at low temperatures and high strain rates within the DSA regime.

- *Type B*

    Type B serrations are closely spaced serrations represented as fine oscillations about the general level of stress-strain curves (see Figure 2.1). They occur due to the rapid locking and unlocking of moving dislocations by solute atmospheres. Unlike type A, the deformation bands due to the type B serrations are discontinuously propagated due to the pinning of moving dislocation within the bands [25, 36]. Type B serrations usually occur at a higher temperature and lower strain rate level than that for type A serrations. They can be also developed from those of type A at higher strains [25]. In practice, mixed serrations of both types A and B are observed.

- *Type C*

Type C serrations are unlocking serrations characterized by stress drops always below the general level of the stress strain curves (see Figure 2.1). They commonly occur at higher temperatures and lower strain rates than that of types A and B serrations.

- *Type D*

Type D serrations, also called staircase type, arise from band propagation with no work hardening or strain gradient ahead of the moving band. They can also be mixed with types B and C serrations (see Figure 2.1).

- *Type E*

At high values of strain, type E serrations usually appear after type A serrations with no work hardening during band propagation characterized by irregularities of the stress-strain curves.
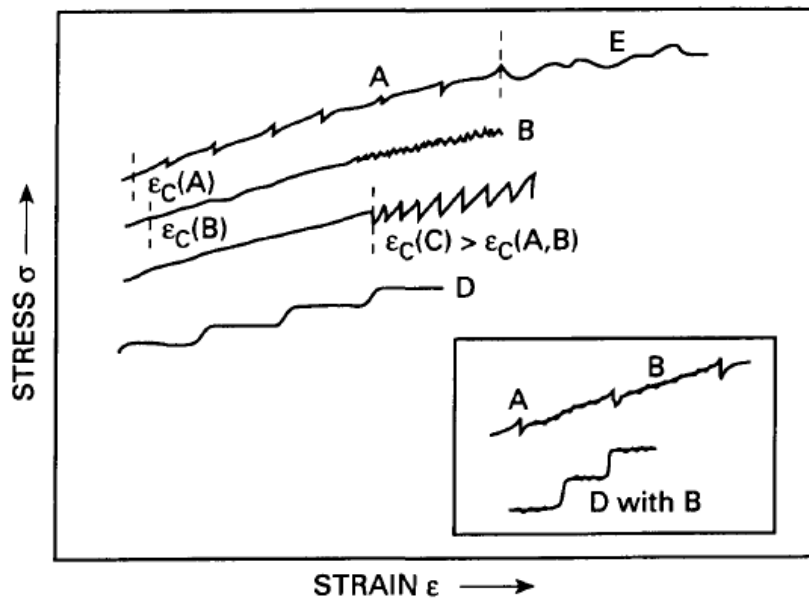
Figure 2.1. Schematic for the segments of stress-strain curves illustrating the various types of serrations [25].

Unlike types D and E, types A, B and C are frequently observed and their characteristics are well-known and demonstrated. Often, different types of serrations can overlap and occur

simultaneously depending on the test conditions. Furthermore, the serrations commonly commence only after a critical amount of plastic strain denoted as ε_c before which smooth flow curve is obtained. As will be described later, the ε_c is an important parameter for determining the activation energy for the serrated yielding.

2.2.2. Models for the serrated yielding from dynamic strain aging (DSA).

During the last decades, numerous models have been developed to understand the underlying micro-mechanism relating the dynamic strain aging resulting in the serrated yielding. However, detailed mechanisms associated with the DSA are not yet fully understood. Originally, the *solute dragging model* was early developed by Cottrell and Bilby [38] and Cottrell [39, 40] where solute atoms diffuse and form an atmosphere along dislocations that are moving in a quasi-viscous manner. When the average drift velocity of solute atoms is equivalent to the average velocity of the dislocations, the unstable plastic flow will initiate leading to the serrated behavior. Thus, the critical velocity, v_c needed for the onset of the serrated yielding is given by [40]:

$$v_c \cong \frac{4D_s}{l} \tag{2.2}$$

where D_s the diffusion coefficient of the solute atoms, l the radius of the solute atmosphere. For substitutional alloys, D_s is initially far too small for solute atmospheres to form along moving dislocations and thus Cottrell suggested that the concentration of vacancies, C_v is increased by plastic deformation allowing dynamic strain aging to occur after a critical amount of strain, ε_c [39]. By substituting v_c of equation (2.2) with the average velocity of mobile dislocations, $\bar{v}$ in Orowan's equation (2.1), the critical strain rate, $\dot{\varepsilon}_c$ for the onset of the

serrated flow can be written in terms of the vacancy concentration, C_v as

$$\dot{\varepsilon}_c = \frac{4\rho_m b C_v D_\circ \exp\left(\frac{-Q_s}{kT}\right)}{l} \tag{2.3}$$

where $D_\circ$ the diffusion frequency factor, Q_s the effective activation energy for the solute migration, k Boltzmann constant and T the temperature. Further, the increase in the vacancy concentration, C_v and the mobile dislocation density, ρ_m with plastic strain, ε can be expressed by the following equations [41, 42]:

$$C_v = K\varepsilon^m \tag{2.4}$$

$$\rho_m = N\varepsilon^\beta \tag{2.5}$$

where K, N, m and β are constants. By substituting equations (2.4) and (2.5) into (2.3) gives the critical strain, ε_c for the onset of the serrated yielding as

$$\varepsilon_c^{m+\beta} = \frac{l\dot{\varepsilon}\exp\left(\frac{Q_s}{kT}\right)}{4NbKD_\circ} \tag{2.6}$$

Although the above solute dragging model can predict qualitatively the strain rate and temperature regime for the serrated yielding, it has been shown that the values predicted for the ε_c calculated from equation (2.6) are in error by several orders of magnitude compared to experimental values [43, 44]. Moreover, the solute drag model does not take into account the effect of solute concentration on the serrated yielding [43].

Therefore, McCormick [43], Van den Beukel [44, 45] and Kubin and Estrin [46] later developed the "*arrest model*" taking into account the fact that the dislocation during plastic deformation glides in its slip plane in a discontinuous process rather than in a quasi-viscous manner. In other words, the mobile dislocations are being temporarily arrested at obstacles

21

during deformation, breaking free probably by thermal activation and advancing further to other obstacles. During the arrest or waiting time at obstacles, solute atoms can sufficiently diffuse to temporarily arrested dislocations and lock them resulting in the DSA occurrence [43-46]. Thus, serrated yielding in the stress-strain curves will initiate when the waiting time of the dislocations at obstacles, t_w equals to the aging time required for the solute atoms required to lock the arrested dislocation, t_a. Following McCormick [43], the waiting time, t_w and the aging time, t_a may be expressed as

$$t_w = \frac{L \, \rho_m \, b}{\dot{\varepsilon}} \tag{2.7}$$

$$t_a \cong \left(\frac{C_1}{\alpha C_\circ} \right)^{3/2} \frac{k \, T \, b^2}{3 \, U_m \, D_s} \tag{2.8}$$

where L is the average distance between arresting obstacles, C_1 is the solute concentration at the dislocations required to lock them, C_o is the original solute concentration in the alloy, α constant and U_m solute-dislocation binding energy. By equating the equations (2.7) and (2.8), the strain rate for the onset of serrated yielding can be given as

$$\dot{\varepsilon} = \left(\frac{\alpha C_\circ}{C_1} \right)^{3/2} \frac{3 L \, \rho_m \, U_m \, C_v \, D_\circ \exp\left(\frac{-Q_s}{kT} \right)}{k \, T \, b} \tag{2.9}$$

 Using equations (2.4) and (2.5), equation (2.9) can be rewritten in terms of the critical strain, ε_c as

$$\varepsilon_c^{\,m+\beta} = \left(\frac{C_1}{\alpha C_\circ} \right)^{3/2} \frac{\dot{\varepsilon} \, k \, T \, b \exp\left(\frac{Q_s}{kT} \right)}{3 L N K U_m D_\circ} \tag{2.9}$$

This model has been widely accepted and employed to estimate the solute atoms responsible

for DSA by determining the activation energy for the serrated flow and comparing it with an activation energy for the solute diffusivity. However, the model is not applicable for some alloys that exhibit an inverse critical strain behavior in which the critical strain decreases with increasing strain rate [47].

Ananthakrishna has developed a model for the DSA based on the collective behavior of dislocations using three types of dislocation densities, namely, the mobile, immobile and the dislocations with solute atoms [48]. By deriving the evolution equations for the three dislocation densities, the model is able to explain majority of general features of the DSA such as the existence of serrations in a window of strain rates and temperatures, and negative strain rate sensitivity. Recently, DSA models based on the strength variation of dislocation junctions [49] and the migration energy for solute atom jumps across dislocation cores [50] are also reported and developed.

2.2.3. Methods for evaluating the activation energy for the serrated yielding

The values for the activation energy along with the exponent $m+\beta$ for the serrated flow can serve to identify the solute atoms and mechanisms associated with the DSA [51]. In all aforementioned models, the variations of the ε_c with the temperature, T and strain rate, $\dot{\varepsilon}$ can be expressed as

$$\varepsilon_c^{m+\beta} = K' \dot{\varepsilon} \exp(Q/kT) \tag{2.10}$$

where K' is a constant and Q is the activation energy associated with the serrated flow. Different methods have been employed to estimate the activation energy for the serrated flow. Four methods are utilized in this research as follows,

- *Method-I:*

  From the Arrhenius plot of $\dot{\varepsilon}$ versus $1/T$ in semi-log scale, Q-value can be obtained as

Q = -2.3 × k × *slope* where the slope of the boundaries delineating serrated and smooth flow is used. This method does not require the critical strain determination and it can be used to determine the Q-values for the onset as well as termination of serrations.

- *Method-II:*

The critical strain method, where Eq. (1) is employed to determine the Q-value as Q = *2.3 × k × (m+β) × slope* where the slope is obtained from ε_c versus $1/T$ in semi-log plot. This method requires the average value of *(m+β)* over a range of strain rates and temperatures to be first evaluated as the slope of $\dot{\varepsilon}$ versus ε_c in log-log scale.

- *Method-III:*

Critical strain intercept method, where $\dot{\varepsilon}$ versus ε_c is firstly plotted. Subsequently, the values of the $\dot{\varepsilon}$ corresponding to different critical strain levels at different temperatures versus $1/T$ in semi-log scale can be used to evaluate the activation energy as Q = *-slope ×k × 2.3*. This method doesn't involve the use of *(m+β)* value.

- *Method-IV:*

Following the arrest model for the DSA developed by McCormick [43] equation (2.9) relating the concentration of solute atoms, Q-value can be determined from the slope of the semi-log plot of the $\varepsilon_c^{(m+\beta)/T}$ versus $1/T$ as Q = *2.3 × k x slope*. In this method, individual values of *(m+β)* at different temperatures are used.

Other methods for the evaluation of the activation energy for the serrated flow such as stress drop method [36], the temperature dependence of elongation minima as a function of strain rate [52] and the minima in the fracture toughness parameter as a function of temperature and strain rate [53] are not employed in this work.

2.2.4. Influence of dynamic strain aging on mechanical properties

The serrated yielding observed in solid solution alloys can be considered as a

24

macroscopic observation for the occurrence of the DSA. Moreover, a distinct change in the mechanical properties has also been numerously observed within DSA temperature regime. In this section, the influence of DSA on the tensile properties, fracture toughness, creep, fatigue and creep-fatigue interactions is discussed.

- *Tensile properties*

In the absence of DSA, a decrease in flow stress and working-hardening rate and an increase in strain rate sensitivity and ductility are expected as temperature increased. However, peaks and/or plateaus in the yield stress, tensile strength and working-hardening rate, negative strain rate sensitivity and minimum in ductility represent manifestations of the occurrence of DSA within a specific temperature regime [25, 34, 37, 46, 54]. Figure 2.2 [25] shows a schematic illustration of the various manifestations for DSA. Although DSA provides a strengthening effect on the material, the detrimental effect in ductility resulting from negative strain rate sensitivity is of concern. The loss in ductility within dynamic strain aging regime has been enormously reported in many various alloys including Al-based alloys [55], Zr-based alloys [53], Ti-based alloys [56], ferritic steels [57], austenitic stainless steels [54, 58, 59] and nickel-based superalloys [60].

- *Fracture toughness*

The fracture toughness is susceptible to DSA [61-66]. Reduced fracture initiation energy and unloading compliance as a measure for the fracture toughness are the main features observed within DSA regimes using three-point bend tests [62, 65]. However, some materials can exhibit an increase in fracture toughness or no influence in the temperature regime where DSA operates [63, 64].

- *Creep*

DSA can also influence various aspects on creep properties including creep curve,

activation energy and stress exponent [67]. The main indications for the occurrence of DSA during creep include an increase and/or negative activation energy with temperature [68, 69], decrease in creep ductility [68] and discontinuous (called also step-like, strain burst, staircase or strain jumps) in the creep curve [70, 71]. Further, an anomalous decrease in stress exponent resulting in a transition in the creep mechanism can occur in solid solution alloys due to the interaction between solute atoms and moving dislocations [72, 73].
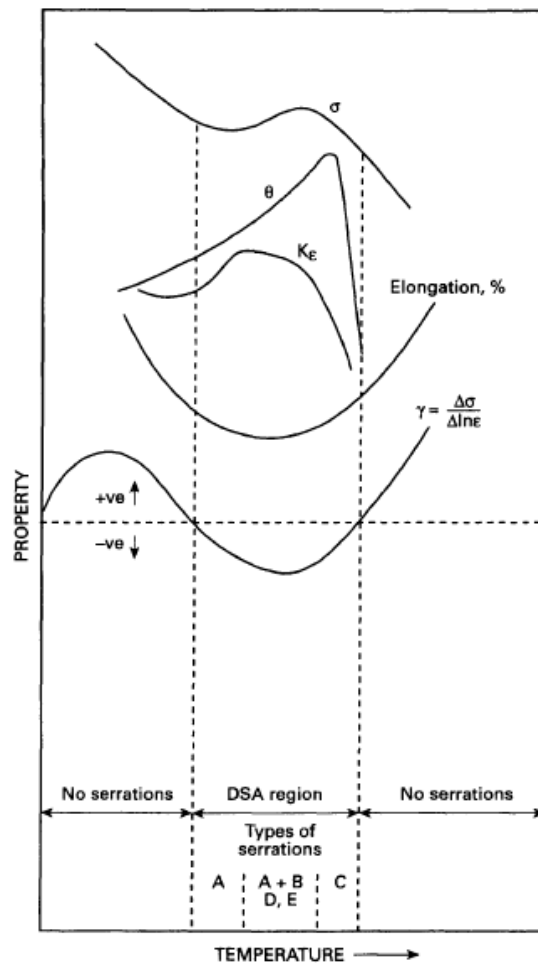
Figure 2.2. Schematic illustration of the various manifestations of the DSA [25].

- *Fatigue*

DSA has also been shown to affect various aspects of low cycle fatigue properties. Decrease in fatigue-life with increasing temperature, serrations on the stress-strain hysteresis

loops, increase in cyclic hardening, negative strain rate sensitivity and inverse dependence of stress amplitude on temperature have been reported to occur within the DSA regime in 316L(N) stainless steel and Ni-base superalloy [74-76].

- *Creep-fatigue interaction*

The change in the waveform or the introduction of a hold time during fatigue test (i.e. creep-fatigue test) has been shown to be influenced by the occurrence of DSA. Although improved creep-fatigue life has been reported in some alloys due to DSA resulting in retardation of the fatigue damage during hold time [77-79], the influence of serrated yielding on creep-fatigue properties is not well-known and requires more systematic studies and evaluation [80, 81].

2.2.5. Factors influencing DSA

As disused earlier, the serrated yielding resulting from DSA is directly influenced by the test temperature, strain rate, strain and solute concentration. Apart from these primary variables, DSA can also be influenced by other factors such as radiation, grain size, prior work and aging.

- *Radiation*

Radiation seems to have a beneficial effect on the materials operating within DSA regime [62, 82-84]. Irradiation at low fluence can suppress the DSA due to radiation induced vacancies in some temperature range resulting in improved mechanical properties [62].

- *Grain size*

It has been postulated that the DSA process occurs preferentially at grain boundary regions resulting in humps in the Hall-Petch slope at an intermediate temperature where DSA operates [85].

- *Prior working*

Prior working was found to enhance the strength of the material in the DSA regime with an acceptable loss of ductility and fracture toughness [80].

- *Heat treatment*

Samuel *et al.,* have studied the effect of aging time and temperature on the type C serrations and concluded that certain time-temperature combination of aging eliminates serrated yielding due to the coarsening of the precipitates and reducing the precipitate density at grain boundaries [86]. Just recently, Beese *et al.,* have reported the absence of dynamic strain aging in an additively manufactured nickel-base superalloy due to the closely spaced secondary phases making type C serrations either experimentally undetectable or completely absent [87].

- *Machine effect*

It should be noted that the observation of the serrations in the stress strain curves can also be affected by the tensile machine itself resulting from the machine stiffness [88]. The total strain recorded by the tensile machine is a combination of machine elastic strain and the sample elastic and plastic strains. Tensile machines are commonly divided into two types; soft and hard. For a hard machine, the elastic modulus for the machine and related loading trail is much higher than that for the sample so that when the sample yields suddenly, the load will be directly affected and recorded. Hard tensile machines are preferred for DSA studies since small sudden drops in the sample due to DSA are easily determined.

2.2.6. Serrated yielding in austenitic stainless steels

Serrated yielding in austenitic stainless steels was first reported by Tamhankar *et al.,* [89] and subsequently, numerous studies on different grades of austenitic steels have been carried out. In general, the serrated yielding in austenitic stainless steels are typically observed within a strain rate range varying from 3×10^{-6} s^{-1} – 3×10^{-1} s^{-1} and at temperatures varying

28

from 473 K – 1073 K. Serrations of types A, B, and C have been commonly reported to occur while types D and E are rarely observed in austenitic stainless steels. Other manifestations for the occurrence of the DSA including negative strain sensitivity, increase in the material strength, loss in ductility and increase in the work-hardening rate are frequently reported. The activation energies and the ($m+\beta$) exponents have been found to vary from 75 – 385 kJ/mole and 0.7 – 2.3 respectively depending on the temperature and strain rate levels. Different mechanisms have been suggested to cause the DSA in austenitic stainless steels. Data from published literature for the values of activation energy, ($m+\beta$) exponent, and proposed mechanisms for serrated flow in various grades of austenitic stainless steels are compiled in Table 2.1[51, 54, 90-100].

Samuel *et al.,* [94] have investigated the serrated yielding behavior in type-316 stainless steel (SS) where two temperature regions are noted: low-temperature region (LT) ~523 – 623 K and high-temperature region (HT) ~673 – 923 K with activation energies of 138 and 277 kJ/mole respectively. They attributed the occurrence for the serrated yielding to the diffusion of interstitial solutes to dislocations in the LT region and substitutional solutes like Cr in the HT region. Similarly, Choudhary [54, 100] studied type-316L(N) with a higher amount of nitrogen (~0.14%) and concluded the same mechanisms associated with the LT and HT regions where different methods were employed to determine the activation energy for the serrated flow. In cold worked (CW) 316SS, Hong and Lee [95, 97], on the other hand, suggested the pipe diffusion of the interstitial atoms such as C or N along the dislocation cores to be responsible for the serrated yielding in the LT regime and the pipe diffusion of substitutional Cr along the dislocation core for HT regime. In all aforementioned studies in 316 SS, an increase in material strength and a decrease in ductility were noted consistent with

the regime of the serrated yielding regime [54, 94, 95, 97, 100].

In 15Cr-15Ni Ti-modified stainless steel (Alloy D9), Venkadesan *et al.,* [51] have identified three regimes of serrated flow: low temperature type A (LT-A), high temperature type A (HT-A) and high temperature type C (HT-C) and attributed the vacancy migration, vacancy pairs causing Schoeck-Seeger locking and interaction of Ti with C (or N) responsible for serrated flow respectively.

In Fe-35Ni-15Cr austenitic steel, Jenkins and Smith [91] suggested the C-vacancy pairs as the controlling mechanism for the serrated flow between 473 – 773 K and Cr-diffusion above 773 K. Similar conclusion for the high temperature regime was mentioned in high Ni austenitic steel, Fe-(31–41%) Ni-(0.12–0.18%) C by Rose and Glover [90]. However, they determined the relatively low value of activation energy in the low-temperature regime of about 85 kJ/mole correlating with the vacancy migration in γ-iron (taken as 1/3 of self-diffusion in γ-iron). A higher value of the activation energy (132-136 kJ/mole) was reported by Almeida *et al.,* [92] in type 304SS where C-vacancy or N-vacancy pairs were attributed to the dislocation locking by interstitial diffusion of C or N controlling the migration of the pair. The interaction of C-C pairs with Cr was suggested to provide sufficient locking to cause the serrations in the high-temperature regime in type 304 SS [92]. In 18-8 type SS, the interaction between (C, Ni) solute atom atmospheres and dislocations was ascribed to explain the DSA at lower temperature range and the interaction between (C, Cr) solute atom atmospheres and dislocations at higher temperature range [96].

In highly alloyed advanced austenitic stainless steel (AL6XN) Meng *et al.,* [98] have reported a relatively higher value of activation energy for the serrated flow of 304 kJ/mole where the diffusion of substitutional solutes, such as chromium and molybdenum was

suggested as the mechanism for the DSA. Another highly alloyed advanced austenitic stainless steel (SUS347J1T) has been studied by Nikulin and Kaibyshev [99] where the apparent activation energy for the onset and termination of jerky flow were found to be ~220 kJ/mole and ~355 kJ/mole respectively with $m+\beta$ varying from 1.2 to 1.95.

Table 2.1. Activation energy, ($m+\beta$) exponent, and proposed mechanisms for serrated flow in various austenitic stainless steels [51, 54, 90-100].

Material type	Range of temperatures (K)	Strain rate (s⁻¹)	$m+\beta$ exponent	Activation energy, Q (kJ/mole)	Suggested mechanism for serrated flow	Ref.
AISI 316	523 – 623 (LT) 673 – 923 (HT)	$3\times10^{-4} - 3\times10^{-2}$	2.3 (HT)	138 (LT*) 277 (HT)	N or C for LT and Cr for HT.	[94]
Alloy D-9 15Cr-15Ni	573 – 623 (LT-A) 723 – 873 (HT-A) 773 – 923 (HT-C)	$1\times10^{-5} - 1\times10^{-2}$	1.8 (LT-A) 1.28 (HT-A) 0.73 (HT-C)	115 (LT-A) 140 (HT-A) 178 (HT-C)	Vacancy for LT-A Interstitial for HT-A Ti and C for HT-C	[51]
18-8 type	523 – 673 (LT) 723 – 873 (HT)	$5\times10^{-5} - 5\times10^{-2}$	1.15 (LT) 2.29 (HT)	139 (LT) 173 (HT)	(C, Ni) for LT (C, Cr) for HT	[96]
SS304	446 – 633 (LT) 633 – 1053 (HT)	$3\times10^{-6} - 3\times10^{-1}$	-	114 (LT) 164 (HT)	LT due to vacancy diffusion and HT due to intestinal.	[93]
SS304	473 – 673 (LT) 673 – 1023 (HT)	$3.5\times10^{-6} - 3.5\times10^{-2}$	-	132 (LT) 191 (HT)	Interstitial -vacancy pairs diffusion.	[92]
Fe-35Ni-15Cr	373 – 573 (LT) 723 – 948 (HT)	$3\times10^{-5} - 3\times10^{-3}$	-	259 (LT) 398 (HT)	C-vacancy pairs for LT and Cr for HT.	[91]
SUS347J1T	803 – 953	$6.7\times10^{-6} - 1.3\times10^{-2}$	1.2 – 1.95	220 (LT) 355 (HT)	-	[99]
Fe-32Ni-C	373 – 523	$1\times10^{-5} - 1\times10^{-3}$	-	83	Vacancy diffusion.	[90]
SS316LN	523 – 603 (LT) 623 – 1023 (HT)	$3\times10^{-5} - 3\times10^{-2}$	1.48 (HT)	115 (LT) 204 (HT)	N and C diffusion for LT and Cr diffusion for HT.	[54, 100]
AL6XN	773 – 973	$3.3\times10^{-5} - 3.3\times10^{-3}$	-	304	Cr and Mo diffusion.	[98]
316L (CW)	523 – 923	$1\times10^{-4} - 1\times10^{-2}$	-	75 (LT) 205 (HT)	Pipe diffusion C for LT and Cr for HT.	[95, 97]

LT: low- temperature, HT: high- temperature, LT-A: low- temperature A-type, HT-C, high- temperature C-type.

2.3. Creep

Creep is the time-dependent plastic strain or deformation at constant temperature and constant stress or load. Creep characteristics play a major rule in design criteria for high temperature applications. Materials exposed at a homologous temperature of ~0.4 or above (the homologous temperature is the ratio of the absolute temperature under consideration, T and the melting temperature T_m in Kelvin) get deformed plastically over a period of time even when the applied stress is much less than the yield stress. Although creep has been known a long time ago, an extensive amount of studies started only in the late forties due to the increased demand for high temperature resistant materials for advanced power plants [101]. The demand, in fact, is still undergoing to meet the new generations of nuclear power plants which are being designed to operate at higher temperatures, higher doses of radiation and for longer service periods compared to the current fleet of nuclear reactors [1]. The lifetime of typical nuclear reactors can range to 60 years, therefore; direct testing for such long time creep behavior at laboratories is not practical [102]. Instead, creep tests involved at laboratories are performed at stresses higher than those encountered in service and then reliable extrapolation methods of the accelerated creep tests to lower stresses are utilized. This requires a comprehensive understanding of the rate controlling creep deformation since a blind-extrapolation of short-term creep data conducted at high stresses can lead to *nonconservative* estimates of the creep life at operating conditions [103].

2.3.1. Creep curves and characteristics

To understand the creep behavior of materials in question, uniaxial tensile tests under constant temperatures and loads are usually performed in laboratories to observe the plastic strain accumulated over time. The plot of the accumulated plastic strain during creep test (creep

33

strain, ε) as a function of time and the plot of the time derivative of the strain (creep rate, $\dot{\varepsilon}$) versus times are known as creep curves. A schematic of the typical creep curves for different stresses, σ and temperatures, T are shown in Figure 2.3. At the instant of applying the load ($t \sim 0$), an instantaneous strain, $\varepsilon_\circ$ is observed which is composed of elastic (instantaneously recoverable when the load is released), anelastic (recoverable with time when the load is released) and plastic (non-recoverable) components [104]. Following that, three different regimes in the creep curves are typically observed, namely, primary or transient creep regime (region I), secondary or steady-state creep regime (region II) and tertiary creep regime (region III). The nature of these creep regimes, as a function of time is a result of the changes occurring in the microstructural level of the materials where a competition between the strain-hardening and recovery processes develops. The effects of stress, σ and temperature, T on the creep curve, are also shown in Figure 2.3 where the creep strain and the creep rate both increase as the stress or temperature increased.
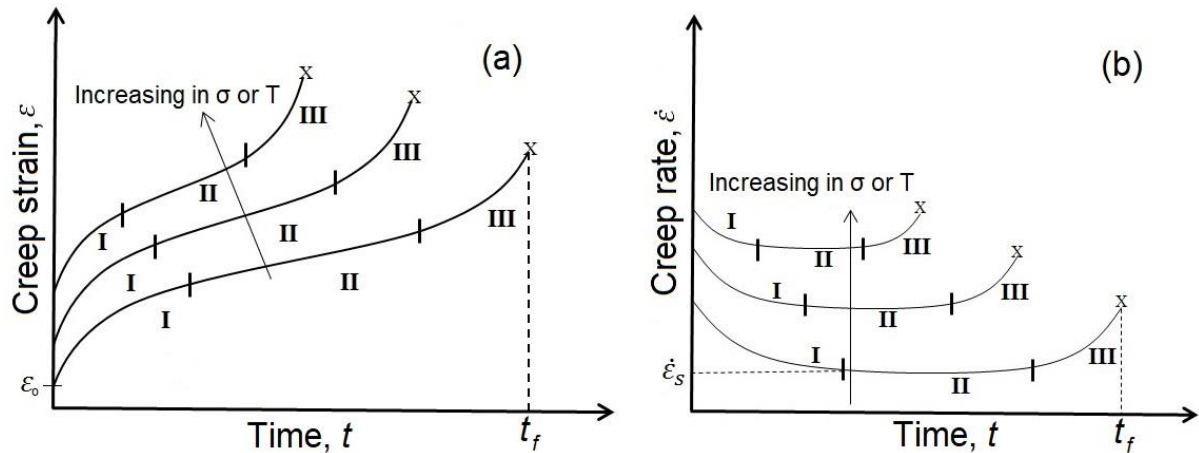
Figure 2.3. A schematic of the typical creep curves for different stresses, σ and temperatures, T showing the primary or transient creep (region I), steady-state creep (region II) and tertiary creep (region III).

In a primary creep regime, the rate of creep strain decreases over time until it reaches a minimum value corresponding to the onset of the secondary creep regime. The decreasing

creep rate during primary creep stage has been attributed to the higher strain-hardening rate relative to that of recovery. For most materials, the creep strain within primary creep regime follows a 1/3 power law with time [104].

Since creep occurs at a high homologous temperature, it mainly involves diffusion and the recovery rate gets higher to be balanced by the rate of hardening as the steady state region is reached. The steady-state creep regime is characterized by a constant creep rate corresponding to a steady state or minimum creep rate, $\dot{\varepsilon}_m$ which is of importance in the scientific community to understand the rate controlling creep mechanisms and serves as a design parameter. The steady-state or minimum creep rate, $\dot{\varepsilon}_m$ in high temperature creep is a unique function of the applied stress, σ and temperature, T through a power-law relation [105],

$$\dot{\varepsilon}_m = A'\sigma^n \exp(-\frac{Q_c}{RT}) \tag{2.11}$$

where A' constant, n the stress exponent, Q_c the activation energy for creep, R the universal gas constant and T the test temperature. Several mechanisms can contribute to the overall plastic strain during creep deformation; however, one mechanism usually dominates in controlling the steady-state creep rate. Hence, the steady state or minimum creep rate, $\dot{\varepsilon}_m$ is frequently employed to deduce the rate controlling creep mechanism. The use of the minimum creep rate properties to deduce the associated creep mechanism will be given in detail in the next section.

In the tertiary creep regime, the creep rate continually increases until sample ruptures at rupture time, t_f. Usually, the tertiary creep regime is considered as a fracture mode associated with metallurgical changes and the growth of creep damage such as necking

formation, internal void formation and/or precipitate coarsening. In addition to the parameter $\dot{\varepsilon}_m$ obtained during secondary creep regime, the time to rupture, t_f is also employed as a design parameter and extensively utilized for the material's life-prediction for high-temperature applications. In fact, a relation between the $\dot{\varepsilon}_m$ and t_f exists through the Monkman-Grant Relation (MGR) expressed as [106],

$$\dot{\varepsilon}_m^{\alpha} \, t_f = C_{MG} \tag{2.12}$$

where α and C_{MG} are constants. The constant α is usually found to be close to 1 for most materials. Furthermore, it was demonstrated by Dobeš and Milička that MGR can be modified by the creep strain, ε_f (total creep strain to failure) resulting in a better relationship between the $\dot{\varepsilon}_m$ and t_f [107],

$$\dot{\varepsilon}_m^{\alpha'} \frac{t_f}{\varepsilon_f} = C_{MMG} \tag{2.13}$$

where α' and C_{MMG} are modified-MGR constants. Equation (2.13) is utilized to estimate the creep damage tolerance parameter, λ as the inverse of the constant C_{MMG}. The value of λ ranges from 1 to 20 for engineering alloys depicting the range from brittle fracture mode for materials having low creep strain without significant plastic deformation to ductile materials that can withstand strain concentration without local cracking [108]. In austenitic stainless steels, values of 2.5 and 4 were reported, and fracture modes were attributed to the occurrence of intergranular cavitation and necking respectively [109]. Furthermore, the Larson-Miller parameter (LMP) is another empirical formula which has been broadly utilized to extrapolate rupture life data using a correlative approach expressed as [110],

$$LMP = T \cdot [C + \log(t_f)] \tag{2.14}$$

where T is in K, t_f in hr and C a constant often approximated as 20 for most materials.

According to the LMP, the log rupture time versus the LMP plot produces a temperature-independent master curve employed for predicting the lifetime of a material as a function of temperature and stress.

It should be mentioned that the nature of the creep curves is related to the microstructural changes during deformation; therefore, some materials exhibit anomalous creep curves associated with microstructural instabilities [111]. These materials do not follow the three stage creep curve discussed above and extensive substructure studies should be carried out to evaluate the origin of such behaviors.

2.3.2. Creep mechanisms in metals and alloys

Considerable efforts have been spent to understand the rate controlling creep deformation in metals and alloys which is influenced by many factors including applied stress, temperature, chemical compositions and metallurgical structures (including grain size, crystal structure, stacking fault, precipitates., etc.). In general, creep mechanisms in metals and alloys fall into two broad categories, namely dislocation creep (power-law creep) and diffusional creep. A general phenomenological description of the steady-state or minimum creep rate, $\dot{\varepsilon}_m$ had been given by Bird-Mukherjee–Dorn (BMD) equation [111], as

$$\dot{\varepsilon}_m = A_o \ \frac{D_\circ Eb}{kT} \exp\left(\frac{-Q_c}{RT}\right)\left(\frac{b}{d}\right)^p \left(\frac{\sigma_a}{E}\right)^n \tag{2.15}$$

where A_o is a dimensionless constant, $D_\circ$ the frequency factor, E the modulus of elasticity, b the Burgers vector, k the Boltzmann constant, Q_c activation energy for creep, R the universal gas constant, d the grain size, p the grain size exponent, σ_a applied stress and n the stress exponent. BMD equation gives better correlations to identify the rate controlling creep and builds the creep constitutive equation. The creep parameters of A_o, n, p and Q_c

37

in equation (2.15) could be employed to identify the creep mechanisms. ducing plastic deformation.

Table 2.2 summarizes the common creep mechanisms and the associated parameters [112]. Nabarro-Herring (N-H) and Coble creep mechanisms are categorized as diffusional creep while Harper-Dorn (H-D), viscous glide, dislocation climb and power-law breakdown creep (PLB) all involve dislocation motion for producing plastic deformation.

Table 2.2. Common creep mechanisms and the associated parameters [112].

Creep Mechanism	n	p	Q_c	A_o
Nabarro-Herring (N-H)	1	2	Q_L^*	12
Coble	1	3	Q_{gb}	150
Harper-Dorn (H-D)	1	0	Q_L	3×10^{-10}
Grain Boundary Sliding (GBS)	1	2	Q_{gb}	200
Viscous Glide	3	0	Q_s	6
Dislocation Climb	4 – 7	0	Q_L	6×10^7
Power Law Breakdown (PLB)	> 7	-	Q_L	-

* Q_L : Activation energy for lattice diffusion. Q_{gb} : Grain boundary diffusion. Q_s : Solute diffusion.

In this section, common creep mechanisms are briefly described, and a more detailed analysis is provided for dislocation climb mechanism as being particularly relevant for this research work.

• *Nabarro-Herring (N-H) and Coble creep*

At relatively low stresses and high temperatures and especially in fine-grained materials, creep deformation can be controlled only by the diffusion of atoms or vacancies and no dislocation motion is involved for producing strain [101, 104, 112]. Hence, the creep curve shows no primary creep or very small because of the absence of the work-hardening and recovery. Moreover, the creep rate increases linearly with the applied stress resulting in fluid-like (Newtonian viscous flow) with a stress exponent of 1. For Nabarro-Herring (N-H) creep,

the migration of atoms or vacancies occur through the lattice and hence the activation energy for N-H creep is equivalent to that for self-diffusion. Further, the creep rate is inversely proportional to the square of the grain size. Unlike N-H creep, Coble creep involves the diffusion of vacancies along the grain boundaries and the creep rate shows an inverse linear dependence to the cube of the grain size. Coble creep becomes dominant at lower stresses, lower temperatures and in smaller grain sized materials compared to N-H creep. In general, N-H creep and Coble creep take place in parallel within materials regardless of the grain size and therefore the faster process controls the creep rate.

- *Harper-Dorn creep*

Harper-Dorn (H-D) creep is observed in some materials at very high temperatures ($T \sim 0.99 T_m$). It also shows a Newtonian viscous flow with stress exponent of one; however, creep curve exhibits a distinct primary creep and the creep rate is grain size independent [113]. It becomes dominant over N-H creep with increased grain size [114]. The activation energy for H-D creep is equal to the lattice diffusion activation energy and edge-dislocation climb was suggested to be operative. However, a solid mechanism has not yet been agreed for H-D creep [115].

- *Grain boundary sliding*

Grain boundary sliding (GBS) has been reported to control the high temperature creep deformation at intermediate temperatures and small grain sizes. The creep rate during GBS deformation is characterized by grain size dependence and activation energy for that of grain boundary diffusion. Unlike N-H and Coble creep, the creep rate is proportional to the square of the applied stress and it occurs at stress levels slightly greater than that for diffusional creep. Langdon [116] developed a model for grain boundary sliding where sliding of grains occurs due to dislocation movement along or near the grain boundaries by a combination of climb and

glide. It has been shown that superplastic behavior with high tensile ductility of $> 1000\%$ can be achieved in equiaxed fine-grained materials (typically $\sim 10~\mu m$) when GBS is predominant [117].

- *Viscous glide creep*

As applied stresses increase, dislocations start to be generated from Frank-Reed sources and control creep deformation where both the dislocation glide and climb are involved. Unlike the deformation at low temperatures, the rate of dislocation climb, which requires the diffusion of atoms or vacancies, becomes significant. Since the glide and climb motion of dislocations occur as sequential processes (the dislocations first glide on their slip planes and then climb over obstacles), the slowest process controls the creep rate. However, the creep strain occurs during the glide process regardless of what controls the creep rate [118].

Viscous glide creep is characterized by the stress exponent of close to 3. The 3-power dependence of the creep rate on the applied stress may naturally be derived from the Orowan's equation (2.1). Assuming that, the $\bar{v}$ is proportional to σ and the Taylor equation relating ρ_m being proportional to σ^2 is valid, the creep rate follows as $\dot{\varepsilon} \propto \sigma^3$, known as natural creep law. Viscous glide creep is not observed in pure metals and only found to occur in various solid solution alloys, referred to as Class-I or Class-A alloys. The presence of the solute atoms slows down the gliding process by the segregation at dislocation cores making the dislocation glide to govern the creep rate with an activation energy that of solute atoms. The substructure for materials deformed in viscous glide creep regime reveals dislocations distributed throughout the matrix with no subgrain boundary formation. The creep curve in viscous glide mechanisms shows no or a little primary creep followed by steady-state regime. The sudden drop of the applied stress would result in a higher creep rate than that expected for the lower stress owing

to the larger dislocation density generated in the previous stress level. The creep rate, then, decreases until a steady state creep rate later in time is reached.

- *Dislocation climb*

In pure metals or Class-II or Class-M alloys, the rate of dislocation glide is relatively faster than that for diffusion-controlled clime process. Therefore, the dislocation climb acts as the rate controlling creep deformation in these materials. The main features of materials deformed in dislocation climb regime include a stress exponent of ~ 5, activation energy for creep equivalent to that of self-diffusion and the presence of well-defined subgrains. Unlike viscous glide creep, a large primary creep is usually obtained. Further, the effect of the sudden drop in the applied stress on the creep curve differs from that for viscous glide creep where the creep rate upon a stress reduction would result in a lower creep rate than that expected for lower stress owing to the smaller subgrain size. The creep rate then increases until a steady state creep rate is attained.
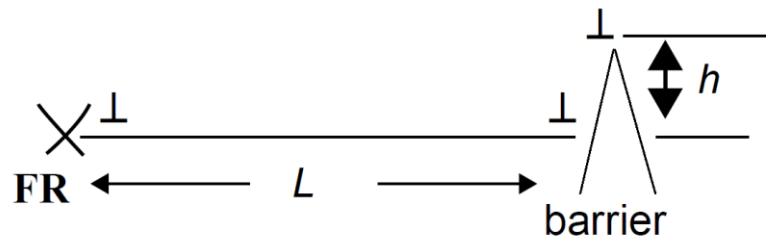
Figure 2.4. Schematic of dislocation glide-climb event [119].

Several mechanisms have been proposed to understand the underlying mechanism during dislocation climb-controlled creep. Weertman [120-122] has developed a model based on evaluating the rate of glide and climb for mobile dislocations. Figure 2.4 shows a schematic of dislocation glide-climb event where dislocation generated form FR sources glides on its slip plane to a distance, L (where the dislocation motion is impeded only by the Peierls frictional

stress) until it reaches a barrier of high, h which is surmounted by climb event and dislocation subsequently glides. Thus, the total strain, $\Delta\gamma$ and the total spent time for the glide-climb event are given by [104]

$$\Delta\gamma = \Delta\gamma_{glide} + \Delta\gamma_{climb} \approx \Delta\gamma_{glide} = \rho_m b L \tag{2.16}$$

$$t = t_{glide} + t_{climb} \approx t_{climb} = \frac{h}{v_c} \tag{2.17}$$

where v_c is the climb velocity. The strain rate can be evaluated by dividing equation (2.16) by (3.17). Gavin that

$$\rho_m \propto \sigma^2 \tag{2.19}$$

$$v_c \propto \Delta C_v \exp\left(\frac{-E_m}{kT}\right) \tag{2.20}$$

$$\frac{L}{h} \propto \sigma^{1.5} \tag{2.21}$$

where E_m the activation energy for vacancy migration, one can show that

$$\dot{\varepsilon} = A_1 D_L \sigma^{4.5} \tag{2.22}$$

where D_L is the lattice diffusivity and A_1 constant. Equation (2.22) agrees very well with experimental results of pure metals and other alloys. At lower temperatures, a stress exponent of 7 may be obtained with activation energy less than that for self-diffusion suggesting the low-temperature dislocation climb controlling the creep with the dominance of dislocation core diffusion [123]. Subgrain formation has been commonly considered as microstructural evidence for the creep due to climb of edge dislocations for various metals and alloys. According to Weertman model [122], edge dislocation dipoles are formed due to the intersections of dislocations originating from different sources of a given density. These dipoles are annihilated towards each other by dislocation climb assisted by lattice diffusion to form both low angle tilt and twist boundaries resulting in subgrain formation.

- *Power-law breakdown*

At very high stresses and intermediate temperatures, a stress exponent of much higher than 5 is observed, also referred to as 'power law breakdown (PLB)' regime. At such higher stresses, dislocations generated greater than predicted by the Taylor equation [104] and thus exponential dependence of strain rate on stress appears in PLB regime. The activation energy in this regime has been found to be the same as the activation energy for self-diffusion and sometimes reported to have an activation energy for that of pip diffusion. Breaking subgrain boundaries, cross slip and cutting of forest dislocation have been suggested to be operative in the PLB regime. However, the creep deformation mechanism in this regime is not clearly resolved probably due to a relatively small number of studies carried out in this regime which only occurs at small regions at very high stresses [104].

- *Transitions in creep mechanisms*

For a given material, a transition in the rate controlling creep mechanisms may occur as a function of the applied stress. Figure 2.5 shows a schematic for the transitions in creep mechanisms as a function of the applied stress in Class-M and Class-A alloys using the BMD equation (2.15). In pure metals and Class-M alloys, a stress exponent of 1 is observed at low stresses implying the occurrence of diffusional creep (either N-H creep through lattice or Coble creep along grain boundaries) or H-D creep, depending on the temperature and grain size. At intermediate stresses, climb of dislocations controls the creep mechanisms and PLB regime appears as stresses get higher.
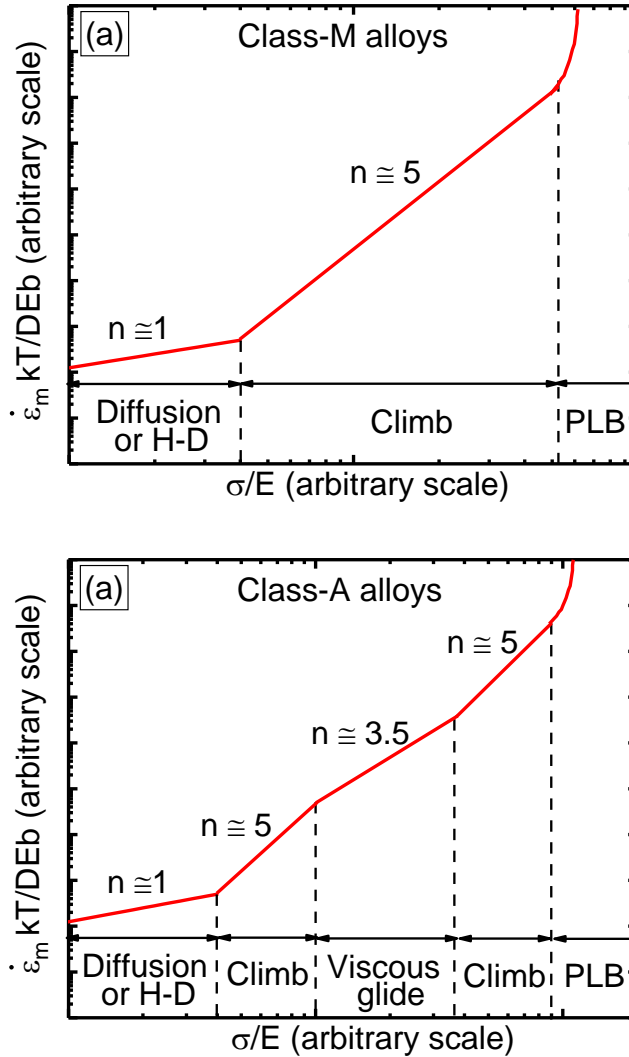
Figure 2.5. Transitions in creep mechanisms as a function of the applied stress in (a) class-M alloys and (b) class-A alloys.

In some solid solution alloys or class-A alloys, the transitions in creep mechanism look interesting. As in pure metals and class-M alloys, Class-A alloys exhibit viscose creep of stress exponent of 1 at lower stresses followed by a transition to the dislocation climb mechanism at slightly higher stresses indicating that the climb process is still slower than glide process. As stress increases further, however, the climb rate increases and together with the glide motion by the presence of solute atoms, glide process becomes slower and viscous glide appears to control the creep deformation. With further increase in stress and before entering PLB regime, a transition from viscous glide creep into dislocation climb may occur due to the breaking away

of the dislocations from the solute atmospheres. It has been shown that this breakaway stress is in the range of $2\times10^{-4}E-1\times10^{-3}E$ which is close to the range where PLB occurs [124].

Noting that, the transitions in creep mechanisms for both classes of alloys may become more complicated, for example, an intervening GBS regime with stress exponent of 2 may appear between viscous creep (diffusional creep or H-D creep) and the dislocation climb regime.

2.3.3. Creep in precipitation-hardened alloys

The change in the solid solubility with temperature in alloys can produce fine second phase particles with different types and sizes in the matrix so-called precipitates. The precipitates in the solid matrix act as effective obstacles to the dislocation movement even at high temperatures, and hence they can enhance the creep properties [101]. The particle characteristics including volume fraction, size, shape, crystal structure and coherency play an important role in determining the increase in the material strength [119]. At low temperatures, dislocations are believed to bypass the particles intersected within its glide plane either by cutting or shearing particles (typically for small coherent particles) or by Orowan bowing between particles (typically for large incoherent particles) where both processes are considered to be athermal [125]. However, diffusional mass transport occurs during high temperature creep deformation and a process of dislocation bypassing the particles by climb is of importance in precipitation-hardened alloys [101, 125-128]. The creep characteristics for precipitation-hardened alloys includes higher (>5) stress exponents even though the stresses and temperature levels are in the power law regime (a stress exponent as high as 40 has been reported in thoriated nickel [129]), much higher activation energy for creep relative to that of self-diffusion and microstructure with dislocation-precipitate interactions. Subgrains may or

may not form during creep in precipitation-hardened alloys.
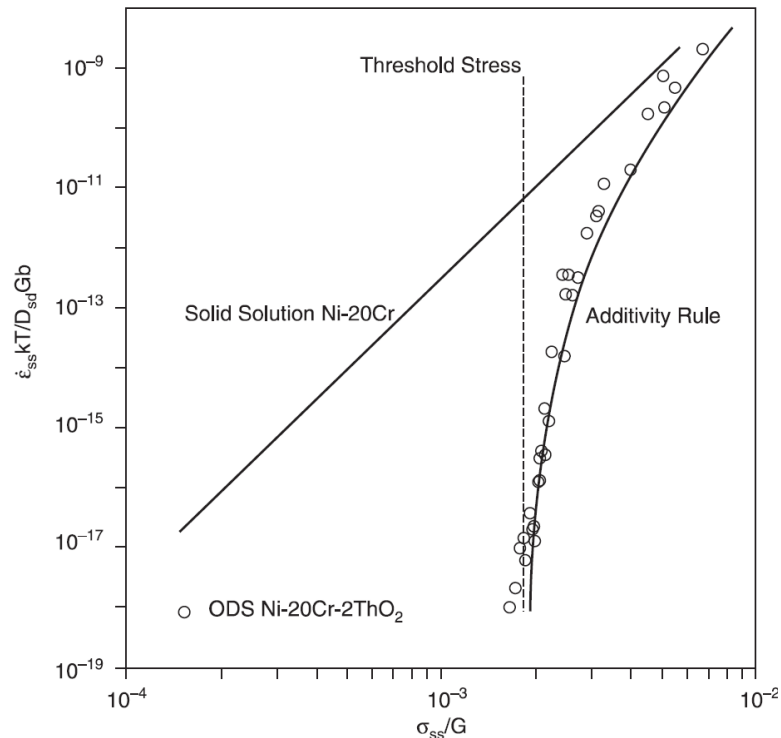
Figure 2.6. The normalized steady-state creep-rate versus modulus compensated stress showing the effect of particle-strengthening on creep rate [125].

The effect of particle strengthening on creep is illustrated in Figure 2.6 where the normalized steady-state creep-rate versus modulus compensated stress is plotted for both a Ni–Cr solid solution matrix and oxide dispersoids (ThO$_2$) in the Ni–Cr solid solution matrix. To rationalize the high values of apparent stress exponent or unrealistic apparent activation energy for creep based on current existing creep mechanisms, the concept of the *threshold stress, σ_{th}* or back stress has been frequently introduced in precipitation-hardened alloys where σ_{th} is associated with the particle by-pass mechanism [101, 125-128]. Thus, the steady state or minimum creep rate is expressed in terms of the effective stress, σ_{eff} instead of the applied stress, σ_a where the σ_{eff} is the difference between the σ_a and the threshold stress, σ_{th}. Then, providing that the activation energy for self-diffusion is operative during creep, the BMD

46

equation (2.15) for dislocation creep can be modified to express the creep rate in precipitation-hardened alloys as follows,

$$\dot{\varepsilon}_m = A_c \frac{D_\circ Eb}{kT} \exp\left(\frac{-Q_c}{RT}\right) \left(\frac{\sigma_a - \sigma_{th}}{E}\right)^n \qquad (2.23)$$

where now the values for the stress exponent, n are in the range of power-law creep indicating that the creep process in precipitation-hardened alloys is closely related to those in single phase systems. Equation (2.23) has been commonly utilized to identify the operating creep mechanism(s) in precipitation-hardened alloys. The values for the threshold stresses can be estimated using the linear extrapolation method [130-132], where a linear plot of $\dot{\varepsilon}_m^{1/n'}$ versus σ is made at a given temperature where n' is an assumed stress exponent value that is varied to cover all possible creep mechanisms. The intercept of the linear extrapolation of data to zero creep rate with the stress axis provides the σ_{th}. The choice of true stress exponent value, n must satisfy the best correlation coefficient of the linear fit as well as the corresponding activation energy for a given creep mechanism. Further, σ_{th} can also be estimated experimentally using stress-dip test where the incubation period after the sudden reduction in the stress is calculated and the plot of accumulated stress reduction versus the accumulated incubation period determines the σ_{th} [101, 133]. However, the incubation period may not be observed or rarely measured in some precipitation-hardened alloys [101].

- *Theoretical approaches to the threshold stress and associated mechanisms*

The threshold stress, σ_{th} originates from the stress imparted on the dislocations by the precipitates during glide and climb processes. Several mechanisms have been proposed to estimate the threshold stress theoretically taking into account the volume fraction, size and the type of precipitates as well as the type of interaction between dislocations and precipitates.

Figure 2.7 illustrates different mechanisms by which a dislocation can surmount second phase particles during creep deformation [134]. The associated formulae for the threshold stress for different dislocation bypassing mechanisms are summarized in Table 2.3 [126, 127, 134-137]. In all models, the values of the threshold stress are found to be inversely proportional to the mean interparticle spacing, λ.

The athermal process of dislocation bypassing the particles by forming loops around them (i.e. Orowan bowing mechanism) was reported to occur during creep deformation [138]. However, threshold stress is usually found to be lower than Orowan stress required to bow around precipitates and the Orowan mechanism seems to be operative at high stresses [101, 125, 128]. Ashby developed a model based on Orowan mechanism but taking into account the mutual interaction between the bowed out segments where it reduces the magnitude of the Orowan stress, typically by a factor between 0.5 and 0.7 [135].

Further, the process of dislocations bypassing participates by climbing over particles is later considered involving diffusional mass transport. This mechanism requires detailed analysis of the nature of the interaction between the dislocations and the precipitates. The climb of dislocations around a group of precipitates can be classified into two general terms; namely local climb or general climb [101, 125]. For local climb, only the portion of the dislocation segment in the particle-matrix interface climbs while the dislocation segments between particles remain on their slip plane. The threshold stress follows from the increase in the dislocation segment due to climb within particle-matrix interface which is needed to compensate for this increment of dislocation length. For general climb, all dislocations climb out of their glide planes, which requires a smaller increase in the total length relative to that of the local climb.
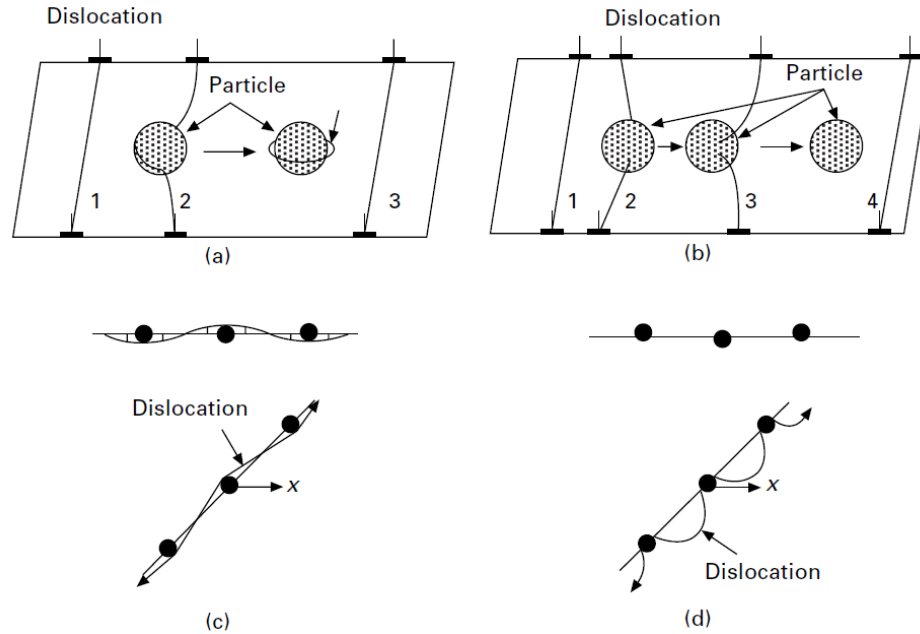
Figure 2.7. Schematic of different mechanisms by which dislocation can surmount second phased particles during creep deformation. (a) Orowan mechanisms, (b) Srolovitz's mechanism, (c) general climb mechanism and (d) local climb mechanism [134].

Srolovitz et al., developed a model based on the attractive interaction in the interface between the particle and dislocation where a relaxation of the dislocation core leading to the pinning of dislocation gives rise to the threshold stress for creep [127]. The local climb of dislocation over a precipitate is dominant over the general climb in Srolovitz's mechanism. Arzt and Wilkinson [136] also considered the attractive interaction between dislocations and spherical particles; however, the threshold stress arises from the detachment of the dislocation from the particle after climb regardless of whether the type of climb is either local or general. Unlike other models, Arzt and Wilkinson showed that the particle size is not of great importance for determining the threshold stress but only the mean interparticle spacing, λ. Further, a threshold stress based on the increasing length of dislocation was given by Evans and Knowles [126] where it is weakly dependent on the applied stress while strongly dependent on particle size to mean interparticle spacing ratio. Mishra et al., [137] have also proposed a model for the threshold stress based on the attractive dislocation-particle interaction where the

49

local climb process involves the dissociation of lattice dislocations into interfacial dislocations, when they enter the matrix-particle interface.

It should be mentioned that the threshold stress evaluated from the aforementioned models are not fully consistent with the threshold stresses determined experimentally and further understanding of creep in precipitation-hardened alloys is required. Furthermore, the these models have taken into account only the particles within grains; however, the presence of second phases along grain boundaries may also occur in precipitation-hardened alloys and inhibit the diffusional creep and GBS [139, 140]. The precipitates at grain boundaries may affect the ease of grain boundaries as vacancy sources and sinks, which may give rise to an additional back stress [6, 139, 140].

2.3.4. Creep mechanisms in austenitic stainless steels

Several creep mechanisms are known to control the rate of deformation in austenitic stainless steels including dislocation-controlled creep or diffusional creep and their associated mechanisms. Data from published literature for the values of apparent stress exponents and activation energies along with suggested creep mechanisms for various austenitic stainless steels are compiled in Table 2.4 [6, 133, 141-152].

In type 304 stainless steel, Chopra and Natesan [133] studied the creep behavior at temperatures of 873 – 973 K and stresses of 55 to 240 MPa, and reported values for the apparent stress exponent and activation energy for creep of 5.6 – 6.5 and 334 – 385 kJ/mole respectively. They interpreted the glide-recovery as the rate controlling mechanism with a true stress exponent of 2.3 – 3.3 where the steady-state creep rate was interpreted as a function of the mean effective, σ_{eff} rather than the applied stress, σ_a as, $\sigma_{eff} = \sigma_a - \sigma_i$ where σ_i is the internal stress arising from the elastic interaction between the barriers and moving dislocations

(athermal component). They measured the effective stress using strain dip tests and found to be $\sigma_i = \alpha\sigma_a{}^{\beta}$, where the constants α and β depend on temperature. The dependence of creep rate on effective stress during high-temperature deformation was described in terms of viscous glide creep mechanism.

Table 2.3. Theoretical models for the threshold stress, σ_{th} in precipitation-hardened alloys [127, 134-137].

σ_{th} (MPa)	Model	Ref.
$0.8MGb/\lambda$	Orowan bowing around precipitates.	[134]
$\dfrac{MGb}{2\pi(1-v)\lambda}\left(\ln(2)+\ln\left(\dfrac{r}{r_\circ}\right)\right)$	Ashby's model.	[135]
$\dfrac{8\Gamma r}{3\lambda b}\sqrt{\left\{r^2+\left[\dfrac{4\Gamma}{\sigma_a b}\sin^{-1}\left(\dfrac{\sigma_a b\lambda}{8\Gamma}\right)\right]^2\right\}}$	Evans and Knowles	[126]
$\dfrac{MGb}{\lambda}\sqrt{1-k^2}$	Detachment mechanism (local or general).	[136]
$MGC\dfrac{B}{\lambda}\exp\left(B\dfrac{r}{\lambda}\right)$	Dislocation dissociation (local climb).	[137]
$\dfrac{MGb}{2\pi(1-v)\lambda}\left(\dfrac{\pi^2}{12}+\ln\left(\dfrac{r}{r_\circ}\right)\right)$	Srolovitz's mechanism (local climb).	[127]

G shear modulus, $M \sim 3$(Taylor factor), $v \sim 0.3$(Poisson's ratio), r average radius of the particles, $r_\circ \sim b$ (dislocation core radius), λ interparticle spacing, Γ dislocation line energy, $C \sim 0.002$ and $B \sim 20$ constant for Mishra model and $k \sim 0.3$ constant for Arzt model.

In type 316 stainless steel, Kestenbach *et al.,* [144] suggested that thermally activated cross-slip was the rate controlling creep mechanism at high stresses (130 MPa – 380 MPa) and temperatures in the range 873 - 1073 K while the dislocation climb is the rate controlling creep at low stresses (60 MPa – 130 MPa) accompanied with evidence for the subgrain formation. However, the absence of subgrains in the secondary creep regime has been reported by Beckitt *et al.*, in 304SS with higher carbon content and ascribed to precipitates formed during creep

tests [8]. They have studied the microstructure following creep tests in two of 304SSs with different carbon contents. The higher carbon content in 304SS was found to increase the $M_{23}C_6$ particles formed during creep and decrease the dislocation mobility within grains resulting in the absence of the subgrain formation.

Morris and Harries [153] have shown that the dislocation junctions and the climb of jogs on the moving dislocation to be the rate controlling creep in type 316 steel over the temperature range 848 to 1173 °C while the creep is controlled by the solute-dislocation interaction leading to dislocation locking at 798 K and higher stresses.

In precipitation hardened stainless steel (TiN-dispersion strengthened Fe-20%Cr-25%Ni SS), Roberts and Evans [146] have reported that the creep was controlled by the separation between the TiN particles in the matrix and the creep rate could be described by the equation of the form $\dot{\varepsilon}_{ss} = B \left(\sigma_a - \sigma_{th} \right)^4$, where the threshold stress σ_{th} was assumed to be the Orowan stress, σ_O when $\sigma_a > \sigma_O$. For $\sigma_a < \sigma_O$, Evans and Knowles [126] have derived an expression for σ_{th} based on the increasing length of dislocation and shown that the ratio of σ_{th} / σ_O changes from 0 to 0.75 with changing the dispersion parameter r / λ from 0 to 1 respectively. They concluded that the threshold stress can be considered to be a unique property of a given dispersion [126]. So, the creep mechanism in dispersion strengthened Fe-20%Cr-25%Ni stainless steel was the dislocation bypassing the particles by climb process and hence the recovery; however, a critical threshold stress is needed to maintain the minimum length increase during climb process.

In Nb-stabilized type 347 stainless steel, Russell *et al.,* [154] observed a transition in creep mechanism at a stress near the yield stress (around 70 MPa) and over temperatures 823 – 1048 K. They suggested that a cross-slip recovery process is the rate controlling creep above

52

70 MPa while at lower stresses creep is controlled by the diffusion of solutes attached to dislocations. Satyanarayana *et al.,* [148] studied the steady-state creep behavior of NiAl hardened austenitic steel over a temperature range of 823 – 923K and at stresses ranging from 150 to 500 MPa. Two distinct regimes of creep deformation were found with an apparent stress exponent of 10 – 12 at high stresses and 6 – 7 at low stresses. They invoked the threshold stress concept at high stresses and used the linear extrapolation method [130] to estimate the values of threshold stress as a function of temperature to obtain a true stress exponent of 7. They suggested that the creep is controlled by the recovery due to low-temperature climb of dislocations over NiAl precipitates assisted by dislocation core diffusion and they attributed the transition in stress exponents to the change in dislocation bypass mechanism from Orowan bowing in the high-stress regime to general climb over the precipitates in the low-stress regime.

Recently, creep behavior of Super304H austenitic steel (type 304 with about 3% Cu and a small amount of Nb) has been investigated at elevated temperatures of 923 – 973 K and applied stresses of 190 – 210 MPa by Ou *et al.,* [152]. The apparent stress exponent and activation energy were found to be 16.2 to 27.4 and 600 to 770 kJ/mole respectively. They attributed these high values to the presence of a threshold stress due to an interaction between the dislocations and Cu-rich precipitates during creep deformation. The origin of the threshold stress was mainly attributed to the coherency strains induced in the matrix by Cu-rich precipitates. They theoretically estimated the threshold stresses from coherent Cu-rich precipitates using a model developed by Krug and Dunand [155] for the creep threshold stress due to climb of a dislocation in the stress field of a misfitting precipitate. The results agree reasonably well with the experimental values obtained by linear extrapolation method.

Creep behaviors of the solution-treated AL6XN austenitic stainless steel [150] have

been investigated at 873 – 1023 K and 120 – 260 MPa where the stress exponent and the activation energy of the AL6XN steel were found to be 5 and 395 kJ/mole, respectively. The creep deformation mechanism was mainly attributed to viscous dislocation glide.

Diffusional creep has also been observed to occur in austenitic stainless steels at low stresses. For example, Crossland and Clay [142] showed that the diffusional creep in 20Cr-25Ni-Nb-stabilized stainless steel at stresses below 20 MPa and over temperatures 973 – 1123 K (using helical spring specimens of 14 - 20 μm grain size) can be represented by Coble creep at a very low strain. However, with the strain increasing, they observed the creep rates falling below those predicted by the Coble theory. The major part of this diffusion creep suppression was attributed to the decrease in the effective viscosity. They proposed the Nabarro-Herring creep with σ_{th} decreasing from 6 to 1.5 MPa with increasing temperature. On the same steel, Knowles [143] reported a transition in a stress exponent from 10 to 1 at 60 MPa and 1073 K. Coble creep was suggested as the creep mechanism at low stresses (below 60 MPa) and the experimental data agreed to within a factor of three with Coble theory. A grain size exponent of 3 was reported in this steel (with 0.02% C) at 70 MPa and 1023 K [156]. The observed minimum creep rates were varied between one and one-tenth below those predicted by Coble creep depending on the Nb:C ratio.

In type 304 stainless steel, diffusional creep at stresses below 30 MPa and over temperatures 873 - 1023 K with a grain size of 60 μm was reported by Beckitt [8]. The results agreed with Coble creep; however, the diffusional creep was inhibited by increasing the carbon content from 0.015% to 0.056%. Lagneborg and Attermo [141] have attributed the departure from power-law creep to a stress exponent of 2 – 3 at 1023 K and in the range 10- 100 MPa to the grain boundary sliding mechanism although creep rates were more than one order of magnitude

below those predicted by diffusional creep. Sritharan and Jones [145] found that the creep behavior in type 304 steel (12 μm grain size) followed Coble creep below 10 MPa and over temperatures 823 – 1023 K (0.49 to 0.61 T_M) with increasing threshold stress from 0.1 MPa to 3 MPa with decreasing temperature due to the $M_{23}C_6$ precipitates on grain boundaries. Same creep mechanism by incorporating a threshold stress was proposed by Yamane *et al.,* [157] in 25Cr-20Ni steel doped with antimony. It was found that the threshold stress increased with increasing antimony content due to the segregation of antimony to grain boundaries retarding the diffusional creep. However, the results by Sritharan and Jones [145] and by Yamane *et al.,* [157] based on diffusional Coble creep with threshold stress have been disputed by Ruano and Sherby [158]. They proposed that the creep mechanism at that range of stresses and temperatures appeared to be controlled by grain boundary sliding, GBS, accommodated by slip rather than by diffusional (Coble) creep. Plots of creep rate versus stress on a double-linear scale suggested that no threshold stress for creep is observed in austenitic stainless steel when grain boundary sliding and slip mechanisms are taken into account.

Table 2.4. Apparent stress exponents and activation energies along with suggested creep mechanisms for various austenitic stainless steels from published literature [6, 133, 141-152].

Material	Range of stresses (MPa)	Range of temperatures (K)	Apparent stress exponent, n_a	Apparent activation energy, Q_a (kJ/mole)	Suggested creep mechanism	Ref.
304H	190 – 210	923 – 1023	16– 27	602 – 769	Dislocation climb over the Cu-rich precipitates.	[152]
Fe–Ni–Cr–Al	150 – 500	823 – 923	6 – 12	165 - 282	Low temperature dislocation climb.	[148]
AISI 347	50 – 196	898 – 1098	8.8	434	Dislocation climb over Nb-rich particles.	[147]
Super304H	120 – 250	923 – 1073	6 – 6.8	460 – 485	Various strengthening particles MX-Z-phase and Cu precipitates.	[151]
Type 304SS	55 – 240	873 – 973	5.6 – 6.5	334 – 385	Viscous-glide	[133]
Fe-15Cr-25Ni-0.086C	15 – 100	1123 – 1223	7	449	Combined matrix/boundary strengthening by carbide	[6]
AL6XN	120 – 260	923 – 1023	5.8 – 7.4	380 – 415	Viscous dislocation glide	[150]
Fe-20Cr-25Ni	103 – 241	1023 – 1123	-	-	Climb over TiN particles	[146]
316SS	60 – 380	873 – 1073	7	-	Climb ($\sigma_a < 130$ MPa) and Cross-slip (higher stresses)	[144]
HR6W	85 – 200	923 – 1073	7.4	428	Precipitate-dislocation interactions	[149]
Fe-20Cr-35Ni	10 – 100	1023			Grain Boundary Sliding (GBS)	[141]
Fe-20Cr-25Ni	< 20	973 – 1123	1 – 3	127 – 265	Nabarro-Herring	[142]
Fe-20Cr-25Ni	< 60	1123	~1	-	Coble (later was suggested to be GBS)	[143]
304SS	< 10	823 – 1023	1 – 2.5	227	Coble (disputed by Sherby [158] and suggested GBS)	[145]

2.4. References

[1] K.L. Murty, I. Charit, Structural materials for Gen-IV nuclear reactors: Challenges and opportunities, Journal of Nuclear Materials 383 (2008) 189-195.

[2] P. Marshall, Austenitic Stainless Steels: Microstructure and mechanical properties, Elsevier Applied Science1984.

[3] P.J. Maziasz, J.T. Busby, Properties of Austenitic Steels for Nuclear Reactor Applications, in: R.J.M. Konings (Ed.), Comprehensive Nuclear Materials, Elsevier, Oxford, 2012, pp. 267-283.

[4] K.H. Lo, C.H. Shek, J.K.L. Lai, Recent developments in stainless steels, Materials Science and Engineering: R: Reports 65 (2009) 39-104.

[5] T. Sourmail, Precipitation in creep resistant austenitic stainless steels, Materials Science and Technology 17 (2001) 1-14.

[6] J.S. Zhang, P.E. Li, J.Z. Jin, Combined matrix/boundary precipitation strengthening in creep of Fe-15 Cr-25 Ni alloys, Acta Metallurgica et Materialia 39 (1991) 3063-3070.

[7] K.H. Mayer, F. Masuyama, The development of creep-resistant steels, in: F. Abe, T.-U. Kern, R. Viswanathan (Eds.), Creep-Resistant Steels, Woodhead Publishing 2008, pp. 15-77.

[8] F.R. Beckitt, T.M. Banks, T. Gladman, Secondary creep deformation in 18%Cr-10%Ni steel, Creep strength in steel and high temperature alloys, The Metal Society, London, 1972, pp. 71-77.

[9] M.D. Mathew, Evolution of creep resistant 316 stainless steel for sodium cooled fast reactor applications, Transactions of the Indian Institute of Metals 63 (2010) 151-158.

[10] J.W. Simmons, Overview: high-nitrogen alloying of stainless steels, Materials Science and Engineering: A 207 (1996) 159-169.

[11] G. Alden, B. Aronsson, Some observations on the influence of carbon and nitrogen on the creep befavior of AISI 316 type austentic stainless steels, Creep strength in steel and high temperature alloys, The Metal Society, London, 1972, pp. 67-70.

[12] M.D. Mathew, V. Ganesan, J.G. Kumar, K. Laha, Creep properties and design curves fornitrogen enhanced grade of 316LN stainlesssteel, Materials at High Temperatures 32 (2015) 363-368.

[13] J.M. Admason, J.W. Martin, Effect of niobium content on the steady state creep of stabilized 20%Cr-25%Ni austenitic stainless steels, Creep strength in steel and high temperature alloys, The Metal Society, London, 1972, pp. 99-105.

[14] S. Latha, M.D. Mathew, P. Parameswaran, M. Nandagopal, S.L. Mannan, Effect of titanium on the creep deformation behaviour of 14Cr–15Ni–Ti stainless steel, Journal of Nuclear Materials 409 (2011) 214-220.

[15] V. Vodárek, Creep behaviour and microstructural evolution in AISI 316LN+Nb steels at 650°C, Materials Science and Engineering: A 528 (2011) 4232-4238.

[16] M.F. McGuire, Austenitic Stainless Steels, Stainless Steels for Design Engineers, ASM International, Materials Park, OH, 2008.

[17] R.V. Nandedkar, W. Kesternich, Effect of boron on high-temperature creep behavior of austenitic stainless steel DIN 1.4970, Metallurgical Transactions A 21 (1990) 3033-3038.

[18] J.P. Shingledecker, P.J. Maziasz, N.D. Evans, M.J. Pollard, Creep behavior of a new cast austenitic alloy, International Journal of Pressure Vessels and Piping 84 (2007) 21-28.

[19] Y. Zhou, Y. Li, Y. Liu, Q. Guo, C. Liu, L. Yu, C. Li, H. Li, Precipitation behavior of type 347H heat-resistant austenitic steel during long-term high-temperature aging, Journal of Materials Research 30 (2015) 3642-3652.

[20] A.F. Padilha, P.R. Rios, Decomposition of Austenite in Austenitic Stainless Steels, ISIJ International 42 (2002) 325-327.

[21] B. Peng, H. Zhang, J. Hong, J. Gao, H. Zhang, J. Li, Q. Wang, The evolution of precipitates of 22Cr–25Ni–Mo–Nb–N heat-resistant austenitic steel in long-term creep, Materials Science and Engineering: A 527 (2010) 4424-4430.

[22] N.D. Evans, P.J. Maziasz, J.P. Shingledecker, M.J. Pollard, Structure and Composition of Nanometer-Sized Nitrides in a Creep-Resistant Cast Austenitic Alloy, Metallurgical and Materials Transactions: A 41 (2010) 3032-3041.

[23] T. Sourmail, H.K.D.H. Bhadeshia, Microstructural evolution in two variants of NF709 at 1023 and 1073 K, Metallurgical and Materials Transactions: A 36 (2005) 23-34.

[24] A. Portevin, F. LeChatelier, Heat treament of aluminum-coopper alloys, Transactions of the American Society for Steel Treating 530 (1924) 457-478.

[25] P. Rodriguez, Serrated plastic flow, Bulletin of Materials Science 6 (1984) 653-663.

[26] S.L. Mannan, P. Rodriguez, Strain-ageing in disordered CuAu, The Philosophical Magazine: A Journal of Theoretical Experimental and Applied Physics 25 (1972) 673-686.

[27] F.A. Mohamed, K.L. Murty, T.G. Langdon, The portevin-le chatelier effect in Cu3Au, Acta Metallurgica 22 (1974) 325-332.

[28] L. Yuan, R. Hu, J. Li, X. Zhang, Y.a. Yang, Portevin-Le Chatelier effect in a Ni–Cr–Mo alloy containing ordered phase with Pt2Mo-type structure at room temperature, Materials Science and Engineering: A 650 (2016) 317-322.

[29] G.F. Bolling, R.H. Richman, Continual mechanical twinning: Part I: Formal description, Acta Metallurgica 13 (1965) 709-722.

[30] M. Koyama, T. Sawaguchi, K. Tsuzaki, Deformation Twinning Behavior of Twinning-induced Plasticity Steels with Different Carbon Concentrations – Part 2: Proposal of Dynamic-strain-aging-assisted Deformation Twinning, ISIJ International 55 (2015) 1754-1761.

[31] V. Seetharaman, Deformation and martensitic transformation, Bulletin of Materials Science 6 (1984) 703-716.

[32] V. Ramachandran, D.H. Baldwin, R.E. Reed-Hill, Tensile behavior of polycrystalline zirconium at 4.2°K, Metallurgical Transactions 1 (1970) 3011.

[33] L.P. Kubin, P. Spiesser, Y. Estrin, Computer simulation of the low temperature instability of plastic flow, Acta Metallurgica 30 (1982) 385-394.

[34] P. Rodriguez, S. Venkadesan, Serrated Plastic Flow Revisited, Solid State Phenomena 42-43 (1995) 257-266.

[35] K.L. Murty, I. Charit, Static strain aging and dislocation–impurity interactions in irradiated mild steel, Journal of Nuclear Materials 382 (2008) 217-222.

[36] E. Pink, A. Grinberg, Serrated flow in a ferritic stainless steel, Materials Science and Engineering 51 (1981) 1-8.

[37] J.M. Robinson, M.P. Shaw, Microstructural and mechanical influences on dynamic strain aging phenomena, International Materials Reviews 39 (1994) 113-122.

[38] A.H. Cottrell, B.A. Bilby, Dislocation Theory of Yielding and Strain Ageing of Iron, Proceedings of the Physical Society. Section A 62 (1949) 49.

[39] A.H. Cottrell, LXXXVI. A note on the Portevin-Le Chatelier effect, The London, Edinburgh, and Dublin Philosophical Magazine and Journal of Science 44 (1953) 829-832.

[40] Dislocations and Plastic Flow in Crystals, American Journal of Physics 22 (1954) 242-243.

[41] R.K. Ham, D. Jaffrey, Dislocation multiplication, vacancy accumulation, and the onset of jerky flow during forward and reverse 1 strain in Cu-3.2 at. % Sn, The Philosophical Magazine: A Journal of Theoretical Experimental and Applied Physics 15 (1967) 247-256.

[42] K.L. Murty, K. Detemple, O. Kanert, J.T.M. Dehosson, In-situ nuclear magnetic resonance investigation of strain, temperature, and strain-rate variations of deformation-induced vacancy concentration in aluminum, Metallurgical and Materials Transactions: A 29 (1998) 153-159.

[43] P.G. McCormick, A model for the Portevin-Le Chatelier effect in substitutional alloys, Acta Metallurgica 20 (1972) 351-354.

[44] A.V.D. Beukel, On the mechanism of serrated yielding and dynamic strain ageing, Acta Metallurgica 28 (1980) 965-969.

[45] A. van den Beukel, Theory of the effect of dynamic strain aging on mechanical properties, Physica Status Solidi A Applications and Material Science 30 (1975) 197-206.

[46] L.P. Kubin, Y. Estrin, Dynamic strain ageing and the mechanical response of alloys, Journal de Physique III 1 (1991) 929-943.

[47] S. Fu, T. Cheng, Q. Zhang, Q. Hu, P. Cao, Two mechanisms for the normal and inverse behaviors of the critical strain for the Portevin–Le Chatelier effect, Acta Materialia 60 (2012) 6650-6656.

[48] R. Sarmah, G. Ananthakrishna, Correlation between band propagation property and the nature of serrations in the Portevin–Le Chatelier effect, Acta Materialia 91 (2015) 192-201.

[49] R.C. Picu, A mechanism for the negative strain-rate sensitivity of dilute solid solutions, Acta Materialia 52 (2004) 3447-3458.

[50] W.A. Curtin, D.L. Olmsted, L.G. Hector Jr, A predictive mechanism for dynamic strain ageing in aluminium–magnesium alloys, Nature Materials 5 (2006) 875.

[51] S. Venkadesan, C. Phaniraj, P.V. Sivaprasad, P. Rodriguez, Activation Energy For Serrated Flow In A 15Cr-15Ni Ti-Modified Austenitic Stainless Steel, Acta Metallurgica et Materialia 40 (1992) 569-580.

[52] K.R. Narendrnath, H. Margolin, Y.H. Jung, P.S. Godavarti, K.L. Murty, A personal computer based system to evaluate J-integral by a single specimen unloading compliance method—part II: Results on A533B class I steel and corona-5, Engineering Fracture Mechanics 30 (1988) 349-359.

[53] S.I. Hong, W.S. Ryu, C.S. Rim, Elongation Minimum and Strain Ram Sensitivity Minimum of Zircaloy-4 Journal of Nuclear Materials 116 (1983) 314-316.

[54] B.K. Choudhary, Influence of Strain Rate and Temperature on Tensile Deformation and Fracture Behavior of Type 316L(N) Austenitic Stainless Steel, Metallurgical and Materials Transactions: A 45 (2014) 302-316.

[55] E. Bouchaud, L. Kubin, H. Octor, Ductility and dynamic strain aging in rapidly solidified aluminum alloys, Metallurgical Transactions: A 22 (1991) 1021-1028.

[56] M. Doner, H. Conrad, Deformation mechanisms in commercial Ti (0.5 at. pct oineq) at intermediate and high temperatures (0.3 - 0.6 tinm), Metallurgical Transactions 4 (1973) 2809-2817.

[57] C. Gupta, J.K. Chakravartty, S.L. Wadekar, J.S. Dubey, Effect of serrated flow on deformation behaviour of AISI 403stainless steel, Materials Science and Engineering: A 292 (2000) 49-55.

[58] D.J. Michel, J. Moteff, A.J. Lovell, Substructure of type 316 stainless steel deformed in slow tension at temperatures between 21° and 816°C, Acta Metallurgica 21 (1973) 1269-1277.

[59] K.G. Samuel, S.K. Ray, G. Sasikala, Dynamic strain ageing in prior cold worked 15Cr–15Ni titanium modified stainless steel (Alloy D9), Journal of Nuclear Materials 355 (2006) 30-37.

[60] X. Xiong, D. Quan, P. Dai, Z. Wang, Q. Zhang, Z. Yue, Tensile behavior of nickel-base single-crystal superalloy DD6, Materials Science and Engineering: A 636 (2015) 608-612.

[61] B.J. Brindley, The Effect of Dynamic Strain Ageing on the Ductile Fracture Process in Mild Steel, Acta Metallurgica 18 (1970) 325-329.

[62] S. Mahmood, K. Al-Otaibi, Y. Jung, K. Linga Murty, Dynamic Strain-Aging and Neutron Irradiation Effects on Mechanical and Fracture Properties of A533B Class 1 PV Steel and 2.25Cr-1Mo Steel, Journal of Testing and Evaluation 18 (1990) 332-337.

[63] M. Srinivas, G.Malakondaiah, K.L. Murty, P.R. Rao, Fracture Toughness in the Dynamic Strain Ageing Regime, Scripta Metallurgica et Materialia 25 (1991) 2585-2588.

[64] C.S. Seok, K.L. Murty, Effect of dynamic strain aging on mechanical and fracture properties of A516Gr70 steel, International Journal of Pressure Vessels and Piping 76 (1999) 945–953.

[65] J.H. Yoon, B.S. Lee, Y.J. Oh, J.H. Hong, Effects of loading rate and temperature on J–R fracture resistance of an SA516-Gr.70 steel for nuclear piping, International Journal of Pressure Vessels and Piping 76 (1999) 663-670.

[66] P. Verma, G. Sudhakar Rao, P. Chellapandi, G.S. Mahobia, K. Chattopadhyay, N.C. Santhi Srinivas, V. Singh, Dynamic strain ageing, deformation, and fracture behavior of modified 9Cr–1Mo steel, Materials Science and Engineering: A 621 (2015) 39-51.

[67] R.D. Warda, V. Fidleris, E. Teghtsoonian, Dynamic strain aging during creep of α-Zr, Metallurgical Transactions 4 (1973) 1201-1206.

[68] V. Černý, J. Čadek, Creep, the Portevin-Le Chatelier effect and dynamic strain aging in 18Cr-12Ni and 17Cr-3Ni-2.5Mo stainless steels, Materials Science and Engineering 66 (1984) 89-96.

[69] H. Sun Ig, Influence of dynamic strain aging on the apparent activation energy for creep, Materials Science and Engineering 64 (1984) L19-L21.

[70] T.L. da Silveira, S.N. Monteiro, Jumps in the creep curve of austenitic stainless steels, Metallurgical Transactions A 10 (1979) 1795-1796.

[71] V.K. Sikka, S.A. David, Discontinuous creep deformation in a type 316 stainless steel casting, Metallurgical Transactions A 12 (1981) 883-892.

[72] K. Linga Murty, Transitional creep mechanisms in Al-5Mg at high stresses, Scripta Metallurgica 7 (1973) 899-903.

[73] S. Ig Hong, Influence of dynamic strain aging on the stress exponent and the dislocation substructure for the creep of Al☐Mg alloys, Materials Science and Engineering 82 (1986) 175-185.

[74] M. Valsan, D.H. Sastry, K.B.s. Rao, S.L. Mannan, Effect of strain rate on the high-temperature low-cycle fatigue properties of a nimonic PE-16 superalloy, Metallurgical and Materials Transactions: A 25 (1994) 159-171.

[75] V.S. Srinivasan, R. Sandhya, M. Valsan, K.B.S. Rao, S.L. Mannan, D.H. Sastry, The influence of dynamic strain ageing on stress response and strain-life relationship in low cycle fatigue of 316L(N) stainless steel, Scripta Materialia 37 (1997) 1593-1598.

[76] S.-G. Hong, K.-O. Lee, S.-B. Lee, Dynamic strain aging effect on the fatigue resistance of type 316L stainless steel, International Journal of Fatigue 27 (2005) 1420-1424.

[77] I.S. Choi, S.W. Nam, K.-T. Rie, Mechanism of the fatigue life increment due to dynamic strain ageing during hold time, Journal of Materials Science 20 (1985) 2446-2458.

[78] K.B.S. Rao, H. Schuster, G.R. Halford, Mechanisms of high-temperature fatigue failure in alloy 800H, Metallurgical and Materials Transactions: A 27 (1996) 851-861.

[79] H. Jiang, X. Chen, Z. Fan, J. Dong, H. Jiang, S. Lu, Influence of dynamic strain aging pre-treatment on creep-fatigue behavior in 316L stainless steel, Materials Science and Engineering: A 500 (2009) 98-103.

[80] P. Rodriguez, Dynamic Strain Ageing: Is it really a damage mechanism?, in: B. Raj, K.B.S. Rao, T. Jayakumar, R.K. Dayal (Eds.) Proceeding of International Symposium on Materials Ageing and Life Management, Allied Publishers Limited, Kalpakkam, India, 2000, pp. K1-K14.

[81] L.J. Carroll, W.R. Lloyd, J.A. Simpson, R.N. Wright, The influence of dynamic strain aging on fatigue and creep-fatigue characterization of nickel-base solid solution strengthened alloys, Materials at High Temperatures 27 (2010) 313-323.

[82] K.L. Murty, E.O. Hall, Dynamic Strain-Aging and Neutron Irradiation in Mild Steel in: Irradiation Effects on the Microstructure and Properties of Metals, ASTM STP 611,1976, pp. 53-71.

[83] K.L. Murty, Is neutron radiation exposure always detrimental to metals (steels)?, Nature 308 (1984) 51.

[84] K. Linga Murty, Role and significance of source hardening in radiation embrittlement of iron and ferritic steels, Journal of Nuclear Materials 270 (1999) 115-128.

[85] S.L. Mannan, K.G. Samuel, P. Rodriguez, The Influence of Grain Size on Elevated Temperature Deformation Behaviour of a Type 316 Stainless Steel, in: R.C. Gifkins (Ed.) Strength of Metals and Alloys (ICSMA 6), Pergamon, Melbourne, 1982, pp. 637-642.

[86] K.G. Samuel, S.L. Mannan, P. Rodriguez, Serrated yielding in AISI 316 stainless steel, Acta Metallurgica 36 (1988) 2323-2327.

[87] A.M. Beese, Z. Wang, A.D. Stoica, D. Ma, Absence of dynamic strain aging in an additively manufactured nickel-base superalloy, Nature Communications 9 (2018) 2083.

[88] E.O. Hall, Yield Point Phenomena in Metals and Alloys, Macmillan1970.

[89] R. Tamhankar, J. Plateau, C. Crussard, Étude de la déformation plastique à chaud d'un fer doux et d'une austénite stable au nickel-chrome, Rev. Met. Paris 55 (1958) 383-400.

[90] K.S.B. Rose, S.G. Glover, A study of strain-ageing in austenite, Acta Metallurgica 14 (1966) 1505-1516.

[91] C.F. Jenkins, G.V. Smith, Serrated Plastic Flow in Austenitic Stainless Steel Transactions of the Metallurgical Society of AIME 245 (1969) 2149-2156.

[92] L.H.D. Almeida, I.L. May, S.N. Monteiro, Effects of Carbon and Nitrogen Levels on the Temperture Ranges for Serrated Flow in Austenitic Stainless Steel, in: H.J. McQueen, J.P. Bailon, J.I. Dickson, J.J. Jonas, M.G. Akben (Eds.), Strength of Metals and Alloys (1CSMA 7), Pergamon Press, Oxford, 1985, pp. 337-342.

[93] L.H.D. Almeida, I.L. May, S.N. Monteiro, Athermal And Temperature Dependent Behavior of Serrated Flow In An Austenitic Stainless Steel, Scripta Materialia 19 (1985) 1451-1454.

[94] K.G. Samuel, S.L. Mannan, P. Rodriguez, Serrated Yielding in AISI 316 Stainless Steel, Acta Metallurgica 36 (1988) 2323-2327.

[95] S.-G. Hong, S.-B. Lee, The tensile and low-cycle fatigue behavior of cold worked 316L stainless steel: influence of dynamic strain aging, International Journal of Fatigue 26 (2004) 899-910.

[96] K. Peng, K. Qian, W. Chenb, Effect of dynamic strain aging on high temperature properties of austenitic stainless steel, Materials Science and Engineering A 379 (2004) 372–377.

[97] S.-G. Hong, S.-B. Lee, Mechanism of dynamic strain aging and characterization of its effect on the low-cycle fatigue behavior in type 316L stainless steel, Journal of Nuclear Materials 340 (2005) 307-314.

[98] L.J. Meng, J. Sun, H. Xing, G.W. Pang, Serrated flow behavior in AL6XN austenitic stainless steel, Journal of Nuclear Materials 394 (2009) 34-38.

[99] I. Nikulin, R. Kaibyshev, Deformation behavior and the Portevin-Le Chatelier effect in a modified 18Cr–8Ni stainless steel, Materials Science and Engineering A 528 (2011) 1340–1347.

[100] B.K. Choudhary, Activation energy for serrated flow in type 316L(N) austenitic stainless steel, Materials Science and Engineering: A 603 (2014) 160-168.

[101] J. Cadek, Creep in Metallic Materials, Elsevier Science Publishers, Amsterdam, The Netharlands, 1988.

[102] F.R.N. Nabarro, F. de Villiers, Physics Of Creep And Creep-Resistant Alloys, Taylor & Francis1995.

[103] K.L. Murty, Y. Zho, B. Devarajan, Transitional Creep Mechanisms in Zr-Alloys : Application to Dry Storage of Spent Nuclear Fuel, in: R.S. Mishra, J.C. Earthman, S.V. Raj (Eds.) Creep deformation: fundamentals and applications: Proceedings of TMS Symposium, TMS (The Minerals, Metals & Materials Society), Seattle, WA, 2002, pp. 31-40.

[104] K.L. Murty, S. Gollapudi, K. Ramaswamy, M.D. Mathew, I. Charit, Creep deformation of materials in light water reactors (LWRs), in: K.L. Murty (Ed.), Materials Ageing and Degradation in Light Water Reactors, Woodhead Publishing 2013, pp. 81-148.

[105] K.L. Murty, High Temperature Deformation and Creep of Materials, Course-held-at North Carolina State University (Spring 2017).

[106] E.C.Monkman, N.J.Grant, An empirical relationship between rupture life and minimum creep rate in creep-rupture tests, Proc. Am. Soc. Test. Mater. 56 (1956) 593.

[107] F. Dobeš, K. Milička, The relation between minimum creep rate and time to fracture, Metal Science 10 (1976) 382-384.

[108] M.F. Ashby, B.F. Dyson, Creep damage mechanics and micromechanisms, in: S.R.V.e. al. (Ed.), Advances in Fracture Research, Pergamon Press, Oxford, 1984, pp. 3–30.

[109] S. Latha, M.D. Mathew, P. Parameswaran, K. Bhanu Sankara Rao, S.L. Mannan, Thermal creep properties of alloy D9 stainless steel and 316 stainless steel fuel clad tubes, International Journal of Pressure Vessels and Piping 85 (2008) 866-870.

[110] F.R. Larson, J. Miller, A Time-Temperature Relationship for Rupture and Creep Stresses, Trans. ASME 74 (1952) 765-771.

[111] J. Bird, A. Mukherjee, J. Dorn, Correlation Between High Temperture Creep Behavior and Structure Quantitative Relations between Properties and Microstructure, Israel Univ, 1969.

[112] K. Linga Murty, S. Gollapudi, I. Charit, Newtonian viscous creep in metals, Transactions of the Indian Institute of Metals 63 (2010) 85-91.

[113] F.A. Mohamed, K.L. Murty, J.W. Morris, Harper-dorn creep in al, pb, and sn, Metallurgical Transactions 4 (1973) 935-940.

[114] K.L. Murty, Viscous creep in Pb—9 Sn, Materials Science and Engineering 14 (1974) 169-177.

[115] M.E. Kassner, P. Kumar, W. Blum, Harper–Dorn creep, International Journal of Plasticity 23 (2007) 980-1000.

[116] T.G. Langdon, Grain boundary sliding as a deformation mechanism during creep, The Philosophical Magazine: A Journal of Theoretical Experimental and Applied Physics 22 (1970) 689-700.

[117] T.G. Langdon, A unified approach to grain boundary sliding in creep and superplasticity, Acta Metallurgica et Materialia 42 (1994) 2437-2443.

[118] K.L. Murty, G. Dentel, J. Britt, Effect of temperature on transitions in creep mechanisms in class-A alloys, Materials Science and Engineering: A 410-411 (2005) 28-31.

[119] K.L. Murty, I. Charit, An Introduction to Nuclear Materials : Fundamentals and Applications, Wiley-VCH, Weinheim, 2013.

[120] J. Weertman, Theory of Steady-State Creep Based on Dislocation Climb, Journal of Applied Physics 26 (1955) 1213-1217.

[121] J. Weertman, Steady-State Creep through Dislocation Climb, Journal of Applied Physics 28 (1957) 362-364.

[122] J. Weertman, High temperature creep produced by dislocation motion, in: A.K. Mukherjee, J.C.M. Li (Eds.), Rate Processes in Plastic Deformation of Materials, ASM, Cleveland, Ohio, USA, 1972, pp. 315–336.

[123] S.L. Robinson, O.D. Sherby, Mechanical behavior of polycrystalline tungsten at elevated temperature, Acta Metallurgica 17 (1969) 109-125.

[124] K.L. Murty, Transitions in deformation mechanisms in class alloys -historical perspective & recent applications to microelectronic solders and nuclear core materials, in: J.C. Earthman, F.A. Mohamed (Eds.) Creep and fracture of engineering materials and structures, The Minerals, Metals & Materials Society, Irvine, USA, 1997, pp. 69-78.

[125] M.E. Kassner, Creep Behavior of Particle-Strengthened Alloys, in: M.E. Kassner (Ed.), Fundamentals of Creep in Metals and Alloys, Elsevier, Amsterdam, 2008, pp. 161-181.

[126] H.E. Evans, G. Knowles, Threshold stress for creep in dispersion-strengthened alloys, Metal Science 14 (1980) 262-266.

[127] D.J. Srolovitz, R.A. Petkovic-luton, M.J. Litton, Diffusional relaxation of the dislocation-inclusion repulsion, Philosophical Magazine A 48 (1983) 795-809.

[128] E. Arzt, Creep of dispersion strengthened materials : a critical assessment, Res. Mechanica. 31 (1991) 399-453.

[129] B.A. Wilcox, A.H. Clauer, Creep of Thoriated Nickel above and below 0.5 Tm, AIME Met. Soc. Trans. 236 (1966) 570-580.

[130] R. Lagneborg, B. Bergman, The stress/creep rate behaviour of precipitation-hardened alloys, Metal Science 10 (1976) 20-28.

[131] R.S. Mishra, T.R. Bieler, A.K. Mukherjee, Superplasticity in powder metallurgy aluminum alloys and composites, Acta Metallurgica et Materialia 43 (1995) 877-891.

[132] T. Shrestha, M. Basirat, I. Charit, G.P. Potirniche, K.K. Rink, U. Sahaym, Creep deformation mechanisms in modified 9Cr–1Mo steel, Journal of Nuclear Materials 423 (2012) 110-119.

[133] O.K. Chopra, K. Natesan, Interpretation of high-temperature creep of type 304 stainless steel, Metallurgical Transactions A 8 (1977) 633-638.

[134] F. Abe, Strengthening mechanisms in steel for creep and creep rupture, in: F. Abe, T.-U. Kern, R. Viswanathan (Eds.), Creep-Resistant Steels, Woodhead Publishing2008, pp. 279-304.

[135] M.F. Ashby, Results and consequences of a recalculation of the frank-read and the orowan stress, Acta Metallurgica 14 (1966) 679-681.

[136] E. Arzt, D.S. Wilkinson, Threshold stresses for dislocation climb over hard particles: The effect of an attractive interaction, Acta Metallurgica 34 (1986) 1893-1898.

[137] R.S. Mishra, T.K. Nandy, G.W. Greenwood, The threshold stress for creep controlled by dislocation-particle interaction, Philosophical Magazine A 69 (1994) 1097-1109.

[138] F. Sun, Y.F. Gu, J.B. Yan, Y.X. Xu, Z.H. Zhong, M. Yuyama, Creep deformation and rupture mechanism of an advanced wrought NiFe-based superalloy for 700 °C class A-USC steam turbine rotor application, Journal of Alloys and Compounds 687 (2016) 389-401.

[139] B. Burton, On the mechanism of the inhibition of diffusional creep by second phase particles, Materials Science and Engineering 11 (1973) 337-343.

[140] J.E. Harris, The Inhibition of Diffusion Creep by Precipitates, Metal Science Journal 7 (1973) 1-6.

[141] R. Lagneborg, R. Attermo, Creep of austenitic 20% Cr/35% Ni stainless steels at low stresses, Journal of Materials Science 4 (1969) 195-201.

[142] I.G. Crossland, B.D. Clay, Diffusion creep and its inhibition in a stainless steel, Acta Metallurgica 25 (1977) 929-937.

[143] G. Knowles, The creep strenghth of a 20%Cr-25%Ni-Nb steel containing controlled particle dipersion, Metal Science 11 (1977) 117-122.

[144] H.J. Kestenbach, W. Krause, T.L. da Silveira, Creep of 316 stainless steel under high stresses, Acta Metallurgica 26 (1978) 661-670.

[145] T. Sritharan, H. Jones, The creep of type 304 stainless steel at low stresses, Acta Metallurgica 28 (1980) 1633-1639.

[146] A.C. Roberts, H.E. Evans, Effects of Titanium and Silicon addtions on Creep Behavior of TiN-dispersion-strenghtened 20Cr-25Ni stailess steel, International Conference on Mechanical Behaviour and Nuclear Applications of Stainless Steel at Elevated Temperatures, Metals Society, Varese, Italy, 1981, p. 11.

[147] E. Evangelista, C. Guardamagna, L. Kloc, A. Rosen, S. Spigarelli, The Role of Cold Working in the Creep Deformation of Nb Stabilized Stainless Steel. I. Creep Results and Microstructural Evolution, High Temperature Materials and Processes 14 (1995) 151-161.

[148] D.V.V. Satyanarayana, G. Malakondaiah, D.S. Sarma, Steady state creep behaviour of NiAl hardened austenitic steel, Materials Science and Engineering: A 323 (2002) 119-128.

[149] J.P. Shingledecker, N.D. Evans, Creep-rupture performance of 0.07C–23Cr–45Ni–6W–Ti,Nb austenitic alloy (HR6W) tubes, International Journal of Pressure Vessels and Piping 87 (2010) 345-350.

[150] L.J. Meng, J. Sun, H. Xing, Creep and precipitation behaviors of AL6XN austenitic steel at elevated temperatures, Journal of Nuclear Materials 427 (2012) 116-120.

[151] D.-B. Park, S.-M. Hong, K.-H. Lee, M.-Y. Huh, J.-Y. Suh, S.-C. Lee, W.-S. Jung, High-temperature creep behavior and microstructural evolution of an 18Cr9Ni3CuNbVN austenitic stainless steel, Materials Characterization 93 (2014) 52-61.

[152] P. Ou, L. Li, X.-F. Xie, J. Sun, Steady-State Creep Behavior of Super304H Austenitic Steelat Elevated Temperatures, Acta Metall. Sin. (Engl. Lett.) 28 (2015) 1336–1343.

[153] D.G. Morris, D.R. Harries, Creep and rupture in Type 316 stainless steel at temperatures between 525 and 900°C Part I: Creep rate, Metal Science 12 (1978) 525-531.

[154] B. Russell, R.K. Ham, J.M. Silcock, G. Willoughby, Creep Mechanisms in Niobium-Stabilized Austenitic Steels, Metal Science Journal 2 (1968) 201-209.

[155] M.E. Krug, D.C. Dunand, Modeling the creep threshold stress due to climb of a dislocation in the stress field of a misfitting precipitate, Acta Materialia 59 (2011) 5125-5134.

[156] J.D. Cook, D.R. Harries, A.C. Roberts, Some factors affecting the creep strength of 20%Cr-25%Ni-Nb austenitic steel at 750 °C, Creep Strength in Steels and High Temperature alloys, The Metals Society, London, 1972, p. 91.

[157] T. Yamane, N. Genma, Y. Takahashi, Creep behaviour of a 25wt % Cr-20wt % Ni austenitic stainless steel doped with antimony, Journal of Materials Science 19 (1984) 263-269.

[158] O.A. Ruano, O.D. Sherby, Low stress creep of fine-grained materials at intermediate temperatures: Diffusional creep or grain boundary sliding?, Materials Science and Engineering 56 (1982) 167-175.

3. MATERIAL AND EXPERIMENTAL METHODS

Various experimental tools were employed in pursuing this research work to attain its objectives. In particular, uniaxial tensile testing, creep testing, transmission electron microscopy and electron backscatter diffraction were extensively utilized for characterizing the serrated yielding, creep behavior and the microstructure of the Alloy 709. This chapter provides detailed information about the alloy used in this study, testing procedures pertaining to mechanical testing and sample preparation for microstructural characterization.

3.1. Material

The material investigated in this study is a highly alloyed advanced austenitic stainless steel (referred to as Alloy 709) with chemical composition listed in the Table 3.1. The Alloy 709 was received in the form of a rectangular plate with dimensions of about 330 mm (length) $\times$ 100 mm (width) $\times$ 25.4 mm (thickness). A photograph for the as-received Alloy 709 is shown in Figure 3.1. The as-received material was manufactured by Carpenter Technology and the processing history is as follows: An ingot of the Alloy 709 (400 lb, 200 mm dia. and 600 mm length) was fabricated using vacuum-induction melting (VIM) and electro-slag remelting (ESR) processes. The ingot was then homogenized at 1250 °C for 4 hours in a reducing atmosphere followed by forging process to make a rectangular plate with size of 100×100 mm. The bar was then hot-forged at a temperature of 1100 °C to a final plate thickness of 25 mm followed by water-quenching.
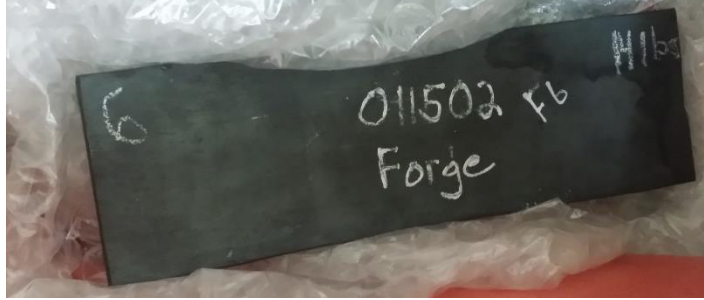
Figure 3.1. A photograph for the as-received Alloy 709 with dimensions of about 330 mm (length) × 100 mm (width) × 25.4 mm (thickness).

Table 3.1. Chemical composition (wt. %) of the Alloy 709 used in this work.

Chemical element	Compositions (wt.%)
C	0.063
Mn	0.88
Si	0.28
P	<0.005
S	<0.001
Cr	19.96
Ni	25
Mo	1.46
N	0.14
Ti	<0.01
Nb	0.23
B	0.0022
Fe	bal.

3.2. Mechanical testing

3.2.1. Tensile tests

Tensile specimens of rectangular pin-loaded type were machined from middle of the as-received plate with dimensions of 20 mm gage length, 4 mm width and 1.15 mm thickness. Figure 3.2 shows the sample geometry and a photograph of a tensile specimen.

Uniaxial tensile tests have been carried out on the Alloy 709 at temperature ranging from 25 – 800 °C and constant cross-head velocities from 0.0002 mm/sec to 0.02 mm/sec corresponding to initial strain rates of $10^{-5} - 10^{-3}$ s^{-1} respectively. Tensile tests were performed using an Instron Universal tester (model No. 5566) equipped with a three-zone furnace. The

70

load and extension were recorded using Bluehill software connected to the Instron machine via a PC. The temperature was measured using a K-type thermocouple wrapped around the gage of the sample and maintained within ±1 K (±1 °C). Before starting the tensile tests, samples were soaked at each test temperature for 30 min to ensure the homogeneity of the temperature over the entire gage length. Once the test was completed, the sample was rapidly cooled to the room temperature by turning the furnace off and using an air fan to preserve the deformation microstructure. The experimental setup is shown in Figure 3.3 depicting the tensile tester components. Tensile tests were repeated (2 to 3 times) to ensure the reproducibility of the test data and the average values are reported with error bars corresponding to the standard devotions around the average values.
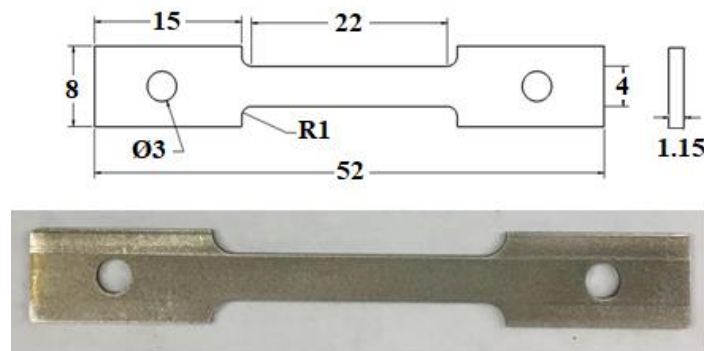
Figure 3.2. The sample geometry (top - all dimensions are in mm). and a photograph (bottom) of the specimen utilized for tensile testing in this work.

During tensile tests, extensometer was not mounted on the gage section of the tensile specimens and thus the crosshead displacement was taken as the specimen extension which was converted to strain by dividing it by the initial gage length of the specimens. The cross head displacement consists of the change in the length of the specimens (due to elastic and plastic deformation) and the change in the length of the parts along the loading train including pull rods, grips and machine frames (due to elastic deformation). Since plastic strain is only considered in this study, the linear elastic portion of stress-strain curves contributed by the

specimen, machine frame, and load–train assembly was subtracted from total elongation by appropriately using the slope of the initial linear portion for the calculation of plastic strain. Thus, the plastic strain was calculated as follows,

$$\varepsilon_{plastic} = \varepsilon_{total} - \varepsilon_{elastic} = \varepsilon_{total} - \frac{\sigma_{\varepsilon_{total}}}{M} \tag{3.1}$$

where ε_{total}, $\varepsilon_{elastic}$, $\varepsilon_{plastic}$, $\sigma_{\varepsilon_{total}}$ and M are total strain, elastic strain, plastic strain, the stress at the total strain ε_{total} and the slope of the linear portion of the stress-strain curves respectively.
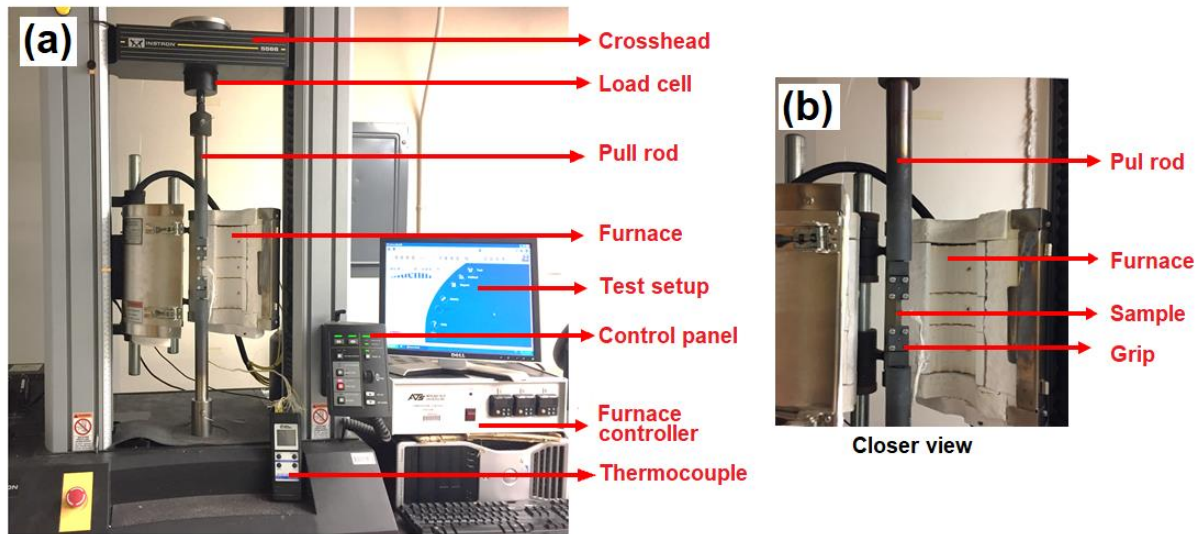
Figure 3.3. (a) Experimental setup showing the Instron tensile tester components. (b) Closer view of the sample attached to the grips.

3.2.2. Creep test

Creep specimens of rectangular pin-loaded type were machined from middle of the as-received plate with dimensions of 25.4 mm gage length, 6.3 mm width and 1.2 mm thickness. Figure 3.4 shows the sample geometry and a photograph of a creep specimen utilized for creep testing.
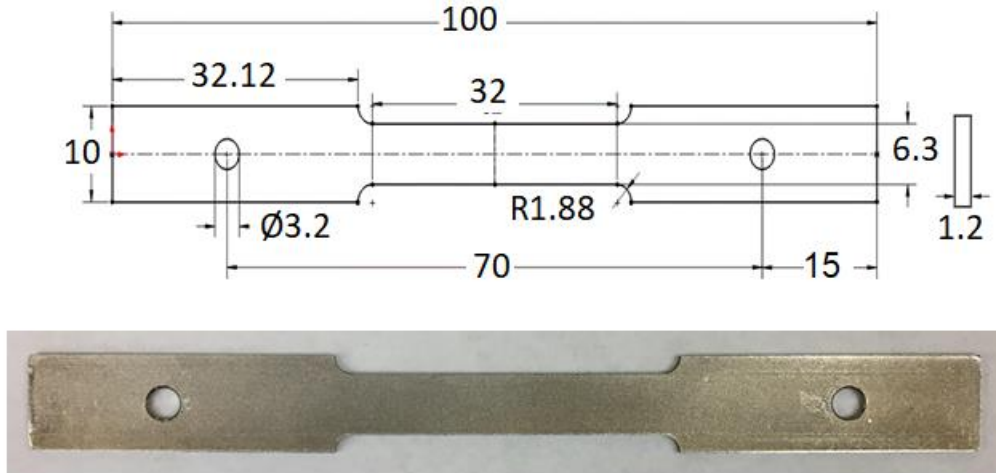
Figure 3.4. The sample geometry (top - all dimensions are in mm). and a photograph (below) of a creep specimen.

Constant load uniaxial creep tests were conducted on the Alloy 709 at temperatures ranging from 700 –800 °C and initial applied stresses of 40 – 275 MPa. Creep tests were performed in air using a constant load lever arm machine (with load ratio 20 :1) employed with a three-zone furnace. The temperature was measured using two K-type thermocouples attached to the gage section of the sample and maintained within ±1 °C during tests. Figure 3.5 shows the experimental set up used for creep tests. Before testing, the specimens were soaked for 30 minutes at the proper temperature without applied load to ensure the homogeneity of the temperature over the entire gage length.

The extension of the sample was measured with an accuracy of 2 µm displacement (or 0.008% strain) using a Linear Differential Variable Capacitor (LVC) transducer attached to a high temperature extensometer. The LVC was connected to a laptop through a LVC control box and a data acquisition box. The Tracerdaq software installed in the laptop was utilized to collect the voltage data generated by the LVC in response to the sample displacement during test. The voltage data (V) was calibrated by attaching the LVC to a micrometer and varying the micrometer from 0 to 0.5 inch with incremental value of 0.001. The calibration curve

comprised of the displacement (D) in inches versus the voltage data (V) yielded the following

$$D = \frac{V + 1.22709}{24.80205} \tag{3.2}$$

At high stresses, the tests conducted were continuously run to final fracture of the specimens. At low stresses, the creep tests were interrupted during the secondary creep stage with several percent of true strains because the creep rates were too low. Selected tests were repeated to ensure the reproducibility of the experimental data. When the test is repeated, average values with error bars corresponding to the standard deviations around the mean are reported.

3.3. Microstructure characterization

3.3.1. Transmission electron microscopy

Transmission electron microscopy (TEM) was utilized to characterize the microstructures of the Alloy 709 in the as-received and deformed conditions to analyze the morphology of dislocations and second phases. TEM was conducted using a JEOL 2000FX TEM at Advanced Instrumentation Facility, NC State University operated at an accelerating voltage of 200 kV. For all bright field TEM micrographs, selected area electron diffraction (SAED) patterns were also obtained and recorded. SAED patterns were utilized to provide more information about the morphology of dislocations and crystal structure of the second phases. Elemental maps for the second phases in the Alloy 709 were obtained using a high angle annular dark field decorator attached to FEI Titan 80-300 scanning-transmission electron microscope at Advanced Instrumentation Facility, NC State University operated at an accelerating voltage of 200 kV.

74
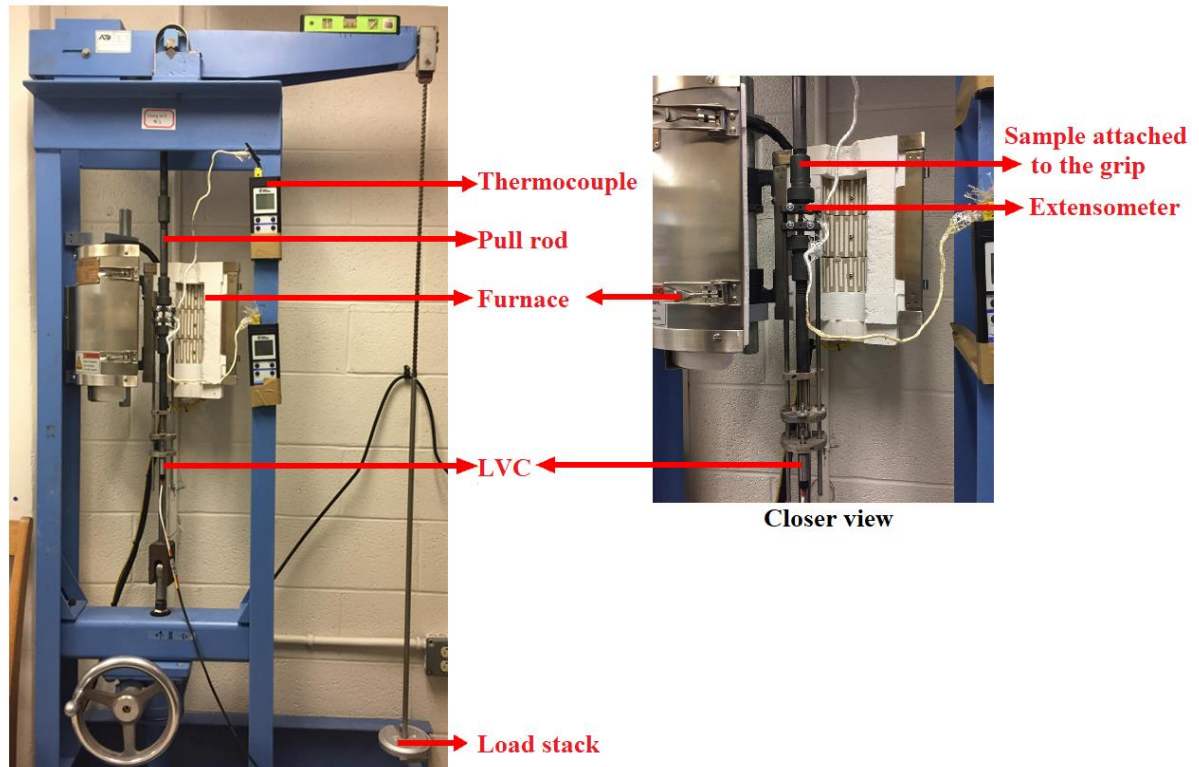
Figure 3.5. Experimental setup showing lever-arm creep tester components. Closer view showing the sample attached to the extensometer and grips.

For synthesizing TEM thin specimens of the Alloy 709, rectangular sections (~ 5 mm × 5 mm) with thickness of about 0.9 – 1.2 mm were first prepared from the as-machined and deformed samples using a Low-Speed Cutting Machine equipped with a diamond blade. The sections were then slowly polished using 320 grit and 400 grit silicon carbide (SiC) papers down to 500 μm followed by using 600 grit and 800 grit papers down to 200 μm. Then, the sections were again polished down to ~ 70 μm thick using Aluminum Oxide Lapping film of 30 – 1 micron grades. The preceding procedures were performed to avoid any artificial dislocations generated in the Alloy 709 from coarse polishing. Small disc specimens with 3 mm diameter were then cut using a mechanical punch for the synthesis of final TEM specimens through twin-jet electro-polishing technique which uses an electrolyte flowing onto the specimen to produce an electron-transparent region within the discs. The detailed information

75

about the twin-jet electropolisher used in this study and the electro-polishing procedures are described in the next paragraph.
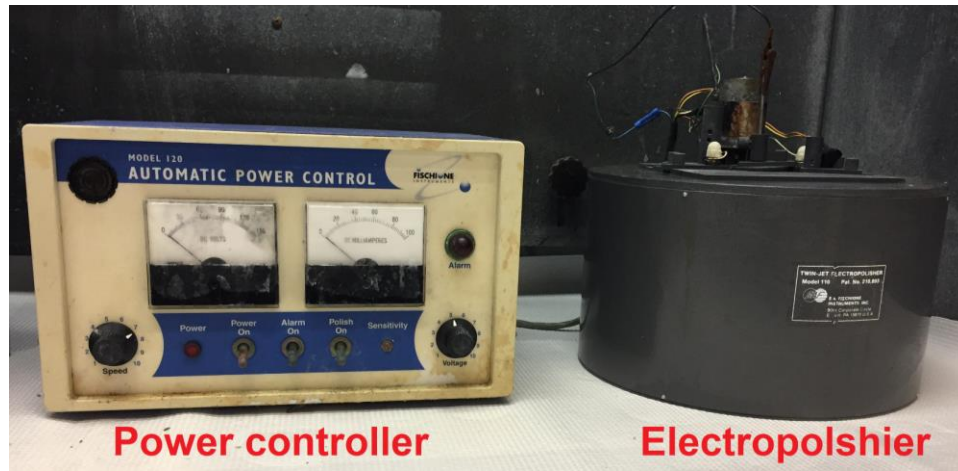
Figure 3.6. The Fischione twin-jet electropolisher employed for making TEM specimens.

A model 110 Fischione automatic twin-jet electropolisher used for electro-polishing discs is shown in Figure 3.6. The electropolisher is connected to a power controller to optimize voltage and the flow speed of the jets. Electropolisher uses two jets to direct electrolyte flow onto the specimen, which simultaneously thins and polishes both sides. It is also equipped with a light alarm system which makes an alarm once a hole is made in the disc as well as stops applying voltage to the electro-polisher. The discs were fixed on the sample holder of the electropolisher which was connected to positive terminal of the power controller while the negative terminal was connected to the stainless steel rods inside the jet nozzles. The electrolyte used for the Alloy 709 was a 10 vol. % perchloric and 90 vol. % methanol solution. The solution was cooled down to ~ 35 °C using liquid nitrogen. By applying a voltage of 30 V and adjusting the speed of the jet flow till the acid touches the disc, the current was obtained to be about ~ 30 mA during electropolishing. Once a hole is created within the disc, the alarm is activated and the process is stopped immediately to avoid any further thinning of the specimens by switching off the power. The holder with specimen was then quickly removed

from the electrolyte and immersed gently into methanol and ethanol in multiple containers for removing any residual acid present in the TEM specimen. The methanol and ethanol were kept at a temperature less than 10 °C using liquid nitrogen. Finally, the TEM specimens were dried in open air before placing inside TEM grid.

3.3.2. Electron backscatter diffraction

Electron backscattered diffraction (EBSD) was used to demonstrate the grain morphology of the as-received and deformed samples of the Alloy 709. The EBSD measurements were carried out on Scanning Electron Microscope (SEM) of FEI Quanta 3D FEG operated at an accelerating voltage of 20 kV at Advanced Instrumentation Facility (AIF) at NC State University where the EBSD detector is connected online through Oxford Aztec software. Iron FCC phase was used to identify the Electron Backscatter Patterns (EBSP) with 9 selected bands. Typical EBSP obtained from the backscatter detector, detected bands and the solved EBSP data to that of Iron FCC are shown in Figure 3.7. In general, less than 2% zero solutions of the EBSP data were determined in all EBSD results. Crystallographic orientation mappings were taken using a step size of 0.6 μm in an area of 150 μm × 150 μm.

The samples for EBSD were sectioned and then mechanically polished using 600–1200 SiC papers followed by 9–1 µm water-based diamond suspension. Subsequently, 50 nm colloidal silica solution as a final polishing was utilized followed by ultrasonic cleaning in acetone. Finally, the sample was dried in open air before placing inside SEM sample holder.
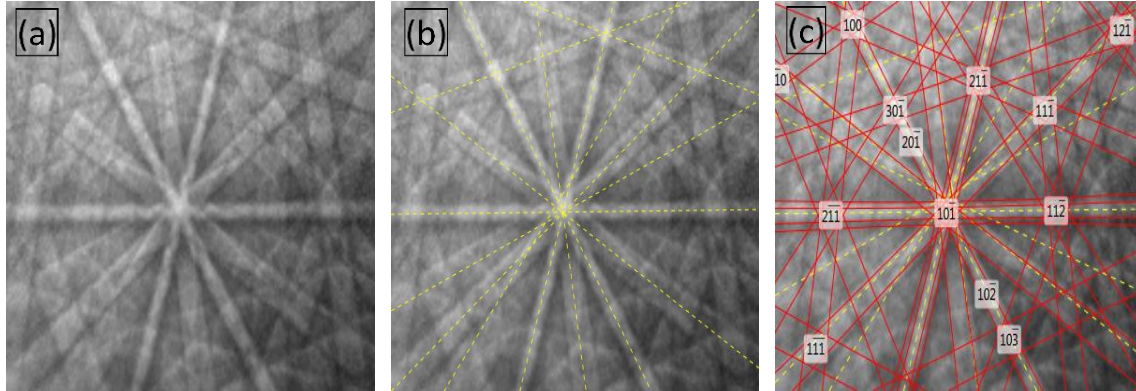
Figure 3.7. (a) Typical EBSP obtained from the backscatter detector for the Alloy 709. (b) Detected bands. (c) The solved EBSP data and indexed to that of iron FCC with zones labelled.

For post-processing EBSD data analysis, HKL Tango commercial software by Oxford Instruments was employed to determine the grain orientations. Standard noise reduction was utilized to reduce the orientation noise originating from zero solutions diffraction data and/or surface contamination, especially for deformed samples. The colors in the EBSD inverse pole images represent the different orientations, e.g., red, green and blue indicate the (0 0 1), (1 0 1) and (1 1 1) planes respectively. The grain boundary distribution was evaluated with an assumption of 2 to 15-degree misorientation angle for low-angle grain boundaries (LAGBs) and above 15-degree for high-angle grain boundaries (HAGBs).

4. SERRATED YIELDING IN AN ADVANCED STAINLESS STEEL Fe-25Ni-20Cr (Wt. %)[1]

Abstract

Understanding serrated yielding behavior resulting from dynamic strain aging (DSA) is essential for design and safety considerations. In this work, uniaxial tensile tests were carried out at temperatures ranging from 298 – 1073 K and strain rates 10^{-5} – 10^{-3} s^{-1} followed by microstructural examination of Fe-25Ni-20Cr (wt. %) austenitic stainless steel (Alloy 709), a candidate structural material for Sodium-cooled Fast Reactors. Serrated yielding was found to occur in this alloy in two temperature regimes; low-temperature serrated flow (LT-SF) from 498 – 648 K and high-temperature serrated flow (HT-SF) from 648 – 973 K (depending on the strain rate) with activation energies of 103 ± 13 kJ/mole and 204 ± 11 kJ/mole respectively. The critical strain for the occurrence of serrations was found to increase with strain rate as an exponential function with exponent (m + β) of 0.78 ± 0.1 and 1.56 ± 0.2 for the LT-SF and HT-SF regimes respectively. Based on the activation energies and m + β values, diffusion of interstitial atoms has been suggested to be responsible for serrated flow in the LT-SF regime while Cr atom migration was inferred to be responsible for DSA in the HT-SF regime. Manifestations of DSA in the Alloy 709 were observed including peaks and/or plateaus in flow stresses along with negative strain rate sensitivity at intermediate temperatures. However, no loss in ductility was observed within DSA regime attributed to the relatively high work hardening rate and strain-hardening exponent. The samples deformed in DSA regime showed planar substructure while equiaxed subgrains formed at higher temperatures. The fraction of low angle grain boundaries after deformation exhibited a valley at intermediate temperatures believed to be another manifestation of the DSA.

---

[1] *This chapter is published in Journal of Materials Science and Engineering: A.*

4.1. Introduction

Advanced materials are needed to withstand higher operating temperatures for longer service life providing more efficient, safe, and reliable structures for next-generation nuclear reactors. Sodium-cooled Fast Reactor (SFR) is one of the leading Gen-IV nuclear reactor concepts that has a two-fold mission - the management of high-level wastes supporting a closed fuel cycle and electricity production that meets the needs for a clean energy source with improved thermal efficiency [1, 2]. Advanced materials developed for SFR should withstand the harsh operating conditions allowing for improved plant efficiency and cost reduction [3]. Alloy 709, a Nb-containing and nitrogen stabilized Fe-25(wt.%)Ni-20Cr advanced austenitic stainless steel, is an excellent candidate material for structural applications in the SFR due to the desired set of mechanical properties found during preliminary investigations relative to conventional stainless steels, SS304 and SS316 [4, 5]. Serrated yielding resulting from the dynamic strain aging (DSA) may have a detrimental effect on mechanical properties such as fatigue life [6], fracture toughness [7], and ductility [8-12] associated with solute-dislocation interactions at these temperatures. Therefore, an investigation into the DSA phenomenon should be carried out comprehensively for design and safety considerations, especially for those materials expected to operate within the temperature range of DSA regime [13, 14].

Serrated flow or jerky flow also known as Portevin-Le Chatelier effect (PLE) is an instability in the stress-strain curves within specific regimes of temperature and strain rate in both interstitial and substitutional solid-solution alloys [15, 16]. The serrations commonly commence after a critical amount of strain (ε_c) which depends on the test temperature (T) and strain rate ($\dot{\varepsilon}$). Numerous physical processes in a crystalline material can cause serrations in the stress-strain curves [16]. However, the most widely accepted mechanism of serrated flow

80

in many alloys including austenitic stainless steels is the dynamic strain aging (DSA) resulting from the interaction between gliding dislocations and mobile solute atoms during the test [12, 16-22]. Various models have been developed during last decades to understand the details of the DSA mechanisms. Initially, Cottrell [23] proposed a model where impurity atoms are assumed to have sufficient mobility to move together with dislocations increasing the stress required to continue the deformation. Dislocations are then unpinned from their clouds and move freely as the rate of deformation continues. Cottrell also suggested that the vacancies produced by plastic deformation are necessary for strain aging to occur. Later on, McCormick [24] and van den Beukel [25] came up with the "arrest model" to solve the considerable discrepancy in the ε_c values calculated from the solute dragging model taking into account the effect of solute concentration on the DSA. In the arrest model, dislocations are considered to move intermittently on their slip planes during plastic deformation (i.e., dislocations being temporarily arrested at obstacles such as forest dislocations, precipitates, and grain boundaries, breaking free and moving forward to the next set of obstacles). Therefore, a segment of dislocation has to wait for some time until the obstacle is overcome possibly with the help of thermal activation. During waiting time at obstacles, solute atoms may diffuse to the core of mobile dislocations and lock them. The repeated locking and unlocking of the mobile dislocations during plastic deformation give rise to serrated stress-strain curves. The vacancies produced by plastic deformation in arrest model are still needed for serrations to occur in substitutional alloys.

The critical strain, ε_c was suggested to be the strain at which the strain rate sensitivity (SRS) becomes negative [26]. In that sense, Kubin and Estrin [27] suggested that the range of existence of DSA occurs before the ε_c where the SRS is decreasing. When the SRS becomes

81

negative, the conditions for the occurrence of the serrations or PLE are satisfied. Thus, the serrations occur within a subdomain of the DSA region [27]. In all models, the variation of the ε_c with T and $\dot{\varepsilon}$ is expressed as [28]

$$\varepsilon_c^{(m+\beta)} = K \, \dot{\varepsilon} \, \exp\left(\frac{Q}{kT}\right) \tag{4.1}$$

where m and β are exponents in the relations for the variations of vacancy concentration C_υ (i.e., $C_\upsilon \propto \varepsilon_c^{\ m}$) and mobile dislocation density ρ_m (i.e., $\rho_m \propto \varepsilon_c^{\ \beta}$) respectively. K is a constant, k the Boltzmann constant and Q the activation energy associated with the serrated flow. The Q-values, which can be deduced by various methods suggested in the literature, have been extensively used to evaluate the mechanisms responsible for the serrations [29]. In addition to the serrated flow or PLE, other manifestations of the DSA include peaks and/or plateaus of the flow stresses and work hardening rate, decreased or negative strain rate sensitivity and minima in ductility at intermediate temperatures. In this study, serrated flow in the Alloy 709 has been examined. The nature of serrations, possible mechanisms causing the serrated flow, the influence of serrated flow on tensile properties, links between microstructure and the DSA in the Alloy 709 are presented and discussed.

4.2. Experimental methods

4.2.1. Material and Mechanical testing

The Alloy 709 used in this study was received in the form of a hot forged (at 1373 K) plate of 25 mm thick fabricated by Carpenter Technology. The chemical composition of the alloy is given in Table 4.1. Rectangular pin-loaded tensile test specimens of 20 mm gage length, 4 mm width and 1.15 mm thickness were machined from the as-received plate (Figure 4.1a). Tensile tests were performed at a constant cross-head velocity using an Instron Universal

tester (model No. 5566) equipped with a three-zone furnace. Experimental setup employed in this study is shown in Figure 4.1b.

Table 4.1. Chemical composition (wt. %) of the Alloy 709 used in this study.

Chemical element	Compositions (wt.%)
C	0.063
Mn	0.88
Si	0.28
P	<0.005
S	<0.001
Cr	19.96
Ni	25
Mo	1.46
N	0.14
Ti	<0.01
Nb	0.23
B	0.0022
Fe	bal.
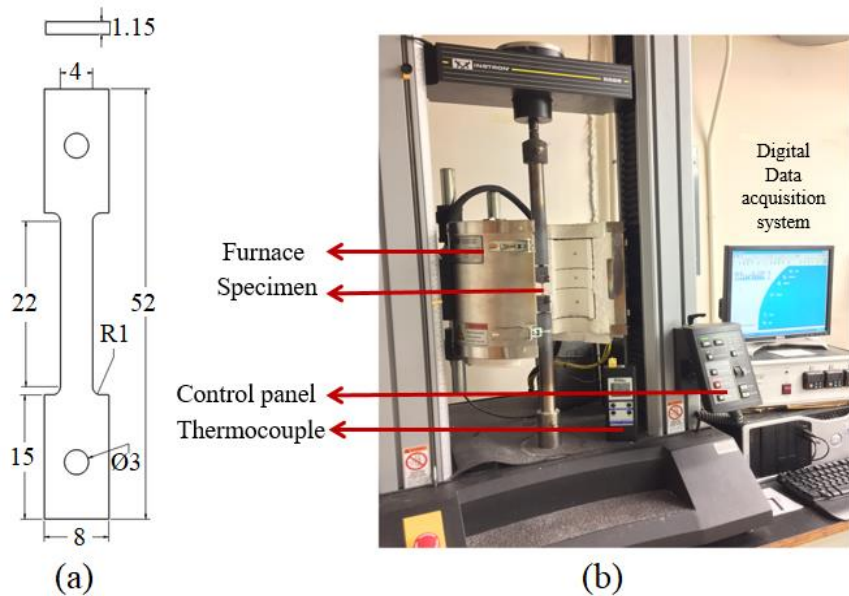
Figure 4.1. (a) Tensile test specimen geometry (dimensions are in mm). (b) Experimental setup.

The extension during the test was recorded using the LVDT installed in the Instron machine that was converted to engineering strain. For the calculation of the plastic strain of the sample, the elastic strain of the stress-strain curve contributed by sample, machine frame and the parts along the loading train was subtracted from total strain at each stress level. The temperature was measured using a K-type thermocouple wrapped around the gage of the sample and maintained within ±1 K (±1 °C). Tensile tests were performed at a wide range of temperatures varying from 298 K to 1073 K (25 °C to 800 °C) and initial strain rates ranging from 10^{-3} s^{-1} to 10^{-5} s^{-1}. Before starting the tensile tests, samples were soaked at each test temperature for 30 min to ensure the homogeneity of the temperature over the entire gage length. The critical strain, ε_c for the onset of serrations in the stress-strain curve was evaluated as the minimum true plastic strain at which a detectable stress jump/drop occurs. Tensile tests were repeated (2 to 3 times) to ensure the reproducibility of the tensile test data and the average values are reported with standard deviations of <5%.

4.2.2. Microstructure characterization

The microstructures of the as-received and deformed samples were characterized using electron backscattered diffraction (EBSD) technique and transmission electron microscopy (TEM). The samples for EBSD were mechanically polished using 600 – 1200 grit size SiC papers followed by 9 – 1 µm water-based diamond suspension. Subsequently, 50 nm colloidal silica solution as a final polishing followed by ultrasonic cleaning in acetone were implemented. The EBSD was carried out on FEI Quanta 3D FEG operated at an accelerating voltage of 20 kV at Advanced Instrumentation Facility (AIF) at NC State University. For each sample, data were acquired with an area of approximately 150×150 µm^2 and a step size of 0.6 µm.

84

The TEM imaging of the as-received and deformed samples was performed using a JEOL 2000FX S/TEM operated at an accelerating voltage of 200 kV at AIF. TEM samples were mechanically ground down to 100 µm thickness using SiC papers of 600 to 1200 grit followed by twin-jet electropolishing using a Fischione twin-jet electropolisher in 10 vol. % perchloric and 90 vol. % methanol solution at ~ 233 K (-40 °C) at a voltage of 30 V.

4.3. Results

4.3.1. Characteristics of serrations

Typical engineering stress-engineering strain curves at a strain rate of 1×10^{-3} s^{-1} at different temperatures is shown in Figure 4.2. At all examined strain rates, the Alloy 709 exhibited serrations in stress-strain curves at intermediate temperatures. Segments of engineering stress vs engineering strain curves at a strain rate of 10^{-3} s^{-1} for different temperatures are shown in Figure 4.3 displaying different types of serrations.
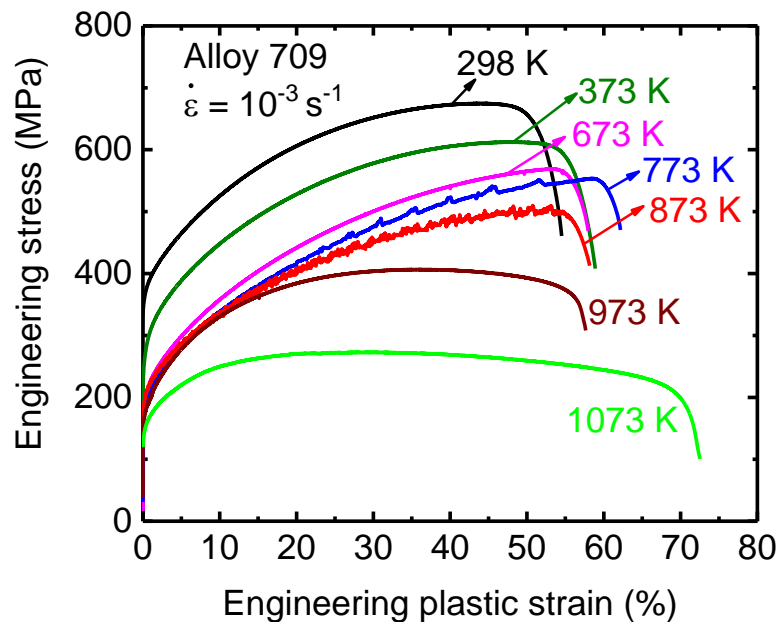
Figure 4.2 Typical engineering stress-engineering strain curves at a strain rate of 1×10^{-3} s^{-1} exhibiting serrated flow at intermediate temperatures in the Alloy 709.
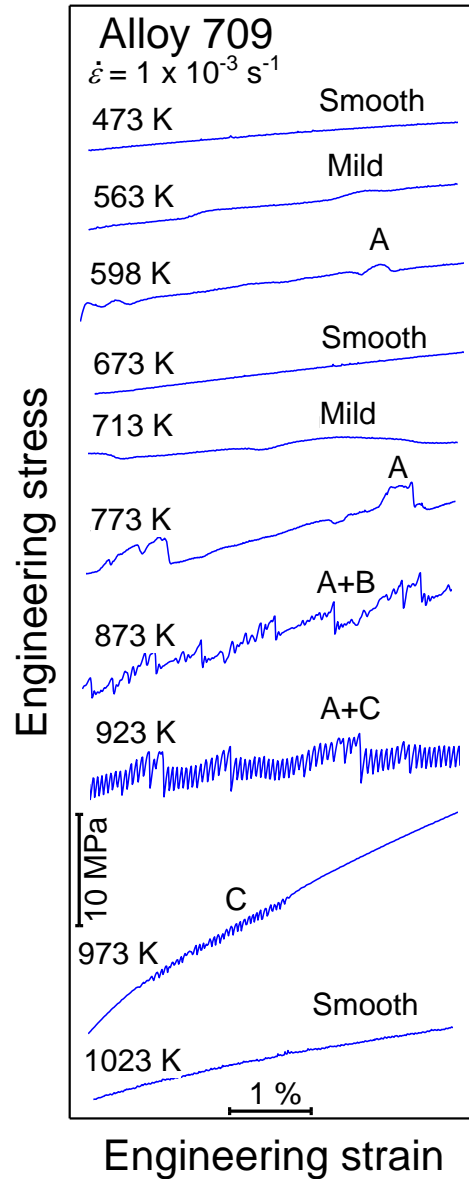
Figure 4.3. The segments of engineering stress – engineering strain curves at the initial strain rate of 10^{-3} s^{-1} and different temperatures exhibiting different types of serrations in the Alloy 709.

The serrations are labelled based on the accepted classification of serration types reported in the literature [15, 16]. At a strain rate of 10^{-3} s^{-1}, the stress-strain curves exhibited smooth flow over temperatures ranging from 298 – 523 K (25 – 250 °C). Mild serrations (i.e., irregularities in the stress-strain curves appeared at relatively high strains) occurred at 548 – 563 K (275 – 290 °C) and then changed over to type A serrations over temperature range 573

– 648 K (300 – 375 °C) before the reappearance of the smooth flow at 673 – 693 K (400 – 420 °C). With further increase in temperature, the mild serrations reoccurred at 713 K (440 °C) followed by distinct type A serrations at 546 – 773 K (455 – 500 °C). The serrations of the mixed type A+B and A+C were found at temperatures 798 – 873 K (525 – 600 °C) and 923 K (650 °C) respectively. In mixed type serrations, the curve usually starts with pure type A or B and then interference between different types occurs at higher strain values. The pure type C serrations were observed at 948 – 973 K (675 – 700°C). The stress-strain curves then continued to flow smoothly from 998 K (725 °C) to 1073 K (800 °C), the highest test temperature used in the present work. The temperature range in which specific type of serrations appears was dependent on strain rates. Table 4.2 provides a summary of serrations observed as a function of temperature and strain rate. At a given strain rate, it is noted from Table 4.2 that two distinct temperature regimes of serrated flow exist, *i.e.,* low-temperature serrated flow (LT-SF) and high-temperature serrated flow (HT-SF) separated by a retardation bay temperature regime where serrations are mild or absent depending on the strain rate.

For all stress-strain curves exhibiting serrations in the Alloy 709, the serrated flow commenced after a finite amount of plastic strain (ε_c) that was obtained from the true stress-true strain curves as the minimum plastic strain at which a detectable stress jump/drop occurred. Figure 4.4 shows typical segments of true stress versus true plastic strain curves up to the point of ultimate tensile stress (UTS). The inset in Figure 4 clearly shows the presence of the critical strain in the Alloy 709. Once the serrated flow commenced at ε_c, the serrations were observed to continue throughout the test until fracture occurred. For only pure type C, the serrations were found to occur within a certain plastic strain range as seen in Figure 4.3 for the curve at 973 K (700 °C).

Table 4.2. A summary of the various type of serrations observed at different temperatures and strain rates in the Alloy 709.

Temperature, K (°C)	Strain rate, (s⁻¹)		
	10^{-3}	10^{-4}	10^{-5}
298 (25)	Smooth	Smooth	Smooth
373 (100)	Smooth	Smooth	Smooth
473 (200)	Smooth	Smooth	Mild
523 (250)	Smooth	A	A
563 (290)	Mild	A	A+B
623 (350)	A	Mild	Mild
673 (400)	Smooth	A	A
728 (455)	A	A	A+B
773 (500)	A	A+B	A+B
823 (550)	A+B	A+B	A+C
873 (600)	A+B	A+C	Smooth
923 (650)	A+C	Smooth	Smooth
973 (700)	C	Smooth	Smooth
1023 (750)	Smooth	Smooth	Smooth
1073 (800)	Smooth	Smooth	Smooth
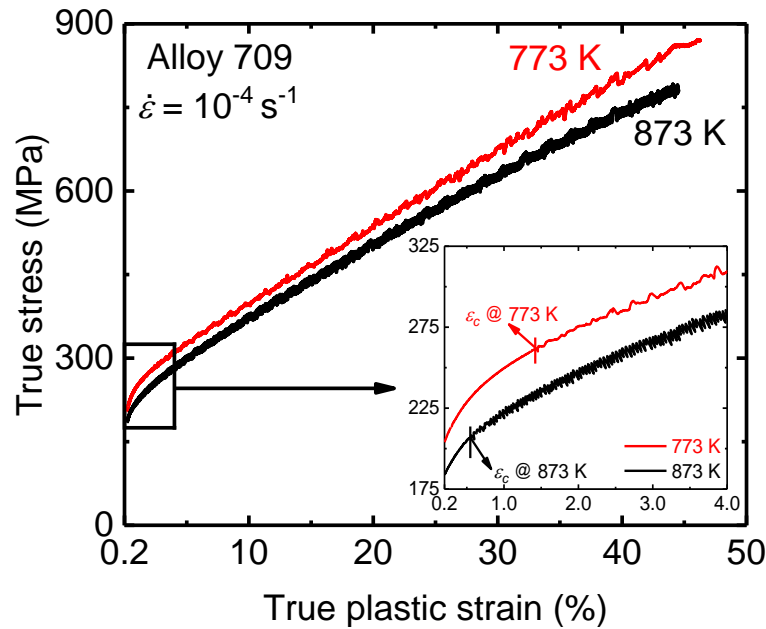
Figure 4.4. Typical true stress versus true plastic strain curves (up to the necking point of ultimate tensile stress) at a strain rate of 10^{-4} s⁻¹ and different temperatures showing the critical strain evaluation in the Alloy 709.

4.3.2. Activation energy for serrated flow

In this study, four methods [29, 30] are employed to evaluate the activation energy for

the serrated flow in the Alloy 709. Figure 4.5 shows the serration map in the $\dot{\varepsilon}$ versus $1000/T$

space where the LT-SF, retardation bay and HT-SF regimes are noted to confine between the

lines (a) and (b), lines (b) and (c) and lines (c) and (d) respectively. Using Figure 4.5, the

activation energy (Q) is obtained from the slopes of the boundaries delineating serrated and

smooth flow (Method-I). Q-values for the onset of type A serrations and the termination of

serrations in LT-SF are obtained from the slopes of the lines (a) and (b) as 113 ± 8 kJ/mole and

195 ± 36 kJ/mole respectively. In HT-SF, the activation energy for the onset of type A

serrations is found from the line (c) as 198 ± 18 kJ/mole while an activation energy of $269 \pm$

13 kJ/mole are evaluated for the termination of serrations in HT-SF using the line (d).
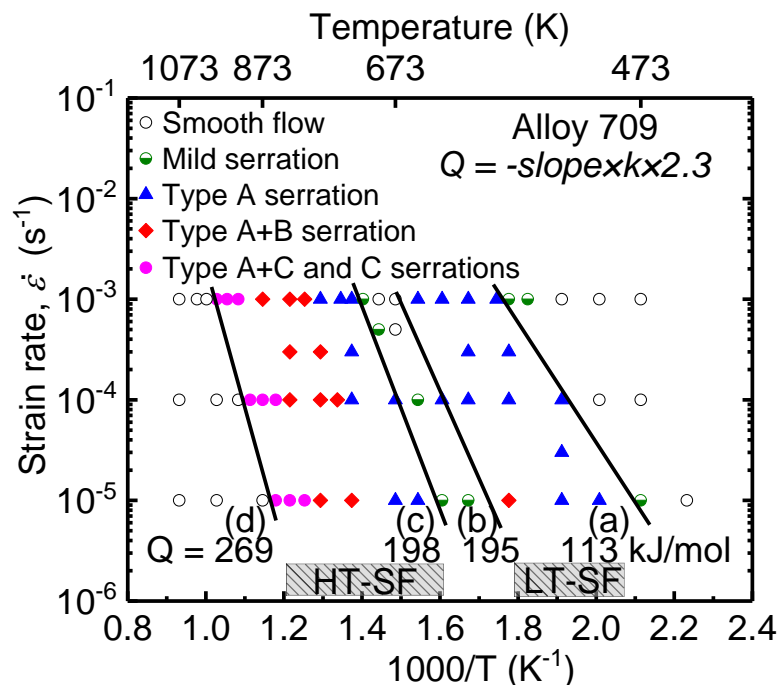
Figure 4.5. Semi-log plot of strain rate versus $1000/T$ showing the serration map in the Alloy 709 and the determination of the activation energy (Q) for the onset and termination of serrated flow in both low-temperature (LT-SF) and high-temperature (HT-SF) serrated flow regimes.

The variation of the critical strain, ε_c with strain rate, $\dot{\varepsilon}$ on a log-log scale at different

temperatures is shown in Figure 4.6a and at a given temperature, ε_c decreases with a decrease

in strain rate with a slope corresponding to the values of the exponent $m+\beta$ in Equation (4.1)

which are found to be 0.78±0.1 and 1.56±0.2 for the LT-SF and HT-SF regimes respectively.

Figure 4.6b shows the variation of the ε_c with the temperature as an Arrhenius plot at different strain rates and we note the normal behavior of critical strain, i.e., a decrease in ε_c with an increase in temperature for both LT-SF and HT-SF regimes. Using these $m+\beta$ values and following Equation (4.1), Q-values for different serrated flow regimes are determined to be 100±18 kJ/mole and 190±14 kJ/mole respectively in the LT-SF and HT-SF regimes (i.e. critical strain method, Method-II). An intercept method (i.e., Method-III) was also employed to determine Q-values for the serrated flow in the Alloy 709 wherein the intercept values of the strain rate for different critical strain values obtained from Figure 4.6a are plotted against 1000/T on a semi-log scale as shown in Figure 4.6c. Average Q-values obtained from the slopes in Figure 4.6c and for critical strain levels of 0.01, 0.02 and 0.03, are noted to be 89 ± 6 kJ/mole and 219 ± 3 kJ/mole in the LT-SF and HT-SF regimes respectively.

Table 4.3. A summary of Q-values for different regimes evaluated by different methods.

Method for the evaluation	Q-value (kJ/mole)	
	LT-SF	HT-SF
Arrhenius plot (Method-I)	113 ± 18	198 ± 13
Critical strain (Method-II)	100 ± 18	190 ± 14
Intercept (Method-III)	89 ± 6	219 ± 3
McCormick (Method-IV)	111	210 ± 12
Average of four methods	103 ± 13	204 ± 11

Following the arrest model for the DSA developed by McCormick [24] relating the concentration of solute atoms, the ε_c can be formulated as,

$$\varepsilon_c^{m+\beta} = \left(\frac{C_1}{\propto C_\circ} \right)^{3/2} \frac{\dot{\varepsilon}\, k\, T\, b \exp(Q/kT)}{3 L N_d K_v U_m D_\circ} \tag{4.2}$$

where C_1 is the solute concentration at the dislocations required to lock them, C_o is the original solute concentration in the alloy, b the Burgers vector, L the average distance between

arresting obstacles, U_m solute-dislocation binding energy, D_o the diffusion frequency factor. α, N_d and K_v are constants. Q-value can be determined from the slope of the semi-log plot of the $\varepsilon_c^{(m+\beta)/T}$ versus $1/T$ (Method-IV) and Figure 4.6d shows the plot of $\varepsilon_c^{(m+\beta)}/T$ versus $1000/T$ using the individual values of $m+\beta$ obtained from Figure 4.6a for each temperature at different strain rates. The average activation energy using this method is found to be 210 ± 12 kJ/mole for the HT-SF. In the LT-SF, Q-value of 111 kJ/mole is obtained at a strain rate of 10^{-4} s^{-1} and not enough data are available for the other strain rates. Table 4.3 summarizes the values of the activation energies for the LT-SF and HT-SF regimes obtained using the above different methods.

4.3.3. The influence of serrations on tensile properties

The temperature and strain rate variations of the elastic modulus (E) compensated 0.2% yields stress (YS) and ultimate tensile stress (UTS) are shown in Figure 4.7a where the values of E as a function of temperature for the Alloy 709 were obtained from Ref. [31] for Fe-20Cr-25Ni/Nb-stabilized steel. At all strain rates, a slight decrease in the normalized UTS from 298 K to 473 K (25 °C to 200 °C) is followed by a peak at intermediate temperatures, depending on the strain rate, before rapid decrease at higher temperatures. The variation of the normalized YS exhibited a decrease with increasing temperature from 298 K to 473 K (25 °C to 200 °C) followed by a plateau or slight peak depending on the strain rate at intermediate temperatures. With further increase in the temperature, a moderate decrease in the flow stress is observed at all strain rates. Note that the peaks and plateaus observed in the YS and UTS coincided with the occurrence of serrated flow. Moreover, the increase in the YS at intermediate temperatures becomes more pronounced at lower strain rates in serrated flow regime as shown in the small dashed-box in Figure 4.7a.
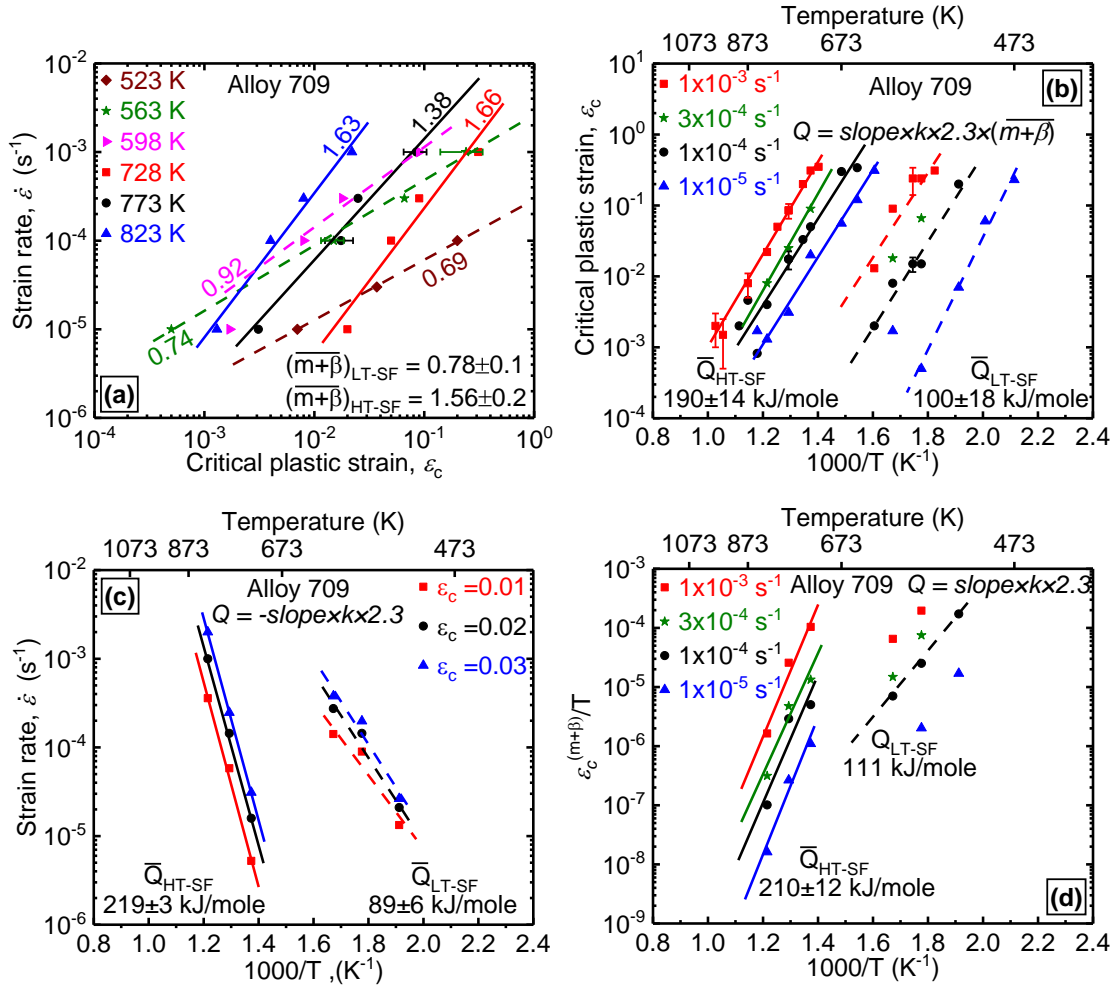
Figure 4.6. (a) The variation of the critical strain, ε_c with strain rate versus εc at different temperatures for obtaining the m+β exponents at different temperatures. (b), (c) and (d) are the variation of ε_c with temperature at various strain rates, the variation of strain rate with temperature at different ε_c and $\varepsilon_c^{(m+\beta)/T}$ versus $1000/T$ at different strain rates for evaluating the Q-values of the serrated flow in the LT-SF and the HT-SF regimes using Methods-II, III and IV respectively. (see text for details).

The variations of the ductility (i.e. elongation to fracture, ε_f) and the uniform elongation, ε_u (defined as the elongation up to the necking point, i.e., UTS) at different strain rates as a function of temperature for the Alloy 709 are shown in Figure 4.7b. No significant variations are noted in the ε_f and ε_u with temperature up to around 673 K (400 °C) at all strain rates while with further increase in temperature, ε_f and ε_u exhibited pronounced peaks at all strain rates followed by a valley in ε_f and a decrease in ε_u at higher temperatures. The valleys in the ε_f are noted to depend on the strain rate.
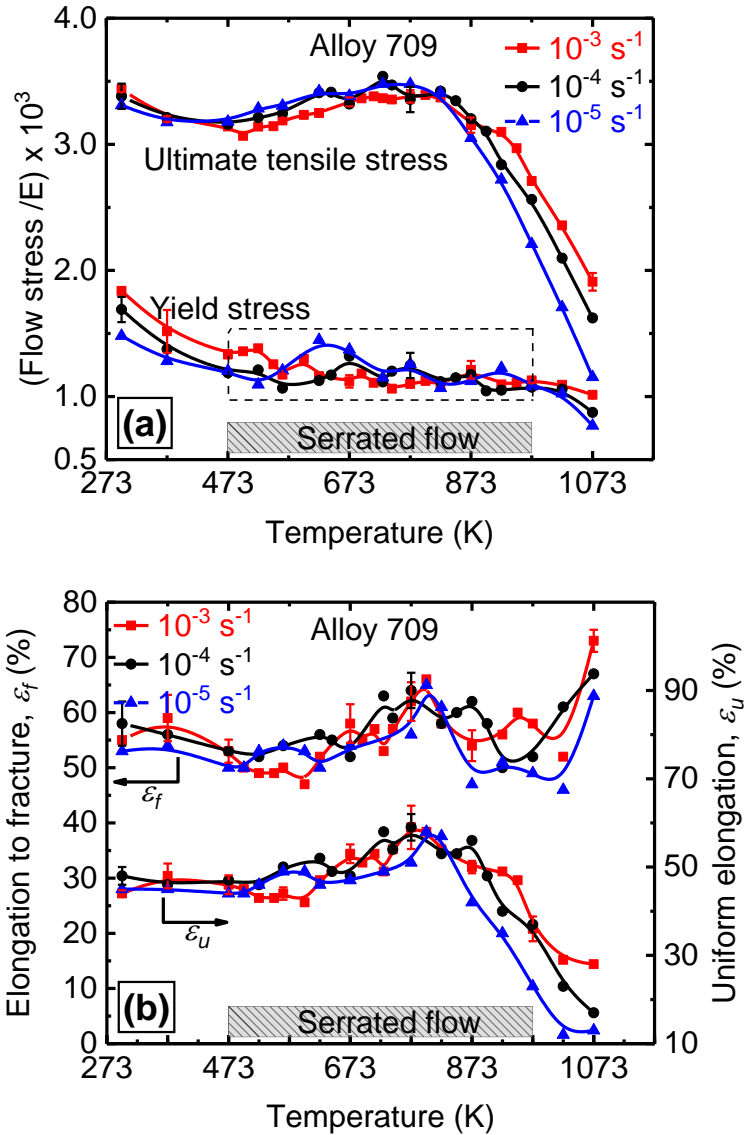
Figure 4.7. (a) Temperature variations of the yield (YS) and ultimate tensile (UTS) stresses and (b) Temperature variations of the elongation to fracture (ε_f) and the uniform elongation (ε_u) at different strain rates for Alloy 709.

4.3.4. Microstructures

Figure 4.8a shows the orientation imaging micrograph (OIM) of the Alloy 709 in as-received condition. The color associated with each grain in the OIM micrograph represents a crystallographic direction perpendicular to the plane of the paper and the associated crystallographic direction for each color can be gleaned from the inverse pole figure map included in the figure. The microstructure of the Alloy 709 in the as-received condition exhibits

nearly equiaxed austenitic grains with annealing twins and some elongated grains that may have formed during forging process. Also, it was found that the fraction of HAGBs exceeds 98% in as-received condition. The corresponding TEM image taken at two beam condition of the alloy in as-received condition is shown in Figure 4.8b exhibiting dislocation related substructures and pre-existing fine precipitates ($<$ ~100 nm). Figure 4.8c shows a bright field TEM image taken at $[1\bar{1}2]$ zone axis. A typical energy dispersive spectroscopy (EDS) spectrum for the pre-existing precipitates is shown in the inset of Figure 4.8c exhibiting niobium rich particles. The SAED pattern taken around the precipitate area encircled in Figure 4.8c is shown in Figure 4.8d, and the precipitates are noted to have a lattice parameter slightly larger than that of austenite matrix. These pre-existing fine precipitates are consistent with the typical reflection for MX-type precipitates reported in Nb-containing austenitic stainless steels where X stands for carbon or nitrogen and M refers to the stabilizing carbide/nitride formers such as Nb [32, 33].

Figure 4.9a to Figure 4.9d are bright field TEM micrographs of deformed samples strained to failure at a strain rate of 10^{-3} s^{-1} and temperatures of 373 K (100 °C), 563 K (290 °C), 728 K (455 °C) and 1073 K (800 °C) respectively. At low temperatures (Figure 4.9a) where smooth stress-strain curves were obtained, the dislocation substructure resulting from testing at 373 K (100 °C) exhibited heterogeneous distribution with a region of high dislocation-dislocation interactions.
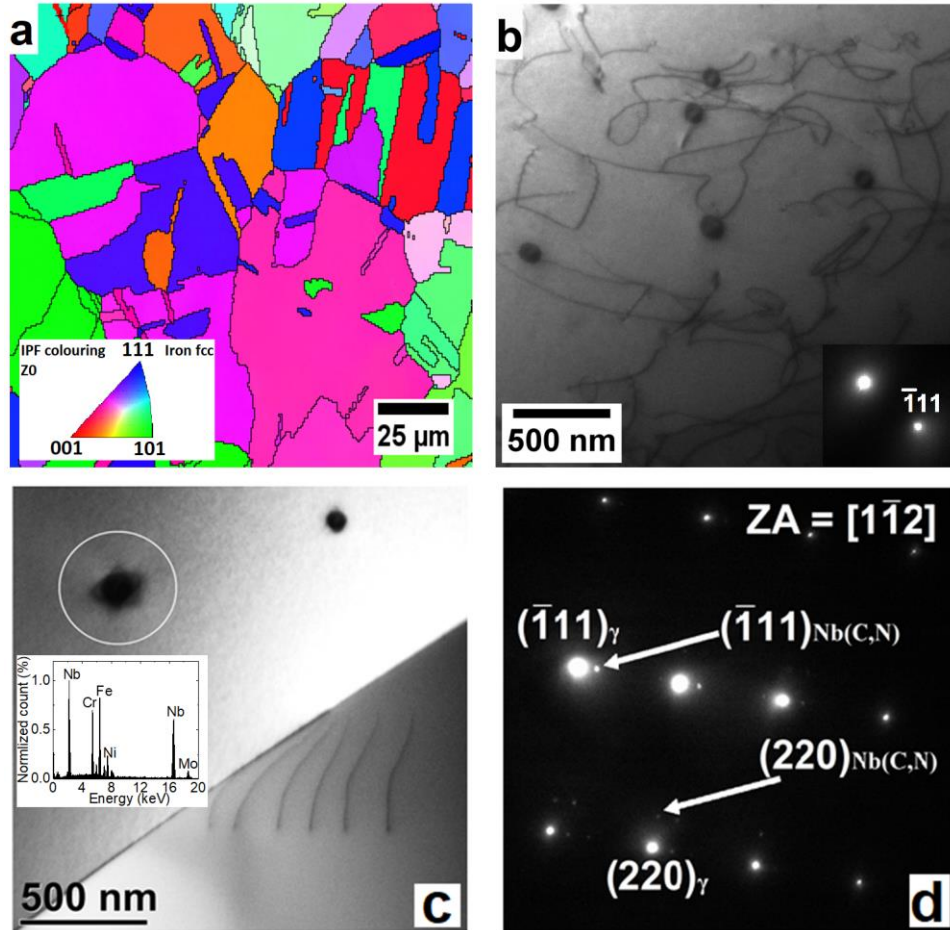
Figure 4.8. Microstructure of the Alloy 709 in as-received condition. (a) Orientation imaging micrograph with inverse pole figure map (shown in the inset) and HAGBs are shown as black lines. (b) Bright field TEM image taken at two-beam condition showing dislocation related substructures and pre-existing fine precipitates. (c) Bright field TEM image and inset shows a typical energy dispersive spectroscopy (EDS) spectrum exhibiting niobium rich particles. (d) SAED pattern corresponding to zone axis $[1\bar{1}2\ ]$ acquired from the area encircled in (c) indicating the reflections of the matrix and niobium rich precipitate

At temperatures of 563 K (290 °C) and 728 K (455 °C) corresponding to LT-SF and HT-SF regimes, the microstructures in Figure 4.9b and Figure 4.9c respectively exhibit a high degree of planarity of dislocation glide. At 1073 K (800 °C) where the serrations disappeared from the stress-strain curve, subgrain formation and large precipitates (with an average size larger than 150 nm) were observed as seen in Figure 4.9d. A typical EDS spectrum for the large precipitates is shown in the inset of Figure 4.9d exhibiting chromium rich particles. These precipitates are consistent with $M_{23}C_6$ particles noted in similar steels at high temperatures

where M mainly stands for Cr but other metallic elements like Fe, Mo, and Ni can also partially substitute for Cr [32, 33]. Figure 4.10 is a TEM micrograph of the Alloy 709 deformed to a strain level of 2% at a strain rate of 10^{-3} s^{-1} at 873 K (600 °C). The observed linear dislocation substructure was a manifestation of deformation by planar slip.

Figure 4.11a to Figure 4.11d are the OIMs of the Alloy 709 strained to fracture at a strain rate of 10^{-3} s^{-1} and temperatures of 298 K (25 °C), 623 K (350 °C), 728 K (455 °C) and 1073 K (800 °C) respectively along with associated inverse pole figures. The OIMs of deformed samples are clearly distinguished from that of the as-received (Figure 4.8a) where misorientations were developed within grains due to substructure formation during plastic deformation. This resulted in decreased fraction of HAGBs to a value of less than 15%. The fraction of LAGBs and HAGBs as a function of temperature for the deformed samples at the strain rate of 10^{-3} s^{-1} is shown in Figure 4.12. At all temperatures, the fraction of LAGBs was clearly observed to be higher than that of HAGBs and while they exhibited a valley, the HAGBs showed a peak at intermediate temperatures in DSA regime.

96
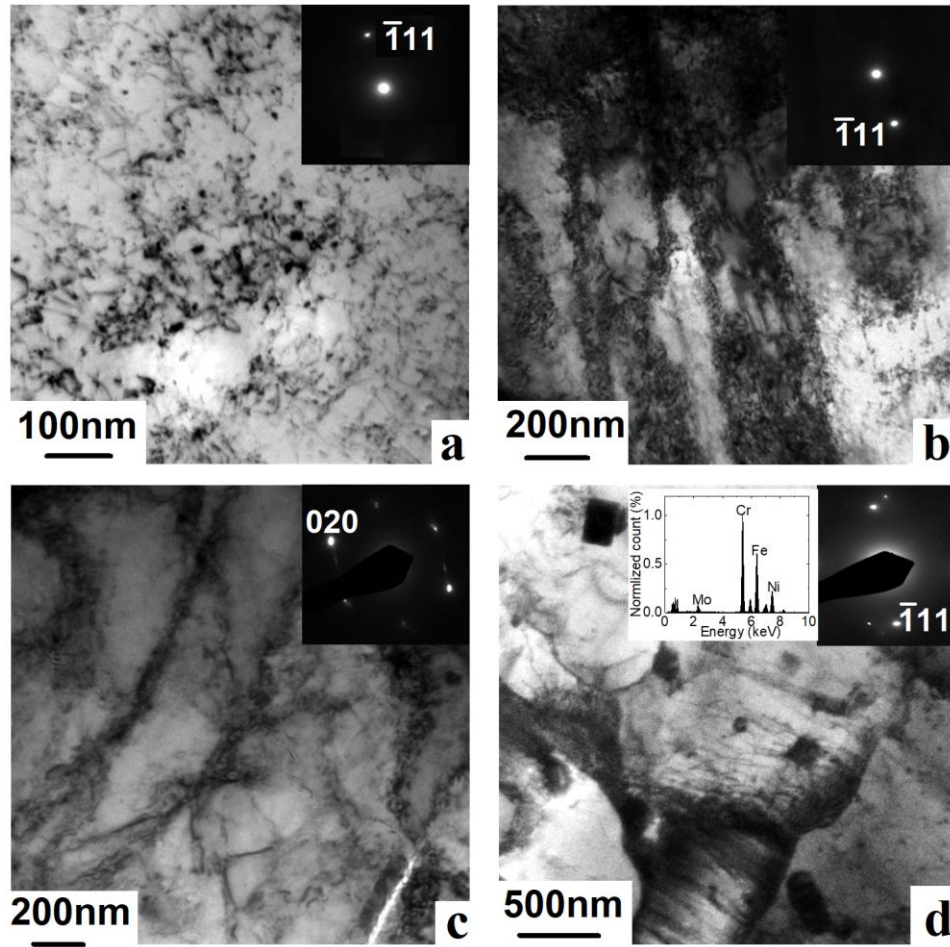
Figure 4.9. Bright field TEM micrographs of the Alloy 709 samples strained to fracture at 10^{-3} s^{-1} and temperatures of (a) 373 K (100 °C) (no serrated flow), (b) 563 K (290 °C) (low temperature serrated flow), (c) 728 K (455 °C) (high temperature serrated flow) and (d) 1073 K (800 °C) (no serrated flow) and typical EDS spectrum exhibiting chromium rich particles is shown in the inset. Corresponding selected area diffraction patterns are included in the inset for all micrographs. Zone-axes are along [1$\overline{1}$2] for (a), (b) and (d) and [101] for (c).
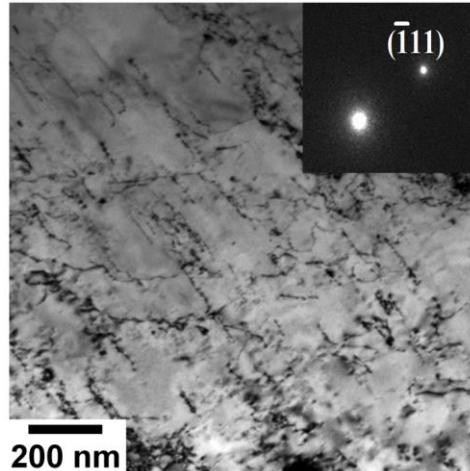
Figure 4.10. A bright field TEM micrograph of the Alloy 709 deformed to a strain level of 2% at a strain rate of 10^{-3} s^{-1} and temperatures of 873 K (600 °C) with corresponding selected area diffraction pattern along $[1\bar{1}2]$ zone-axis shown in the inset.
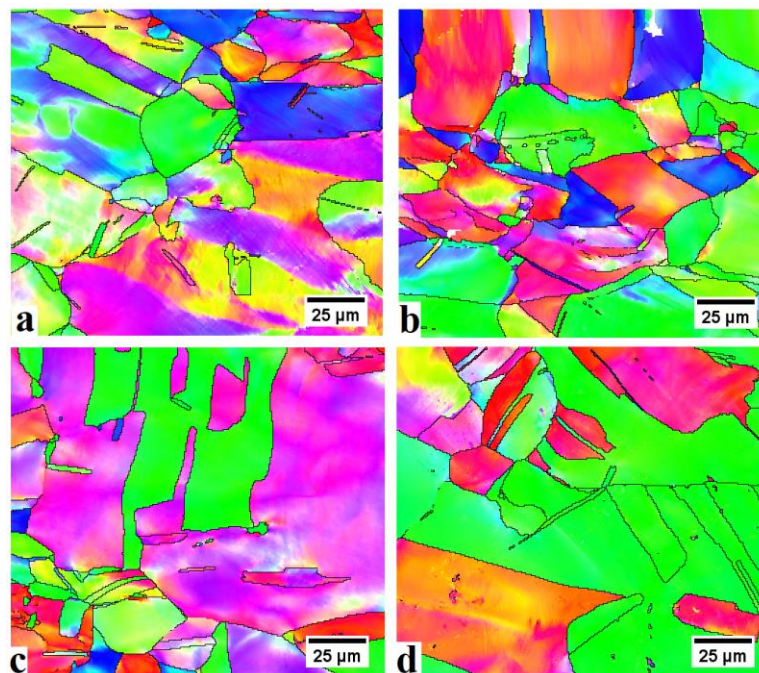
Figure 4.11. Orientation imaging micrographs of the Alloy 709 samples strained to fracture at strain rate of 10^{-3} s^{-1} and temperatures of (a) 298 K (25 °C) (no serrated flow), (b) 623 K (350 °C) (low temperature serrated flow), (c) 728 K (455 °C) (high temperature serrated flow) and (d) 1073 K (800 °C) (no serrated flow). HAGBs are marked with black lines, for details see text.
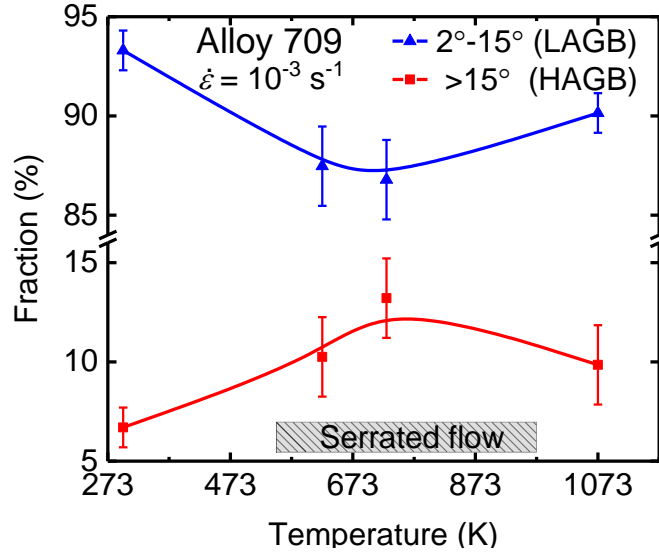
Figure 4.12. The fraction of grain boundaries with misorientation angles of 2–15° (LAGB) and greater than 15° (HAGB) as a function of temperature at which sample deformed to fracture at strain rates of 10^{-3} s^{-1}.

4.4. Discussion

We investigated uniaxial tensile deformation behavior of the Alloy 709 in the temperature range from 298 to 1073 K (25 to 800 °C). The alloy exhibited DSA at intermediate test temperatures with serrated stress-strain curves. The tensile test data at different temperatures and strain-rates were analyzed to find activation energies and critical strain exponent m+β, and both these parameters gave insight into possible rate-controlling mechanism(s) governing the DSA. The variations in YS and UTS of the alloy were consistent with those reported previously in literature on different alloy systems exhibiting DSA. However, the variation in ductility in DSA regime was anomalous and the ductility increased in HT-SF regime contrary to the commonly observed decrease in ductility during serrated flow reported for many material systems in the literature. Additionally, the uniform elongation was also found to increase in HT-SF regime as per the increased work-hardening parameter.

4.4.1. Mechanisms of serrated flow

Despite being highly alloyed, the variation in the serration types at intermediate

temperatures and the existence of two distinct serrated flow regimes (i.e., LT-SF and HT-SF) separated by a retardation bay in the Alloy 709 are consistent with the data reported for different austenitic stainless steels [12, 16, 18, 22]. This alloy exhibited all three types, A, B, and C, of serrations commonly reported. Table 4.4 summarizes the activation energies and ($m+\beta$) exponents for the Alloy 709 and other austenitic steels along with a list of proposed mechanisms for serrated flow [18, 29, 30] .

Table 4.4. Activation energy, ($m+\beta$) exponent, and proposed mechanisms for serrated flow in various austenitic stainless steels [18, 29, 30].

Material	Ti –modified Fe-15Cr-15Ni-		SS 316L(N) SS		SS 304 SS		Alloy 709	
Serrated flow regime	LT-SF	HT-SF	LT-SF	HT-SF	LT-SF	HT-SF	LT-SF	HT-SF
m+β	1.8	1.28	-	1.48	-	-	0.78	1.56
Q-value (kJ/mole)	115	140	115	206	132-136	191–198	103	204
Temp. (°C)	175–450	370–700	250–330	350–750	200–400	400–750	200–400	400–700
Suggested mechanism for DSA	V*	I-V	I	S	I-V	I-V	I	S
Strain rate (s⁻¹)	$10^{-5} - 10^{-2}$		$3\times10^{-5} - 3\times10^{-3}$		$3.5\times10^{-6} - 3.5\times10^{-2}$		$10^{-5} - 10^{-3}$	
Ref.	[29]		[30]		[18]		This study	

V: Vacancy migration. I-V: Interstitial–vacancy pairs diffusion. I: Interstitial diffusion. S: Substitutional diffusion.

The activation energy for the serrated flow is commonly used to infer about the operating mechanism(s) responsible for the occurrence of the serrations. For a given serrated flow regime in the Alloy 709, no significant variations are observed in Q-values determined from different methods so that the average values listed in Table 4.3 are considered in the present study.

The Alloy 709 is highly alloyed stainless steel with relatively large amount of substitutional and interstitial solutes, and both are expected to contribute to the DSA process. Equation (4.1) is extensively used for the determination of activation energy, Q and ($m+\beta$)

exponent of the serrated flow process. As mentioned earlier, per theoretical and experimental estimates, *m* lies between 1 and 1.5 and *β* between 0.5 and 1. Therefore, (*m*+*β*) exponent lies between 1.5 and 2.5 where the serrated flow is being controlled by the diffusion of substitutional solute atoms. In the case of interstitial atoms, Equation (4.1) reduces to the following,

$$\varepsilon_c{}^{\beta} = K' \dot{\varepsilon} \exp\left(\frac{Q'}{kT}\right) \tag{4.3}$$

where *Q'* is the activation energy for the serrated flow controlled by interstitial diffusion. As indicated in Table 4.4, the activation energies estimated for the Alloy 709 for LT-SF and HT-SF regimes correspond to the diffusion of interstitials such as carbon/nitrogen and substitutional chromium, respectively. These values are very similar to what have been reported in the literature for different stainless steels. The values of the exponents estimated in LT-SF and HT-SF regimes are as expected. The *m*+*β* slope for the LT-SF regime was 0.78 which lies in the range 0.5 and 1 and it is 1.56 in HT-SF region lying between 1.5 and 2.5.

For the onset of the serrations in LT-SF regime, Venkadesan *et al* [29] have reported a value of 115 kJ/mole in a 15Cr-15Ni Ti-modified austenitic stainless steel using the average of the four methods considered here and suggested the vacancy migration to be the mechanism responsible for the DSA whereas diffusion of interstitials such as carbon has been suggested to be responsible for DSA in type 316(L)N stainless steel [30]. Rose and Glover [34] suggested the C-vacancy pairs as the controlling mechanism for the serrated flow at 473 K (200 °C) in high Ni austenitic steel, Fe-(31–41%) Ni-(0.12–0.18%) C. They determined about 85 kJ/mole for the *Q*-value for the onset of serrations correlating with the vacancy migration in γ-iron (taken as 1/3 of self-diffusion in γ-iron). A higher value of the activation energy (132–136

kJ/mole) was reported by Almeida *et al.* [18] in type 304 stainless steel and C-vacancy or N-vacancy pairs was attributed to the dislocation locking by interstitial diffusion of C or N controlling the migration of the pair. From the above literature survey, it is noted that the values for the activation energy in LT-SF varied between 85 – 136 kJ/mole. In the present investigation, the activation energy of 103 ± 13 kJ/mole for the onset of the serrated flow in the Alloy 709 was found to lie within the values reported for the diffusion of interstitial solutes such as carbon or nitrogen in stainless steels. Thus, the observation of the serrated flow in the low-temperature regime is attributed to the diffusion of interstitial solutes in the Alloy 709. This view is further strengthened by the observation of $(m+\beta)$ of 0.78 ± 0.1 in this regime, as this is in close agreement with typical $(m+\beta)$ values, i.e., between 0.5 and 1 for interstitial controlled mechanism of DSA [16, 24].

In the HT-SF regime, Q-value for the onset of serrations was determined to be 206 kJ/mole in type 316L(N) stainless steel where Cr diffusion has been proposed to be responsible for DSA [30]. The interaction of C-C pairs with Cr was suggested to provide sufficient locking to cause the serrations in the high-temperature regime in type 304 SS [18]. In a 15Cr-15Ni Ti-modified austenitic stainless steel, C (or N) as controlling diffusing species to form pairs with vacancies causing serrations in HT-SF regime was ascribed as a mechanism for DSA to rationalize the relatively low activation energy of 178 kJ/mole (compared to substitutional solute diffusion) obtained in this regime [29]. In the present case, the activation energy for the onset of serrations in HT-SF regime (204 ± 11 kJ/mole) closely matches with that for the diffusivity of the Cr solutes in Fe-20%Cr-25%Ni stainless steel [35] which was measured to be 246 ± 16 kJ/mole over temperatures 550 – 1290 °C using radiotracer techniques. Therefore, the diffusion of substitutional atoms such as Cr is ascribed to be responsible for the serrations

in HT-SF. The higher value of the $(m+\beta)$ of 1.56 ± 0.2 in this regime relative to the low-temperature region also supports the contribution of the substitutional solutes to the DSA mechanism through the strain induced vacancy concentration [36].

The termination of the serrations in the Alloy 709 are of interest where the activation energy for the disappearance of serrations in HT-SF was determined to be 269 kJ/mole. Often, precipitation mechanism is ascribed to be responsible for the disappearance of serrated flow [20, 37] and carbide or nitride precipitates which are found to form usually on the arrested dislocations will lead to depletion of solute for dislocation locking. When the net solute atoms locking the dislocations decrease to a value below a critical concentration, serrated flow disappears [30, 38]. An extensive review has been carried out on the precipitation behavior of alloys similar to the Alloy 709 by Sourmail [32] where chromium carbides are reported to be nucleated and formed in grain interior and at grain boundaries at intermediate temperatures. In this alloy, Cr rich precipitates have been observed at high temperatures where stress-strain shows smooth flow (see Figure 4.9d). Thus, the disappearance of serrations at high temperatures accompanied with the observation of type C serrations may be ascribed to the formation of the chromium-carbide precipitates leading to the loss of solute (Cr) responsible for the serrations in the Alloy 709.

4.4.2. The influence of the serrations on the tensile properties and microstructure

At low temperatures where smooth stress-strain curves are obtained in the Alloy 709, normal dependence of the flow stresses on the temperature and strain rate (i.e., decrease in the flow stresses with a decrease in strain rate and an increase in temperature) are clearly observed in Figure 4.7a. Planar slip and single slip at low strains followed by cross-slip at higher strains have been found as the deformation mechanism in AISI 316L stainless steel deformed at 300

103

K (27 °C) resulting in heterogeneous dislocation substructure [39]. Dislocation motion by glide and cross-slip are thermally activated processes and will be enhanced as temperature increases. Thus, the decrease in the flow stress with a decrease in strain rate and increase in temperature in the Alloy 709 can be ascribed to the effects associated with easy glide followed by cross-slip resulting from the increase in temperature ranging from 298 – 498 K (25 – 225 °C). This view is further supported by the observation of the heterogeneous dislocation microstructure (Figure 4.9a) of the sample deformed at 373 K (100 °C) where stress-strain curves showed smooth flow.
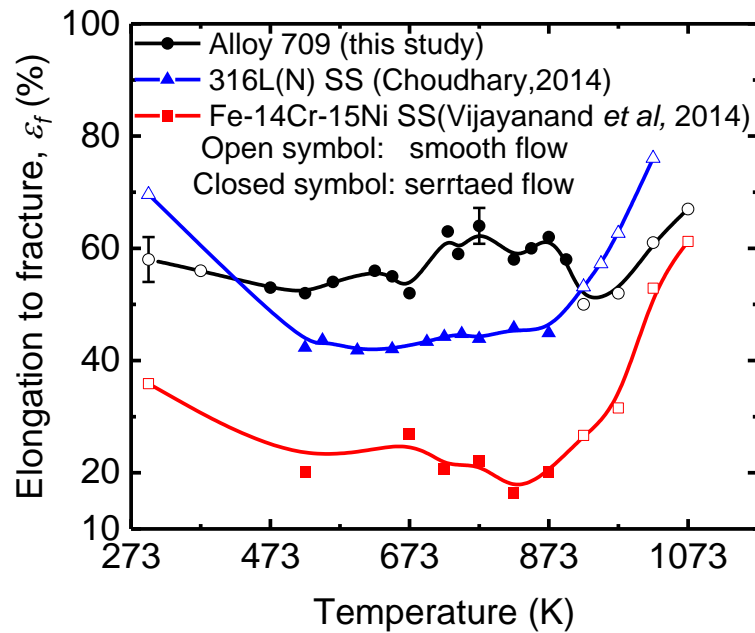
Figure 4.13. Comparison of the ductility data (elongation to fracture) for the Alloy 709 obtained in the current study with those reported for type 316L(N) stainless steel [12] and Fe-14Cr-15Ni [41].

The high degree of dislocation planarity observed in the DSA regime (Figure 4.9b and Figure 4.9c) which has also been reported in AISI 316 SS [40] is ascribed to the restriction of dislocations to the cross-slip and recovery due to DSA at intermediate temperatures. Therefore, the formation of LAGBs will decrease as the deformation by cross-slip or climb are restricted in the DSA regime and was clearly indicated in Figure 4.12 where the fraction of the

LAGB exhibits a decrease at intermediate temperatures in the presence of DSA.

The behavior of the ductility during serrated flow regimes in the Alloy 709 is different from most of the results reported in the literature for the alloys exhibiting DSA phenomena. In general, serrated flow resulting from DSA causes instability in plastic deformation. The localized deformation and the negative strain rate sensitivity are linked with a loss in ductility as reported in various alloys including austenitic stainless steels [11, 30, 42]. Unlike the commonly observed detrimental effect of DSA, a pronounced peak in ductility was observed in the present study in the serrated flow regime relative to room temperature (Figure 4.7b). To illustrate this point further, the variation in total elongation as a function of deformation temperature in the Alloy 709 of this study is compared in Figure 4.13 to those reported in 316L (N) stainless steel [12] and Fe-14Cr-15Ni steel [41]. A decrease from about 70% at room temperature to about 45% at 823 K (550 °C) in the presence of serrated flow is clearly seen in type 316L(N) stainless steel owing to the effect associated with the occurrence of DSA. In materials with very low stacking fault energy, increase in both strength and ductility have been reported [43, 44] and attributed to the deformation twinning. However, no deformation twinning is observed in the deformed samples of the Alloy 709.

In general, the overall ductility of the polycrystalline materials can be understood in terms of the strain rate sensitivity and work-hardening behavior [27]. In this study, the strain rate sensitivity (m) is determined from the equation: $m = \Delta \ln \sigma / \Delta \ln \dot{\varepsilon}$ as the slope of the flow stress at 5% strain versus the strain rate curve on ln-ln scale. Figure 4.14a shows the strain rate sensitivity (m) as a function of temperature where negative strain rate sensitivity is clearly observed in the serrated flow regime due to the enhancement of the localized deformation caused by the DSA. On the other hand, the strain-hardening exponent (n) and work hardening

105

rate (θ) during deformation can also influence the ductility, particularly the uniform elongation since strain-hardening exponent is related to the true uniform strain.
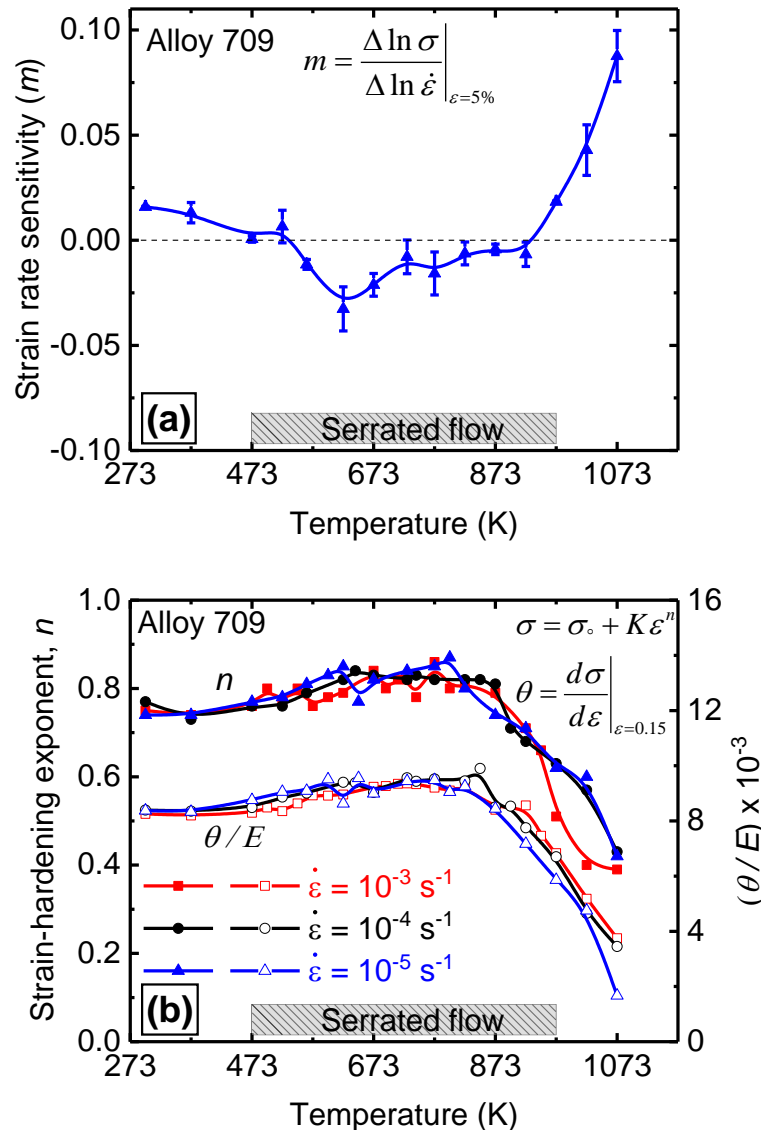
Figure 4.14. (a) Strain rate sensitivity (m) vs temperature. (b) Temperature variations of strain hardening exponent, n (left scale) and normalized work-hardening rate (θ/E) at true plastic strain of 0.15 (right scale) at different strain rates.

To estimate the strain-hardening exponent (n) and work hardening rate (θ) in the Alloy 709, true stress- true strain curves up to the point of necking were curve-fitted using the least square fit with Ludwik's equation: $\sigma = \sigma_o + K\varepsilon^n$ where σ_o, K and n are constants representing yield stress, strain hardening coefficient and strain hardening exponent

106

respectively. The correlation coefficients, R^2 for all fitting curves were higher than 0.98. The

work-hardening rate, θ is determined as $\theta = \dfrac{d\sigma}{d\varepsilon}$ (the first derivative of the Ludwik's

equation). Figure 4.14b shows the temperature variations of strain hardening exponent, *n* and

normalized work-hardening rate (θ/E) at true plastic strain of 0.15 at different strain rates. Both

exhibit peaks at intermediate temperatures where serrated flow occurs. Thus, the superior

ductility observed in the Alloy 709 during DSA regime is attributed to the relatively large

uniform strain resulting from the increase in the work hardening exponent at intermediate

temperatures in DSA regime [45]. High values of strain hardening exponent will enhance the

uniform elongation and hence the ductility [46]. At higher temperatures, the rapid increase in

total elongation and decrease in uniform elongation with temperature indicate reduced ability

for uniform deformation due to the early formation of macroscopic necking, and the majority

of strains are derived from post-necking deformation due to increased strain rate sensitivity at

high temperatures outside the DSA regime [47].

4.5. Conclusion

Tensile tests of the Alloy 709 (candidate structural material for Sodium-cooled Fast

Reactors) in a wide range of temperatures 298 – 1073 K (25 – 800 °C) and nominal strain rates

(10^{-5} – 10^{-3} s^{-1}) followed by microstructural evaluations were carried out to investigate the

serrated flow behavior resulting from DSA. The following conclusions are made:

1) Serrated flow was observed in the stress-strain curves within a specific regime of test

   temperatures identified as low-temperature regime (LT-SF) at 498 – 623 K (225 – 375 °C)

   and high temperature regime (HT-SF) at 623 – 973 K (375 – 700 °C) separated by mild

serrations or smooth flow. Types A and A+B and types A, A+B, A+C and C serrations were observed in the LT-SF and HT-SF respectively.

2) The activation energy, Q, for the onset of the serrated flow was evaluated using different methods and the average Q-values were found to be 103 ± 13 kJ/mole and 204 ± 11 kJ/mole respectively for the LT-SF and HT-SF.

3) Based on the activation energy values, the dependence of the critical strain on strain rate and the literature survey, diffusion of interstitial atoms such as nitrogen and/or carbon is thought to be responsible for serrations in the LT-SF regime while the diffusion of substitutional atoms such as chromium is operative in the HT-SF region.

4) The disappearance of serrations at high temperatures accompanied with the observation of type C serrations is thought to be due to the formation of carbide precipitates.

5) The observed plateaus and peaks in flow stresses, negative strain rate sensitivity, planar substructure and a relatively low fraction of LAGBs in deformed samples at intermediate temperatures were ascribed to the DSA at $498 – 973$ K ($225 – 700$ °C).

6) Increase in ductility (total elongation to fracture) was observed in the DSA regime compared to lower temperatures where no serrated flow is observed. This observation is opposite to the commonly reported loss in ductility due to DSA. The beneficial effect of the DSA in the Alloy 709 was attributed to the relatively high work hardening rate and strain hardening exponent resulting in large uniform strain and hence increased overall ductility.

4.6. References

[1] K.L. Murty, I. Charit, Structural materials for Gen-IV nuclear reactors: Challenges and opportunities, J. Nucl. Mater. 383 (2008) 189-195.

[2] W. Hoffelner, Materials for Nuclear Plants From Safe Design to Residual Life Assessments, 1st ed., Springer, Switzerland, 2013.

[3] J.T. Busby, Economic benefits of advanced materials in nuclear power systems, J. Nucl. Mater. 392(2) (2009) 301-306.

[4] W. Corwin, Advanced Structural Materials (RC-3), Nuclear Energy University Programs (NEUP), Fiscal Year (FY) 2015 Annual Planning Webinar, DOE, 2014.

[5] T.-L. Sham, L. Tan, Y. Yamamoto, Development of Advanced 9Cr Ferritic-Martensitic Steels and Austenitic Stainless Steels for Sodium-Cooled Fast Reactors, Fast Reactors and Related Fuel Cycles: Safe Technologies and Sustainable Scenarios (FR13), IAEA, Vienna, 2015, pp. 1-9.

[6] V.S. Srinivasan, M. Valsan, R. Sandhya, K. Bhanu Sankara Rao, S.L. Mannan, D.H. Sastry, High temperature time-dependent low cycle fatigue behaviour of a type 316L(N) stainless steel, Int. J. Fatigue 21(1) (1999) 11-21.

[7] Y.H. Jung, K.L. Murty, Effect of Temperature and Strain Rate on Upper Shelf Fracture Behavior of A533B Class 1 Pressure Vessel Steel, in: T.A. Cruse (Ed.), Fracture Mechanics: Nineteenth Symposium, ASTM, STP 969, Philadelphia, 1988, pp. 392-401.

[8] M. Doner, H. Conrad, Deformation mechanisms in commercial Ti (0.5 at. pct oineq) at intermediate and high temperatures (0.3 - 0.6 tinm), Metall. Trans. 4 (1973) 2809-2817.

[9] S.I. Hong, W.S. Ryu, C.S. Rim, Elongation Minimum and Strain Ram Sensitivity Minimum of Zircaloy-4 J. Nucl. Mater. 116 (1983) 314-316.

[10] E. Bouchaud, L. Kubin, H. Octor, Ductility and dynamic strain aging in rapidly solidified aluminum alloys, Metallurgical Transactions: A 22 (1991) 1021-1028.

[11] C. Gupta, J.K. Chakravartty, S.L. Wadekar, J.S. Dubey, Effect of serrated flow on deformation behaviour of AISI 403stainless steel, Mater. Sci. Eng., A 292 (2000) 49-55.

[12] B.K. Choudhary, Influence of Strain Rate and Temperature on Tensile Deformation and Fracture Behavior of Type 316L(N) Austenitic Stainless Steel, Metall. Trans. A 45 (2014) 302-316.

[13] K.L. Murty, E.O. Hall, Dynamic Strain-Aging and Neutron Irradiation in Mild Steel in: Irradiation Effects on the Microstructure and Properties of Metals, ASTM STP 611,1976, pp. 53-71.

[14] A. Sarkar, S.A. Maloy, K.L. Murty, Investigation of Portevin−Le Chatelier effect in HT-9 steel, Mater. Sci. Eng., A 631 (2015) 120-125.

[15] B.J. Brindley, P.J. Worthington, Yield-point phenomena in substitutional alloys, Metall. Rev. 15(1) (1970) 101-114.

[16] P. Rodriguez, Serrated plastic flow, Bull. Mater. Sci. 6 (1984) 653-663.

[17] C.F. Jenkins, G.V. Smith, Serrated plastic flow in austenitic stainless steel, Trans. Metall. Soc. AIME 245 (1969) 2149–56.

[18] L.H.D. Almeida, I.L. May, S.N. Monteiro, Effects of Carbon and Nitrogen Levels on the Temperture Ranges for Serrated Flow in Austenitic Stainless Steel, in: H.J. McQueen, J.P. Bailon, J.I. Dickson, J.J. Jonas, M.G. Akben (Eds.), Strength of Metals and Alloys (ICSMA 7), Pergamon Press, Oxford, 1985, pp. 337-342.

[19] L.H. de Almeida, I.L. May, S.N. Monteiro, Athermal and temperature dependent behavior of serrated flow in an austenitic stainless steel, Scr. Metall. 19(12) (1985) 1451-1454.

[20] K.G. Samuel, S.L. Mannan, P. Rodriguez, Serrated Yielding in AISI 316 Stainless Steel, Acta Metall. 36 (1988) 2323-2327.

[21] K.G. Samuel, S.K. Ray, G. Sasikala, Dynamic strain ageing in prior cold worked 15Cr–15Ni titanium modified stainless steel (Alloy D9), J. Nucl. Mater. 355(1) (2006) 30-37.

[22] L.J. Meng, J. Sun, H. Xing, G.W. Pang, Serrated flow behavior in AL6XN austenitic stainless steel, J. Nucl. Mater. 394(1) (2009) 34-38.

[23] A.H. Cottrell, LXXXVI. A note on the Portevin-Le Chatelier effect, Lond. Edinb. Phil. Mag. 44(355) (1953) 829-832.

[24] P.G. McCormick, A model for the Portevin-Le Chatelier effect in substitutional alloys, Acta Metall. 20 (1972) 351-354.

[25] A. van den Beukel, Theory of the effect of dynamic strain aging on mechanical properties, Phys. Status Solidi A 30 (1975) 197-206.

[26] A.V.D. Beukel, On the mechanism of serrated yielding and dynamic strain ageing, Acta Metall. 28(7) (1980) 965-969.

[27] L.P. Kubin, Y. Estrin, Dynamic strain ageing and the mechanical response of alloys, J. Phys. III 1 (1991) 929-943.

[28] K. Linga Murty, F.A. Mohamed, J.E. Dorn, Effect of vacancy sinks and sources on serrated yielding due to solute locking, Scr. Metall. 5 (1971) 1087-1091.

[29] S. Venkadesan, C. Phaniraj, P.V. Sivaprasad, P. Rodriguez, Activation Energy For Serrated Flow In A 15Cr-15Ni Ti-Modified Austenitic Stainless Steel, Acta Metall. Mater. 40 (1992) 569-580.

[30] B.K. Choudhary, Activation energy for serrated flow in type 316L(N) austenitic stainless steel, Mater. Sci. Eng., A 603 (2014) 160-168.

[31] E.G. Wilson, Stress varied creep of 20%Cr-25%Ni-Nb stabilized austenitc stainless steel, Creep strength in steel and high temperature alloys, The Metal Society, London, 1972, pp. 111-121.

[32] T. Sourmail, Precipitation in creep resistant austenitic stainless steels, Mater. Sci. Technol. 17(1) (2001) 1-14.

[33] A.S. Alomari, N. Kumar, K.L. Murty, Creep Behavior and Microstructural Evolution of a Fe-20Cr-25Ni (Mass Percent) Austenitic Stainless Steel (Alloy 709) at Elevated Temperatures, Metall. Trans. A, 2018.

[34] K.S.B. Rose, S.G. Glover, A study of strain-ageing in austenite, Acta Metall. 14(11) (1966) 1505-1516.

[35] A.F. Smith, G.B. Gibbs, Volume and Grain-Boundary Diffusion in 20 Cr/25/Ni_Nb Stainless Steel, Met. Sci. J. 3 (1969) 93-94.

[36] K.L. Murty, K. Detemple, O. Kanert, J.T.M. Dehosson, In-situ nuclear magnetic resonance investigation of strain, temperature, and strain-rate variations of deformation-induced vacancy concentration in aluminum, Metall. Trans. A 29 (1998) 153-159.

[37] R.W. Hayes, W.C. Hayes, A proposed model for the disappearance of serrated flow in two Fe alloys, Acta Metall. 32(2) (1984) 259-267.

[38] S.L. Mannan, K.G. Samuel, P. Rodriguez, The Influence of Grain Size on Elevated Temperature Deformation Behaviour of a Type 316 Stainless Steel, in: R.C. Gifkins (Ed.), Strength of Metals and Alloys (ICSMA 6), Pergamon, Melbourne, 1982, pp. 637-642.

[39] X. Feaugas, On the origin of the tensile flow stress in the stainless steel AISI 316L at 300 K: back stress and effective stress, Acta Mater. 47(13) (1999) 3617-3632.

[40] W. Karlsen, M. Ivanchenko, U. Ehrnstén, Y. Yagodzinskyy, H. Hänninen, Microstructural manifestation of dynamic strain aging in AISI 316 stainless steel, J. Nucl. Mater. 395 (2009) 156-161.

[41] V.D. Vijayanand, K. Laha, P. Parameswaran, M. Nandagopal, S. Panneer Selvi, M.D. Mathew, Influence of thermo-mechanical treatment on the tensile properties of a modified 14Cr–15Ni stainless steel, J. Nucl. Mater. 453 (2014) 188-195.

[42] V. Ramachandran, R.E. Reed-Hill, Dynamic strain aging and ductility minima in zirconium, Metall. Trans. 1(8) (1970) 2105-2109.

[43] A. Chiba, X.G. Li, M.S. Kim, High work-hardening rate and deformation twinning of Co-Ni-based superalloy at elevated temperatures, Philos. Mag. A 79(7) (1999) 1533-1554.

[44] X. Bian, F. Yuan, X. Wu, Correlation between strain rate sensitivity and characteristics of Portevin-LeChátelier bands in a twinning-induced plasticity steel, Mater. Sci. Eng., A 696 (2017) 220-227.

[45] A.S. Alomari, N. Kumar, K.L. Murty, Enhanced ductility in dynamic strain aging regime in a Fe-25Ni-20Cr austenitic stainless steel, Mater. Sci. Eng., A 729 (2018) 157-160.

[46] K.L. Murty, I. Charit, An Introduction to Nuclear Materials : Fundamentals and Applications, Wiley-VCH, Weinheim, 2013.

[47] D.W. Woodford, Strain rate sensitivity as a measure of ductility, Trans. ASM 62 (1969) 291-293.

5. CREEP BEHAVIOR AND MICROSTRUCTURAL EVOLUTION OF A Fe-20Cr-25Ni (MASS PCT) AUSTENITIC STAINLESS STEEL (ALLOY 709) AT ELEVATED TEMPERATURES[2]

Abstract

Understanding creep properties and microstructural evolution for candidate materials of the next-generation nuclear reactors are essential for design and safety considerations. In this work, creep tests were carried out at temperatures ranging from 973 – 1073 K and stresses 40 – 275 MPa followed by microstructural examinations of a Fe-20Cr-25Ni (mass pct) austenitic stainless steel (Alloy 709), a candidate structural material for the Sodium-cooled Fast Reactors. The apparent stress exponent and activation energy were found to be 6.8 ± 0.4 and 421 ± 38 kJ/mole respectively. The higher activation energy relative to that of lattice self-diffusion together with the observation of dislocation-precipitate interactions in the crept specimens were rationalized based on the concept of threshold stress. The threshold stresses were estimated using a linear extrapolation method and found to decrease with increased temperature. By invoking the concept of threshold stresses, the true stress exponent and activation energy were found to be 4.9 ± 0.2 and 299 ± 15 kJ/mole, respectively. Together with the observation of subgrain boundary formation, the rate-controlling mechanism in the Alloy 709 was conclusively determined to be the high temperature dislocation climb. Three types of precipitates were identified in the crept samples: Nb(C, N), Z-phases of sizes between 20 – 200 nm within the matrix and $M_{23}C_6$ with sizes between 200 – 700 nm within the matrix and on grain boundaries. Further, the analysis of creep rupture data at high stresses indicated that the Alloy 709 obeyed Monkman–Grant and modified Monkman–Grant relationships with creep damage tolerance factor of ~ 5. Using the Larson-Miller parameter, it was concluded that

---

[2] *This chapter is published in journal of Metallurgical and Materials Transactions A.*

the Alloy 709 exhibited superior creep strengths relative to the other advanced austenitic steels.

5.1. Introduction

Austenitic stainless steels have been widely used as major structural materials in nuclear reactors owing to their excellent oxidation and corrosion resistance along with elevated temperature mechanical properties. However, advanced materials with superior high-temperature performance are needed for the Gen-IV nuclear reactors to endure harsh operating conditions including higher operating temperatures in comparison with the current fleet [1-3]. It is known that Ni-based superalloys (such as Alloy 617) possess higher creep strength in comparison to ferritic and austenitic stainless steels. However, other design factors have to be considered for materials selection in Gen-IV nuclear reactors such as radiation effects and effective cost. For example, Ni-based alloys suffer from serious irradiation embrittlement due to the formation of bubbles on grain boundaries resulting from the formation of transmuted He mainly generated by (n, α) nuclear reaction of nickel [1, 4]. Further, Ni-based superalloys are relatively costly than steels. Thus, developing advanced austenitic stainless steels with superior properties is vital to improve the economics for the next-generation nuclear reactors through the reduction of the commodities and the raw materials required for the structural components, assuming all other design factors are still adequate [3].

The majority of the newly developed steels rely on the fine scale precipitations for their high temperature creep strength by adding specific type of substitutional (such as Nb or Ti) and interstitial (C and N) alloying elements in a controlled way [5]. The common types of precipitates employed in the creep-resistant austenitic stainless steels are Z and MX phases, where M is a carbide- or nitride-forming element such as Ti, Nb, V, or Hf, and X is C or N. One of such advanced alloys is a Nb-containing and nitrogen stabilized Fe-20(mass pct) Cr-

114

25Ni austenitic stainless steel (here afterwards referred to as Alloy 709) which is an excellent candidate material for structural applications for Sodium-cooled Fast Reactors due to the desired set of mechanical properties found during preliminary investigations including high temperature characteristics, sodium compatibility and thermal stability relative to code-approved reference structural materials such as 304 and 316 stainless steels [6, 7]. The Alloy 709 was developed based on the Nb/Ti stabilized 20Cr-25Ni stainless steel in the mid-1980s for ultra supercritical fossil power plants [8] and fuel-cladding in advanced gas-cooled reactors where improved mechanical properties were achieved by forming the Nb(C, N) and TiN particles in these alloys [5, 9, 10].

Understanding the creep behavior along with their constitutive equations and microstructural evolution is essential not only for predicting the life of the alloy but also for developing more creep-resistant microstructures. Several creep mechanisms are known to control the rate of deformation in austenitic stainless steels and Ni-based superalloys including dislocation-controlled creep or diffusional creep and their associated characteristics [11-19]. Recently, research efforts on the Alloy 709 have focused on precipitation behavior [20], radiation effects [21, 22], nanoindentation behavior [23], thermophysical properties [24] and serrated flow and tensile properties [25-27]. The current study is focused on the creep behavior and microstructural evolution of the Alloy 709 at elevated temperatures. Constant load creep tests at temperatures ranging from 973 – 1073 K and stresses of 40 – 275 MPa followed by microstructure evaluations are reported and discussed in terms of creep deformation mechanisms, microstructures and creep rupture properties.

5.2. Material and experimental methods

The Alloy 709 used in this investigation was received in the form of a hot forged (at

1373 K followed by water quenching) 25 mm thick rectangular plate. The chemical composition is listed in Table 5.1. Rectangular pin-loaded specimens were machined from the as-received plate with a gage length of 25.4 mm, thickness of 1.2 mm and width of 6.3 mm for creep tests (Figure 5.1c). Uniaxial creep tests were conducted in air using a constant load lever arm machine employed with a three-zone furnace at temperatures ranging from 973 – 1073 K and initial applied stresses of 40 – 275 MPa. The temperature was measured using two K-type thermocouples attached to the gage section of the sample and maintained within ±1 K during tests. The extension of the sample was measured with an accuracy of 2 µm displacement (or 0.008 pct strain) using a Linear Differential Variable Capacitance (LVC) transducer attached to a high temperature extensometer. Figure 5.1a and Figure 5.1b show the creep tester and the experimental set up used in this study. Before testing, the specimens were soaked for 30 minutes at the test temperature without applied load to ensure the homogeneity of the temperature over the entire gage length. The tests conducted at high stresses were continuously run to a final fracture of the specimens. At low stresses, the creep tests were interrupted during the secondary creep stage with some amount of true strains and selected tests were repeated to ensure the reproducibility of the experimental data. When the test is repeated, average values with error bars corresponding to the standard deviations are noted. The ultimate tensile strengths for the Alloy 709 measured at the creep temperatures of 973, 1023 and 1073 K and a strain rate of 10^{-3} s^{-1} were found to be 406, 345 and 273 MPa respectively [25].

Transmission electron microscopy (TEM) was utilized to characterize the microstructures of the Alloy 709 before and after creep deformation using a JEOL 2000FX TEM (operated at 200 kV) at Advanced Instrumentation Facility (AIF), NC State University. Sections were cut from the as-machined tensile specimens for examining the initial

116

microstructure before creep testing. In order to preserve the microstructures after deformation, creep tests were stopped and rapidly cooled using a fan to bring the sample down to room temperature under load with cooling rate of approximately 3 °C/second. Cuts along the transverse direction of the gage section of the deformed samples using a diamond saw were mechanically polished down to 100 µm using SiC papers of 600 to 1200 grit. Subsequently, 3 mm diameter disks were punched out from the foil and were electro-polished till perforation to produce electron transparent regions within the disk using a Fischione twin-jet electropolisher in 10 vol. pct perchloric and 90 vol. pct methanol solution at 238 K using liquid nitrogen at a voltage of 30 V. Elemental maps for the second phases were obtained using a high angle annular dark field decorator attached to FEI Titan 80-300 scanning-transmission electron microscope operated at AIF. The fractured samples were ultrasonically cleaned in acetone for 3 hours before performing fractography in the SEM, FEI Quanta 3D FEG at an accelerating voltage of 20 kV.

Table 5.1. Chemical compositions (mass pct) of the Alloy 709.

Element	Compositions (wt. %)
C	0.063
Mn	0.88
Si	0.28
P	<0.005
S	<0.001
Cr	19.69
Ni	25
Mo	1.46
N	0.14
Ti	<0.01
Nb	0.23
B	0.0022
Fe	bal.
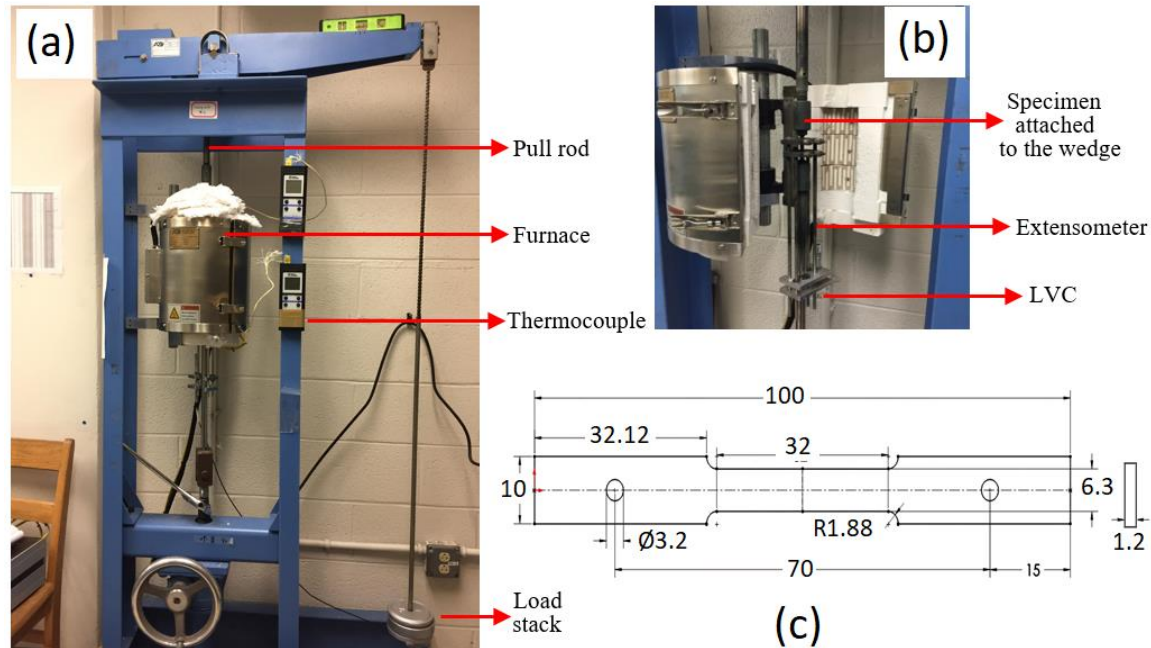
Figure 5.1. (a) Lever arm creep tester. (b) Closer view of the specimen and extensometer. (c) Creep test specimen geometry where all dimensions are in mm.

5.3. Results

5.3.1. Initial microstructures

The microstructure for the as-received Alloy 709 exhibited nearly equiaxed austenite grains with an average size of 36.8 ± 7.3 μm determined by using the line intercept method and TEM micrographs are shown in Figure 5.2 along with corresponding selected area electron diffraction (SAED) patterns. A relatively low density of dislocations and annealing twins were observed in the as-received alloy. Moreover, preexisting fine spherical precipitates are uniformly distributed within the grains with an average radius of 44.5 ± 22 nm. Figure 5.2c shows a higher magnification bright field TEM image taken at $[1\bar{1}2]$ zone axis. SAED pattern taken around the precipitate area encircled in Figure 5.2c is shown in Figure 5.2d, and the precipitates are noted to have a lattice parameter slightly larger than that of austenite matrix.

These undissolved precipitates were found to be Nb-rich second phase as seen in a high-angle
annular dark-field (HAADF) image (Figure 5.3) along with its elemental map of Nb.
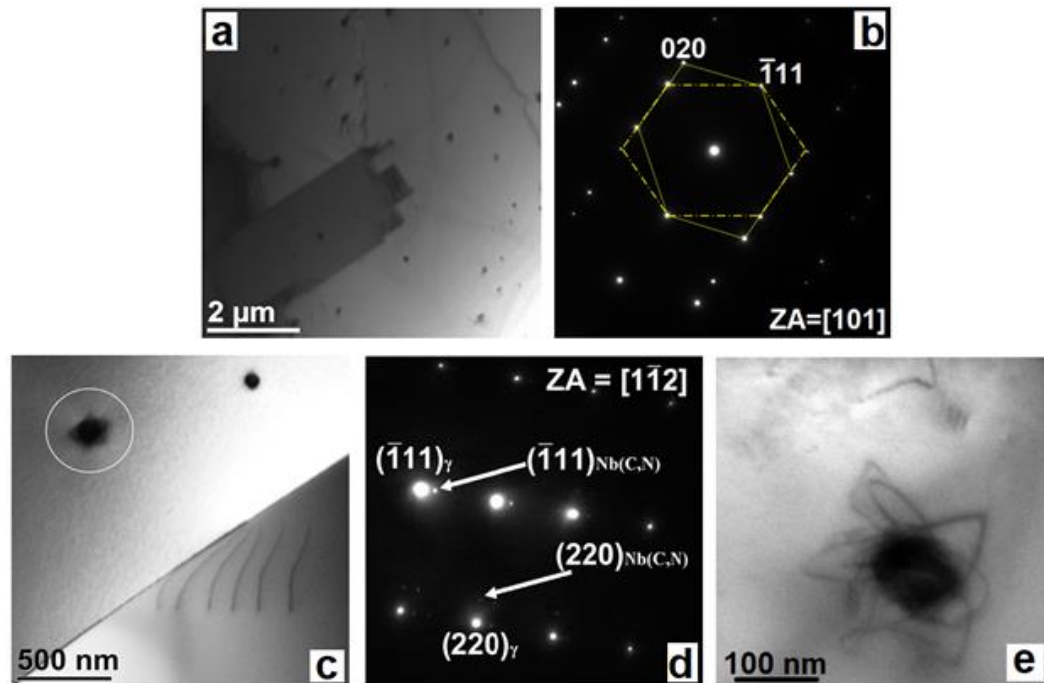
Figure 5.2. (a) Bright field TEM image for the as-received Alloy 709 showing the presence of undissolved precipitates and twin boundary. (b) Selected area electron diffraction (SAED) pattern of (a) showing the reflections of the two orientations on each side of the twin boundary at the zone axis [101]. (c) Bright field TEM image for the as-received Alloy 709 showing dislocation pile-up at a boundary and undissolved Nb(C, N) precipitates. (d) SAED pattern corresponding to zone axis $[1\bar{1}2]$ acquired from the area encircled in (c) indicating the reflections of the matrix and Nb(C, N) precipitate. (e) A higher magnification TEM micrograph showing a Nb(C, N) particle surrounded by some dislocations.

These particles were identified to be MX-type precipitates (here afterward referred to as Nb (C, N) precipitates) which are usually observed in Nb-containing austenitic stainless steels. Nb(C, N) precipitates were usually found to be surrounded by some dislocations (Figure 5.2e) which may have been formed during quenching process due to the different thermal expansion coefficients of the particle and the matrix. No other phases were found in the as-received Alloy 709.
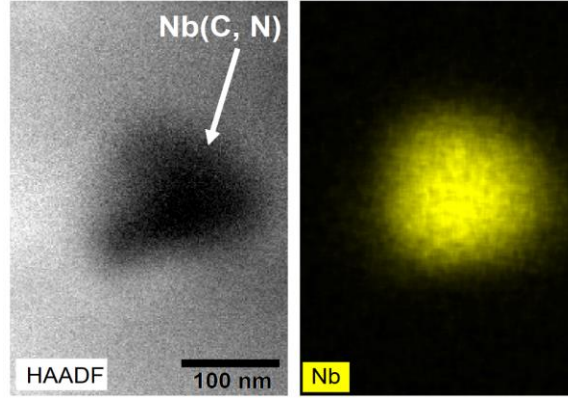
Figure 5.3. High-angle annular dark-field (HAADF) image for a typical precipitate observed in the as-received Alloy 709 with a corresponding elemental map of Nb.

5.3.2. Creep curves and minimum creep rate characteristics

Typical creep rupture curves of the Alloy 709 tested at 1023 K and 150 – 250 MPa stresses are shown in Figure 5.4a while the creep rate as a function of time is shown in Figure 5.4b. At all temperatures, normal creep curves are usually observed (i.e. primary creep regime with decreasing rate, secondary creep regime with constant creep rate corresponding to a steady state or minimum creep rate, $\dot{\varepsilon}_m$, and tertiary creep regime with increasing creep rate with time until failure). Figure 5.5a shows the creep curves at 1023 K and at 60 – 100 MPa for the interrupted creep tests at the secondary creep regime. Corresponding creep rates as a function of time for interrupted tests are shown in Figure 5.5b.

The minimum creep rate, $\dot{\varepsilon}_m$ is found to be related to the applied stress, σ through a power law relation,

$$\dot{\varepsilon}_m = A'\sigma^{n_a} \exp(-\frac{Q_a}{RT}) \tag{5.1}$$

where A' constant, n_a the apparent stress exponent, Q_a the apparent activation energy for creep, R the universal gas constant and T the test temperature. Figure 5.6a shows the $\dot{\varepsilon}_m$ versus σ at temperatures 973 – 1073 K in log-log scale which yielded apparent stress exponent

values ranging from 6.4 – 7.1 with an average value of $\overline{n_a} = 6.8 \pm 0.4$. An Arrhenius plot of

the $\dot{\varepsilon}_m$ versus reciprocal of the absolute temperature at different stress levels is shown in Figure

5.6b where Q_a for creep deformation was found to be in the range of 385 – 461 kJ/mole with

an average value of $\overline{Q_a} = 421 \pm 38$ kJ/mole.

For samples tested until fracture, the time to rupture (t_f), minimum creep rate ($\dot{\varepsilon}_m$)

and creep strain to failure (creep ductility, ε_f) at different stresses and temperatures are

reported in Table 5.2. Overall, the time to rupture was found to increase as the applied stress

or temperature decreased. The creep ductility varied between ~ 20 pct – 55 pct depending on

the test temperature and the applied stress.

The variation of t_f as a function of the minimum creep rate at different temperatures

for the Alloy 709 is shown in Figure 5.7a. The alloy is found to follow the Monkman-Grant

relation expressed as,

$$\dot{\varepsilon}_m^{\alpha} \; t_f = C_{MG} \tag{5.2}$$

where α and C_{MG} are constants found to be 1.1 $\pm$ 0.1 and 0.043 $\pm$ 0.005 respectively.

Furthermore, the interrelation between time to rupture and the applied stress was demonstrated

by the applicability of the Larson-Miller parameter (LMP) for the Alloy 709 using the

expression,

$$LMP = T \cdot [C + \log(t_f)] \tag{5.3}$$

where T is in K, t_f in hr and C a constant equal to 20. Figure 5.7b shows the applied stress

versus LMP at different temperatures and it is clearly seen that values of LMP are found to be

independent of the temperature at a given stress. The estimated temperatures in K for 100,000

hours rupture life using LMP are also shown in the top x-axis in Figure 5.7b.

Table 5.2. The test matrix and creep results of the Alloy 709.

Temperature (K)	Applied stress (MPa)	Time to rupture, t_f or interruption (hr)	$\dot{\varepsilon}_m$ (hr^{-1})	Creep strain to failure or interruption (pct)
973	100	1111.6	1.26×10^{-6}	0.53
	150	450.1	3.24×10^{-5}	3.59
	250	9.86	1.15×10^{-3}	1.7
	200	434.1*	2.43×10^{-4}	51.5*
	225	166.4*	5.04×10^{-4}	55.3*
	275	38.4*	1.22×10^{-3}	19.8*
1023	60	578.1	3.24×10^{-7}	0.11
	80	380.8	4.32×10^{-6}	0.31
	100	343.2	1.76×10^{-5}	1.04
	125	131.6	1.01×10^{-4}	1.94
	150	236.1*	5.04×10^{-4}	44.4*
	200	31.6*	2.71×10^{-3}	35.4*
	250	7.52*	9.90×10^{-3}	23.3*
1073	40	1033.7	5.40×10^{-7}	0.328
	80	408.4	6.73×10^{-5}	1.28
	100	328.5*	2.25×10^{-4}	39.8*
	150	24.1*	3.20×10^{-3}	52.2*
	200	3.3*	1.79×10^{-2}	37.6*

* Creep rapture test.
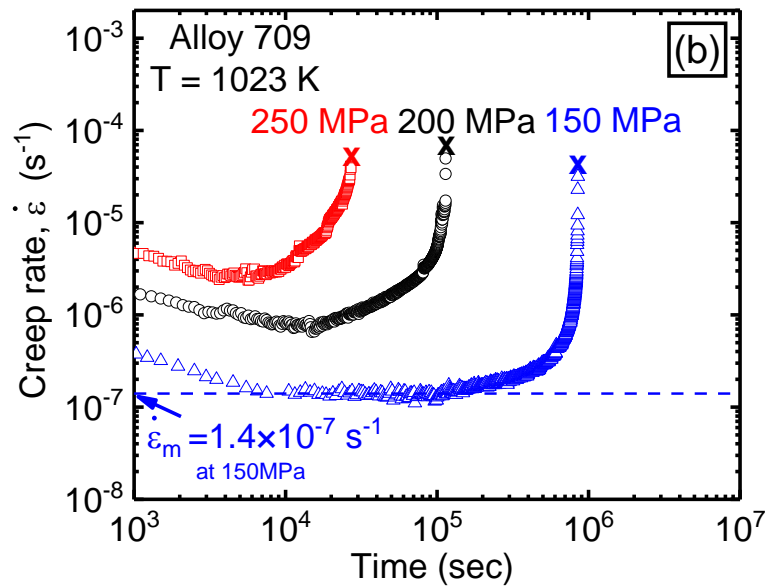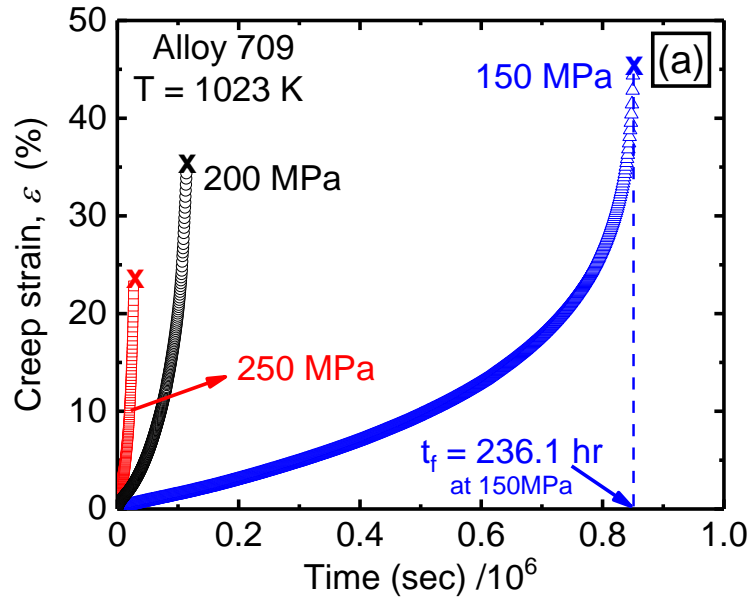
Figure 5.4 (a) Creep rupture curves at 1023 K and different stresses for the Alloy 709. (b) Creep rate as a function of time. (X symbol indicating that sample ruptured).
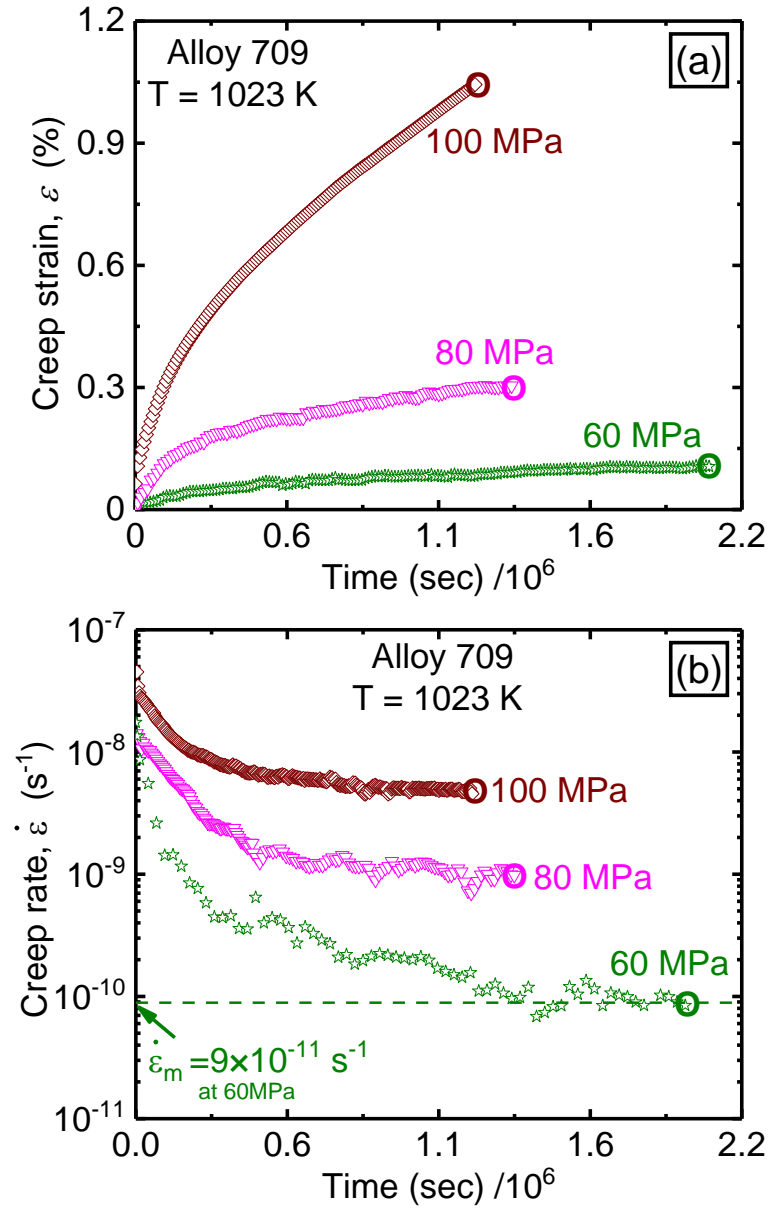
Figure 5.5. (a) Creep curves at 1023 K and different stresses for the Alloy 709. (b) Creep rate as a function of time. (O symbol indicating test interruption).
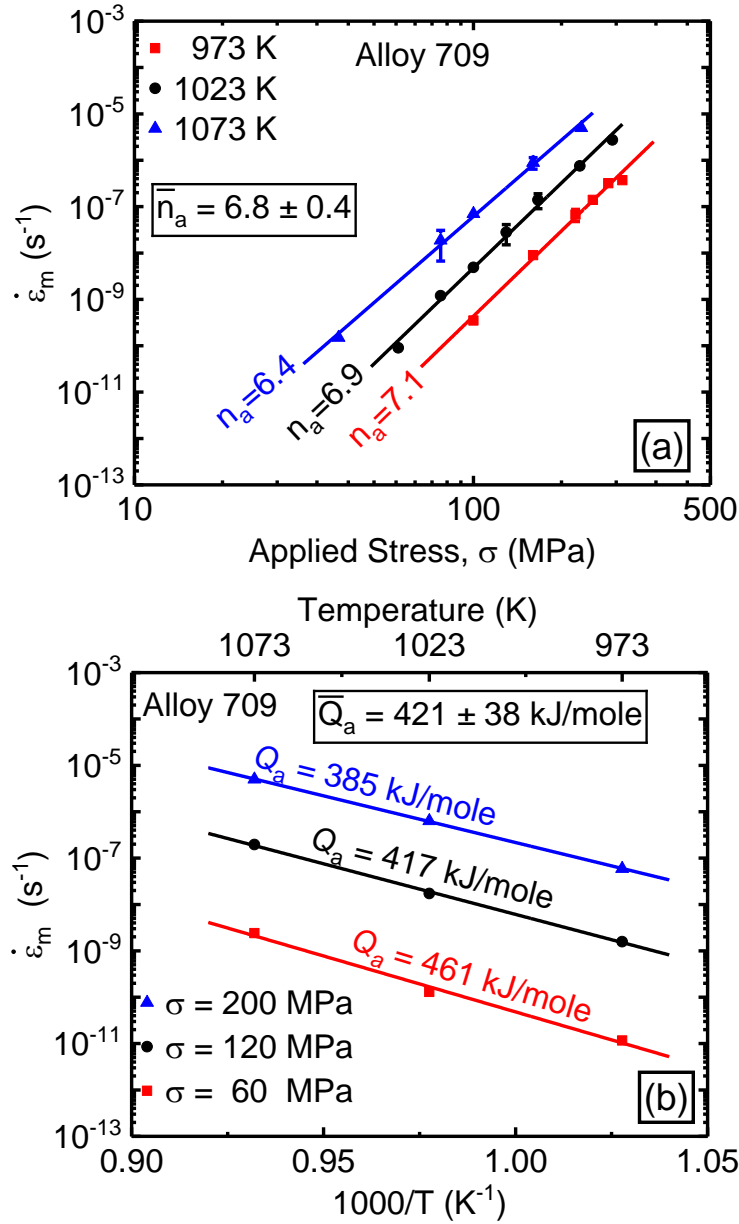
Figure 5.6. (a) Log-log plot of the minimum creep rate versus applied stress at various temperatures for the Alloy 709. (b) Semilog plot of the $\dot{\varepsilon}_m$ versus the reciprocal temperature at various applied stresses. Error bars are the standard deviations determined from repeated tests.
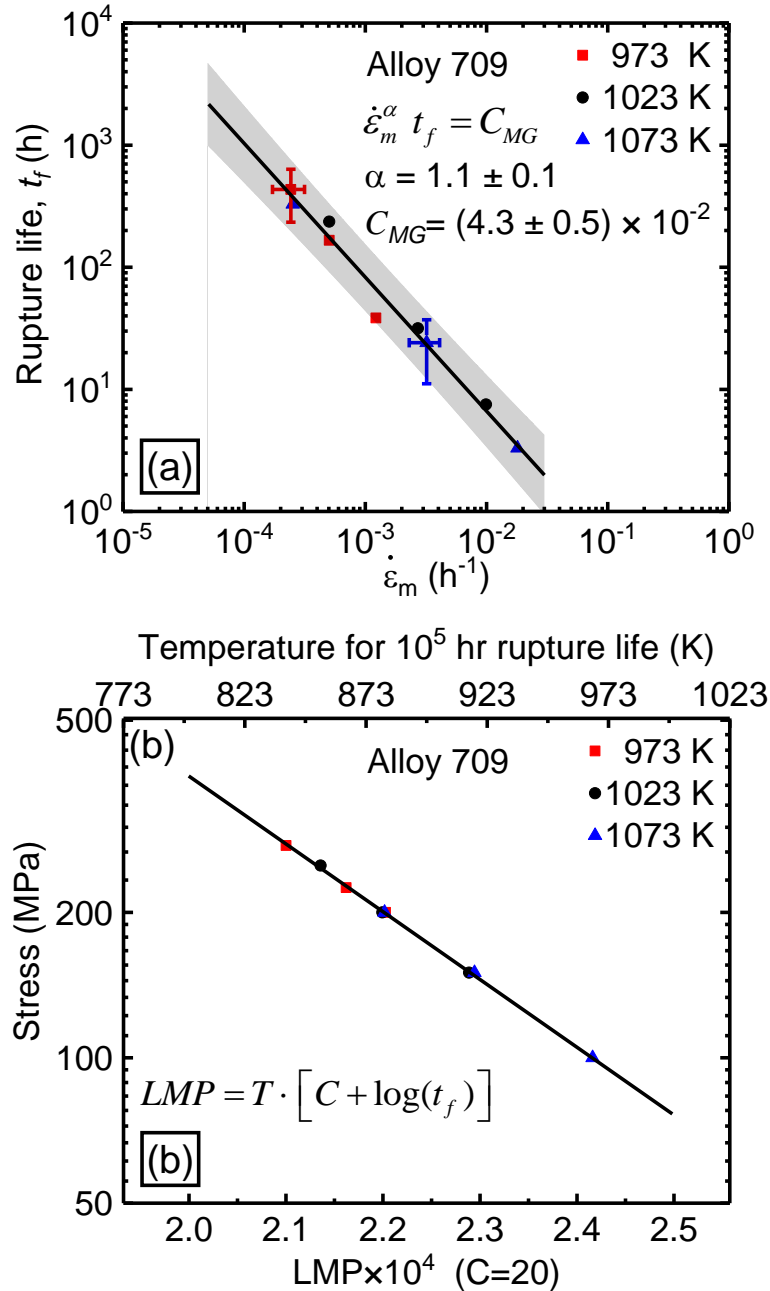
Figure 5.7. (a) Log-log plot of the rupture life versus minimum creep rate exhibiting Monkman-Grant relation. (b) Larson-Miller parameter (LMP) plot at different temperatures for the Alloy 709 and the temperatures for 100,000 hours rupture life is also shown on the top x-axis.

5.3.3. Microstructural examination of crept samples

Selected crept samples were examined under TEM and HAADF-STEM. In addition to the preexisting Nb(C, N) precipitates, creep deformation resulted in the formation of other precipitates with coarse (200 – 700 nm) and fine sizes (< 200 nm) within the matrix and at

126

grain boundaries. Figure 5.8 shows the TEM microstructure of the sample crept at 1023 K and 100 MPa strained up to 1 pct in the steady state creep regime. Coarse and fine particles within the grains are seen in Figure 5.8a. Figure 5.8b and Figure 5.8c include the SAED patterns for the matrix and the coarse precipitate respectively, where the latter has the same FCC structure as the austenite matrix and a cube-to-cube orientation relationship with a lattice parameter about three times larger than that of the matrix. The SAED pattern for theses coarse precipitates is consistent with the $M_{23}C_6$ carbides usually observed in stainless steels. The fine precipitates of sizes ranging from 10 – 200 nm are shown in the TEM micrograph taken at two beam condition (Figure 5.8d) where dislocation-precipitate interactions are clearly noted. Evidence for the dislocation line bypassing a Nb-rich precipitate possibly by climb is shown in Figure 5.8e and Figure 5.8f using a higher resolution bright field and dark field TEM images. In addition, Figure 5.8g exhibits dislocations pinned by fine-scale precipitates. Figure 5.8h and Figure 5.8i show chain-like and plate-like morphologies of $M_{23}C_6$ precipitates on grain boundaries and twin boundaries respectively, which were typically observed in crept samples.

The fine precipitates of less than 200 nm size were examined under HAADF-STEM to determine their chemical make-up. Three types of precipitates were observed in crept samples. Figure 5.9a shows HAADF image of the Alloy 709 crept at 1023 K and 100 MPa to 1 pct strain exhibiting a particle with both niobium and chromium and these Nb- and Cr-rich particles were usually observed in grain interiors and at grain boundaries with sizes ranging from 20 – 100 nm. These precipitates are identified to be Z-phases as reported in austenitic steels containing both niobium and nitrogen. HAADF-STEM image for a cluster of precipitates and corresponding elemental maps of Nb and Cr are shown in Figure 5.9b exhibiting the presence of both Nb(C, N) and $M_{23}C_6$ particles.
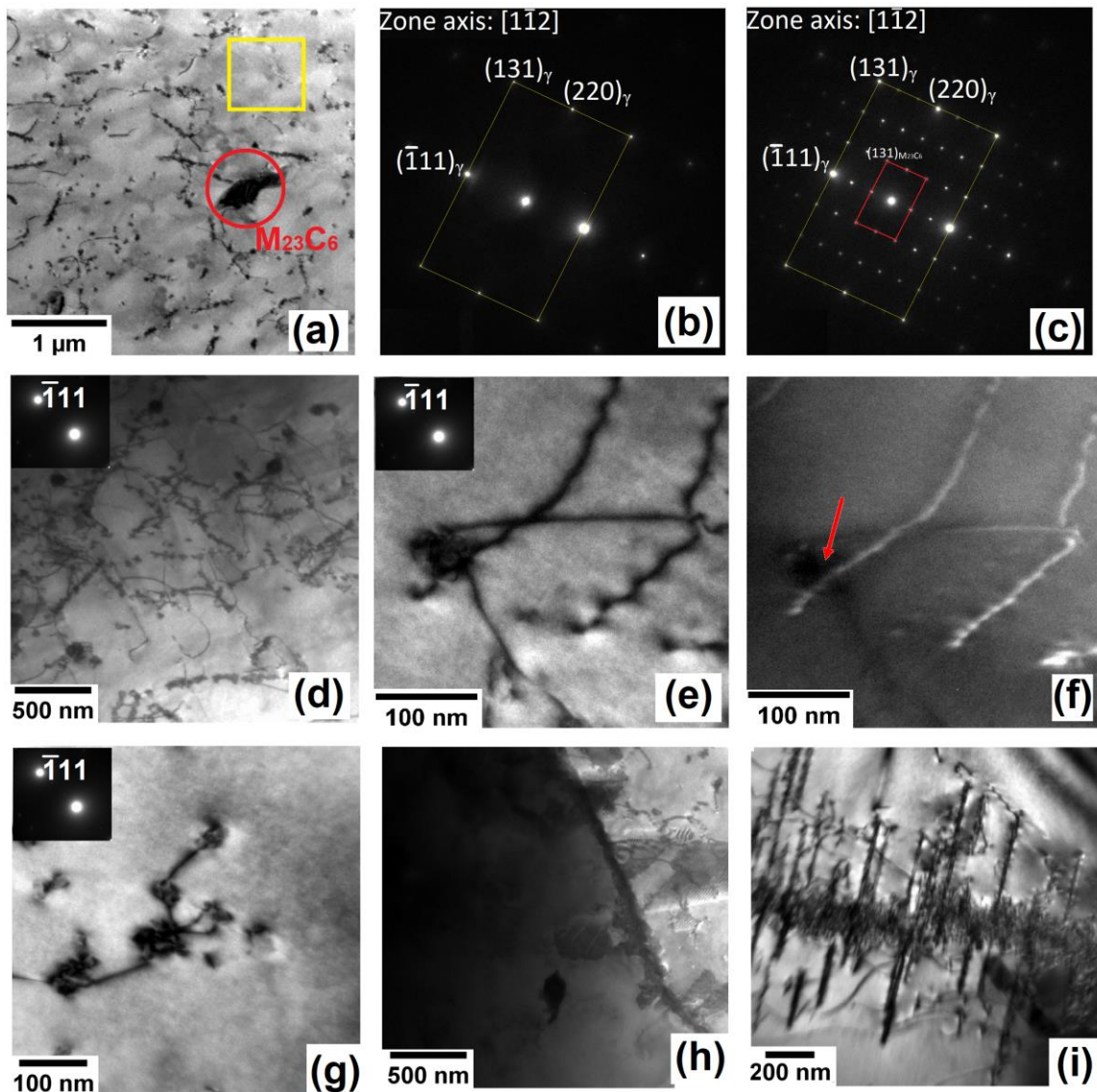
Figure 5.8. The microstructure of the Alloy 709 crept at 1023 K and 100 MPa to 1 pct strain (a) Bright field TEM image showing large and fine precipitates within the grain. (b) and (c) SAED patterns acquired from the square and circle areas noted in (a) respectively showing typical reflections of the austenite matrix and $M_{23}C_6$ precipitate at zone axis of $[1\bar{1}2]$. (d) The interaction of dislocations with fine precipitates. (e), (f) and (g) Higher magnification TEM micrographs with detailed dislocation-precipitate interactions. (h) and (i) Chain-like and plate-like $M_{23}C_6$ observed on grain boundary and the twin boundaries respectively.
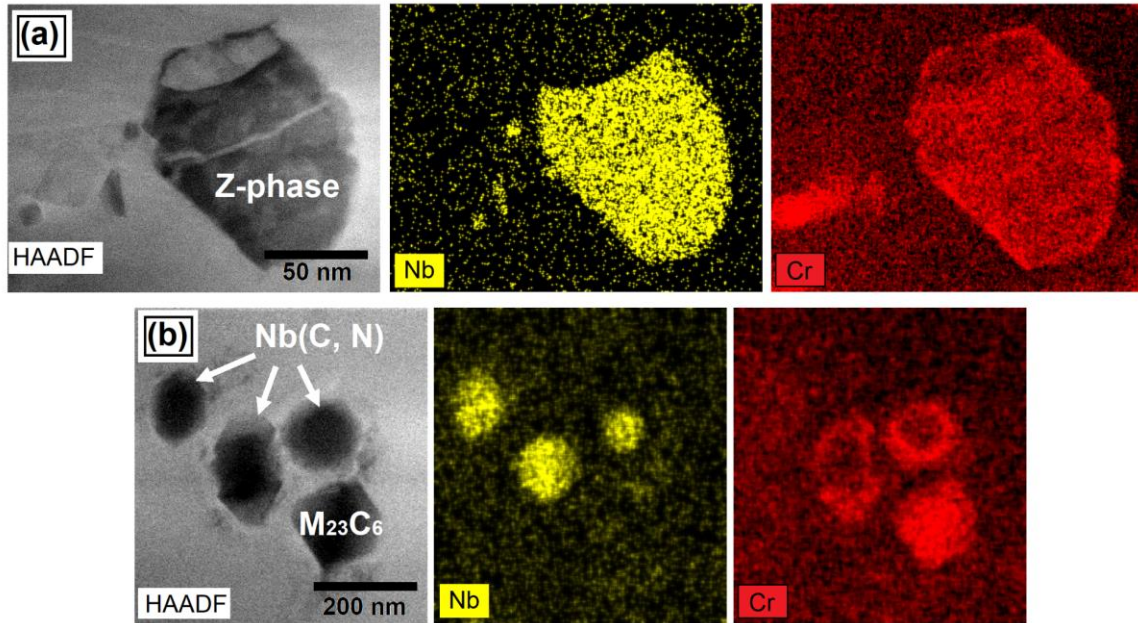
Figure 5.9. High-angle annular detector dark-field scanning transmission electron micrographs (HAADF-STEM) along with elemental maps of Nb and Cr for the Alloy 709 crept at 1023 K and 100 MPa to 1 pct strain showing (a) Z-phase, (b) Nb(C, N) and $M_{23}C_6$ precipitates.

Figure 5.10a is a bright field TEM image taken at two beam condition for the Alloy 709 crept samples at 40 MPa and 1073 K to 0.3 pct showing subgrain formation. Figure 5.10b and Figure 5.10c are TEM micrographs of samples crept at 275 MPa and 973 K, and at 150 MPa and 1073 K respectively. Large precipitates of a few micrometers size and finely dispersed precipitates of nano size were also found in the ruptured samples. The dislocation density is relatively higher for the sample crept at 275 MPa and 973 K than that at 150 MPa and 1073 K. Furthermore, the fractured surfaces of ruptured specimens were characterized using SEM and a typical fracture surface of a crept specimen at 1023 K and 200 MPa is shown in Figure 5.11 depicting ductile fracture characterized by the presence of dimples with cavitation.
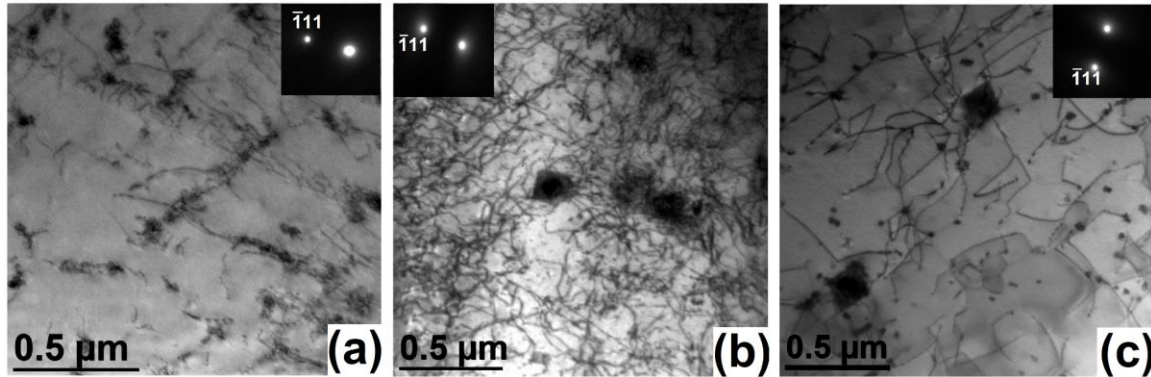
Figure 5.10. Bright field TEM micrographs of the Alloy 709 crept samples at (a) 40 MPa and 1073 K strained to 0.3 pct showing subgrain formation, (b) 275 MPa and 973 K strained to fracture (~20 pct creep strain) with a high density of dislocations, and **(c)** 150 MPa and 1073 K strained to fracture (~ 52 pct creep strain). Corresponding SAED patterns are included in the insets.
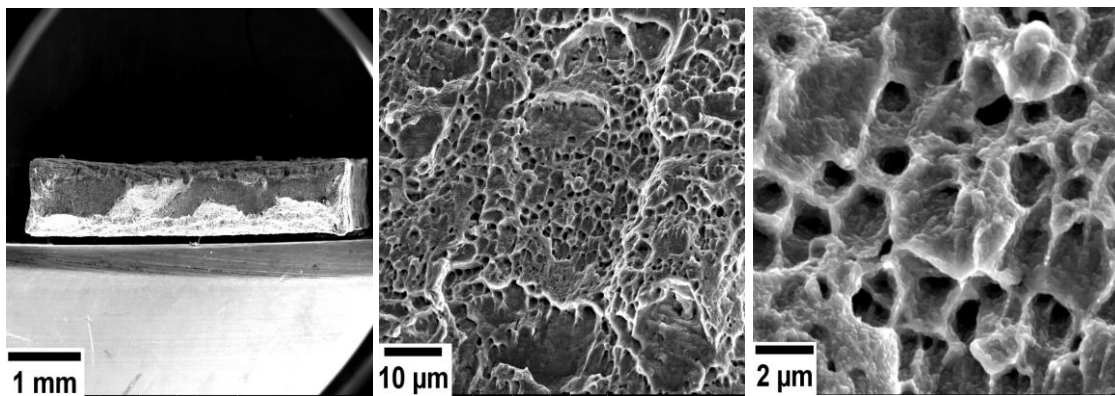
Figure 5.11. Fractured surface of the crept specimen at 1023 and 200 MPa showing ductile fracture characterized by the presence of dimples with little cavitation.

5.4. Discussion

5.4.1. The rate controlling creep mechanism in the Alloy 709

The values of the apparent stress exponent ($\overline{n_a} = 6.8 \pm 0.4$) and the activation energy for creep ($\overline{Q_a} = 421 \pm 38$ kJ/mole) for the Alloy 709 are consistent with those reported for various austenitic stainless steels [12, 13, 16]. For example, an activation energy of 434 kJ/mole has been reported in the temperature range from 898 – 1098 K where both solid solution of Nb, as well as fine NbC precipitates contributed to the creep strength [13]. Apparent

stress exponents and activation energies along with suggested creep mechanisms for various austenitic stainless steels obtained from published literature are compiled in Table 5.3 [11-18]. Since many factors can influence the precipitation behavior and the microstructures, it is not surprising that dramatic differences in creep properties of austenitic stainless steels have been reported.

Table 5.3. Apparent stress exponents and activation energies along with suggested creep mechanisms for various austenitic stainless steels from published literature [11-18].

Material	Range of stresses (MPa)	Range of temperature (K)	Apparent stress exponent, n_a	Apparent activation energy, Q_a (kJ/mole)	Suggested creep mechanism	Ref.
Type 304SS	55 – 240	823 – 923	5.6 – 6.5	334 – 385	Glide-recovery creep	[11]
Fe-15Cr-25Ni-0.086C	15 – 100	1123 – 1223	7	449	Combined matrix/boundary strengthening by carbide	[12]
AISI 347	50 – 196	898 – 1098	8.8	434	Dislocation climb over Nb-rich particles	[13]
Fe–Ni–Cr–Al	150 – 500	823 – 923	6 – 12	165 - 282	Low temperature dislocation climb	[14]
AL6XN	120 – 260	923 – 1023	5.8 – 7.4	380 – 415	Viscous dislocation glide	[15]
Super 304H	120 – 250	923 – 1073	6 – 6.8	460 – 485	Various strengthening particles MX-Z-phase and Cu precipitates	[16]
304H	190 – 210	923 – 1023	16– 27	602 – 769	Dislocation climb over the Cu-rich precipitates	[17]
Alloy 709	100 – 250	923 – 1023	9.9 – 10.8	368	Dislocation climb	[18]
Alloy 709	40 – 275	973 – 1073	6.4 – 7.1	385 – 461	Dislocation climb	This study

In general, n_a and Q_a values obtained from the dependence of the minimum creep rate

on the applied stress and temperature (equation 5.1) are indicative parameters to deduce the

rate controlling creep mechanism(s). For instance, viscous glide process is the rate controlling creep deformation when $n_a = 3 – 3.5$ and the activation energy being close to that of the solute diffusion; however, the dislocation climb process becomes the rate controlling mechanism with higher values of n_a ranging from $5 – 7$ and an activation energy close to that of the lattice self-diffusion [28-30]. In precipitation hardened alloys, however, higher stress exponents and high values of the activation energy compared to the lattice diffusion have been usually reported and attributed to the retarding effect of particles on recovery during high temperature creep [16, 17, 19, 31-33]. This retardation effect is manifested in the form of a threshold stress (σ_{th}) originating from the stress imparted on the dislocations by the precipitates during glide and climb processes. Values as high as 27 for stress exponent and 770 kJ/mole for activation energy have been reported in 304 austenitic steel alloyed with Cu and Nb [17].

Although, the $\overline{n_a}$ value of 6.8 in this study of the Alloy 709 lies within the power-law creep regime, the activation energy of 421 ± 38 kJ/mole being significantly higher than that for self-diffusion for iron in Fe-20Cr-25Ni austenitic steel (284 kJ/mole) [34] makes it difficult to elucidate the true deformation mechanism. In addition, the microstructures of crept samples revealed evidence for dislocation-precipitate interactions suggesting the effects of precipitates on the creep mechanism and putting forward the existence of the "threshold stress" for the Alloy 709. The precipitates are considered to inhibit the recovery process thereby reducing the creep rate. Thus, the creep behavior is interpreted by incorporating a threshold stress produced by the particles and thus, equation 5.1 is modified as

$$\dot{\varepsilon}_m = A''\left(\sigma - \sigma_{th}\right)^n \exp(-\frac{Q}{RT}) \tag{5.4}$$

where n and Q are the true stress exponent and true activation energy for creep respectively and A'' a constant. In equation 5.4, therefore, the effective stress, $\sigma_{eff} = \sigma - \sigma_{th}$ is responsible

for the creep deformation instead of the applied stress suggesting that the deformation does not occur below σ_{th}.

A linear extrapolation method is commonly employed to estimate the values of the threshold stress at different temperatures [35-37] where a linear plot of $\dot{\varepsilon}_m^{1/n'}$ versus σ is made at a given temperature where n' is an assumed stress exponent value that is varied to cover all possible creep mechanisms. The intercept of the linear extrapolation of data to zero creep rate with the stress axis provides the σ_{th}. The choice of true stress exponent value, n must satisfy the best correlation coefficient of the linear fit as well as the corresponding activation energy for a given creep mechanism. The linear extrapolation plots of the $\dot{\varepsilon}_m^{1/n'}$ versus the σ for $n' = 3$ and $n' = 5$ are shown in Figure 5.12a and Figure 5.12b corresponding to viscous glide and dislocation climb controlled mechanisms respectively.

The corresponding threshold stresses are then utilized to calculate the true stress exponent and activation energy for the high temperature deformation. The values of the obtained threshold stresses, average correlation coefficients for the best linear fits (R^2) and average activation energies are summarized in **Error! Not a valid bookmark self-reference.** for assumed stress exponent with n' varied from $3 – 7$ at different temperatures. The calculated activation energy for viscous glide creep mechanism ($n' = 3$) of 190.2 ± 26 kJ/mole was found to be less than that of substitutional solute diffusivities such as Cr, Ni, Mn and Nb which were measured in Fe-20Cr-25Ni-Nb steel using radiotracer techniques to be about 246, 282, 247 and 268 kJ/mole respectively [38-40]. Interstitial solute atoms are not expected to produce significant dislocation pining at the test temperatures as suggested by investigating the serrated flow behavior in this alloy during tensile deformation [26]. Further, the correlation coefficient

133

R^2 has relatively lower values at $n' = 3$ and therefore, this mechanism was excluded from further consideration. For $n' = 7$, the expected creep mechanism is a dislocation climb process either through lattice diffusion or dislocation core diffusion [41].

Table 5.4. Threshold stress analysis for the Alloy 709.

Assumed stress exponent, n'	Temperature (K)	Threshold stress (MPa)	Avg. correlation coefficient, R^2 (%)	Obtained stress exponent (Avg.)	Avg. activation energy, (kJ/mole)
3	973	90.2 ± 16.9	97.32	2.8 ± 0.5	190.2 ± 26
	1023	69.4 ± 15.2			
	1073	48.2 ± 15.5			
4	973	66.7 ± 11.1	98.36	3.6 ± 0.3	248.2 ± 21
	1023	51.9 ± 6.7			
	1073	33.0 ± 6.6			
5	973	42.7 ± 10.2	99.51	4.9 ± 0.2	299.3 ± 15
	1023	33.6 ± 2.4			
	1073	17.2 ± 1.9			
6	973	18.5 ± 10.4	99.49	6.2 ± 0.2	332.9 ± 6
	1023	14.8 ± 3.1			
	1073	1.1 ± 3.4			
7	973	5.9 ± 22.3	99.17	6.4 ± 0.8	431.1 ± 51
	1023	4.4 ± 13.3			
	1073	5.3 ± 35.6			

However, the activation energy was calculated to be about 431 kJ/mole which is higher than that of the lattice self-diffusion, and is considerably higher than that of the dislocation core diffusion of 155 kJ/mole in Fe-20Cr-25Ni steel [34]. The stress exponent of 5 is mainly considered due to the high average value of R^2, and more importantly the estimated activation energy of 299 ± 15 is consistent with that of the lattice diffusivity of iron in Fe-20Cr-25Ni steel [34]. Thus, the threshold stresses in the Alloy 709 are estimated to be 42.7 ± 10.2, 33.6 ± 2.4 and 17.2 ± 1.9 MPa at temperatures 973, 1023 and 1073 K respectively where a decrease of threshold stress with temperature is noted. Log-log plot of the $\dot{\varepsilon}_m$ versus σ_{eff} at various

temperatures and semilog plot of the $\dot{\varepsilon}_m$ versus the reciprocal temperature at various σ_{eff} for the Alloy 709 are included in Figure 5.13a and Figure 5.13b respectively. The true stress exponent is obtained to vary from 4.8 – 5.1 with an average value of 4.9 ± 0.2 and true activation energy of 285 – 315 kJ/mole with an average value of 299 ± 15 kJ/mole. The validity of the obtained values for the threshold stress, true stress exponent, and true activation energy were then verified by establishing the creep constitutive equation for the Alloy 709 using the modified Bird–Mukherjee–Dorn (BMD) equation given by [31]

$$\frac{\dot{\varepsilon}_m kT}{DEb} = A_o \left(\frac{\sigma - \sigma_{th}}{E} \right)^n \tag{5.5}$$

where D is the lattice diffusivity, E the modulus of elasticity, b the Burgers vector (2.58×10^{-8} cm), k the Boltzmann constant and A_o a dimensionless constant. The lattice diffusivity is given by $D_o \exp\left(\frac{-Q}{RT} \right)$ where D_o is the frequency factor taken to be 1.74 cm^2/s [24] and Q is the true activation energy for creep. The values of E at various temperatures for the Alloy 709 have been obtained as $E = 6895(28.73 - 0.01T)$ where the temperature, T is in °C and E in MPa for a Fe-20Cr-25Ni-Nb stabilized austenitic steel [42]. A plot of the diffusion compensated creep rate, $\frac{\dot{\varepsilon}_m kT}{DEb}$ versus the modulus-compensated effective stress, $\frac{\sigma - \sigma_{th}}{E}$ shown in Figure 5.14 demonstrates that the data at various temperature best represented by a straight line with a slope of $n \sim 5$. Further, the obtained constant value of $A_o = 2.4 \times 10^6$ is in close agreement with the value expected when dislocation climb is the operative creep mechanism [43-46]. Hence, the rate-controlling mechanism in the Alloy 709 at the examined stresses and temperatures is determined to be the high temperature climb of edge dislocations.
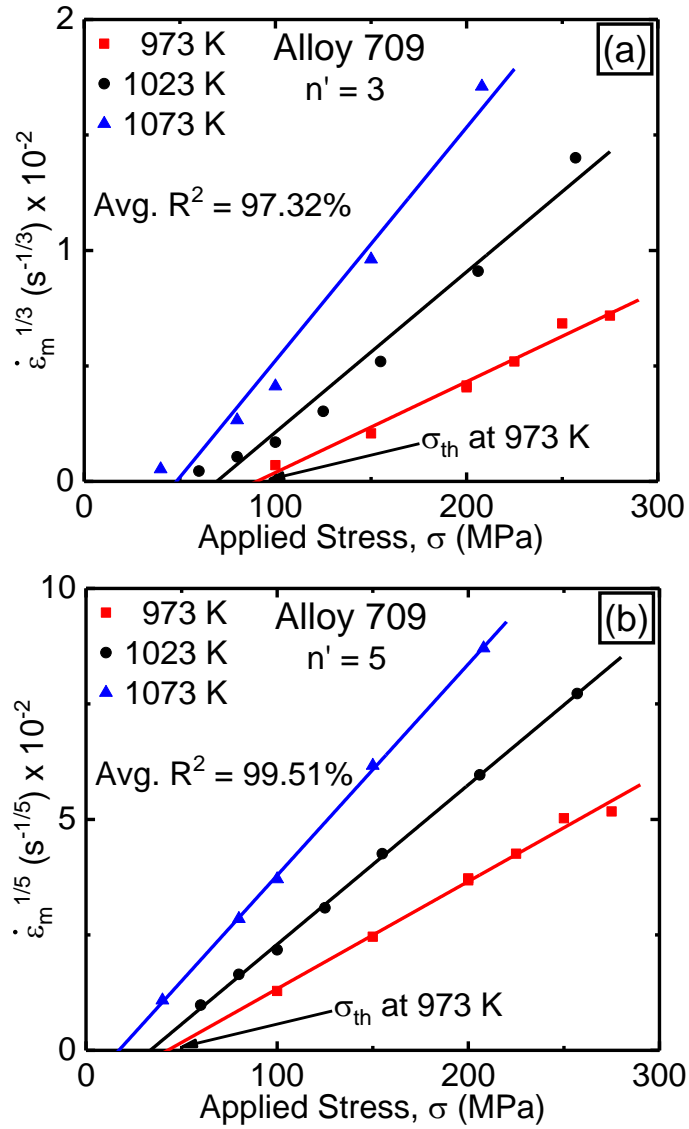
Figure 5.12. The calculation of the threshold stresses at different temperatures in the Alloy 709 for assumed creep deformation mechanism of (a) viscous glide mechanism ($n' = 3$) and (b) dislocation climb controlled mechanism ($n' = 5$).

Figure 5.13. Log-log plot of the minimum creep rate versus effective stress at various temperatures for the Alloy 709. (b) Semilog plot of the $\dot{\varepsilon}_m$ versus the reciprocal temperature at various effective stresses.

Figure 5.14. A log-log plot of diffusion compensated creep rate versus modulus compensated effective stress for the Alloy 709 exhibiting that the data at various temperatures coalesce to a straight line with a slope of n ~ 5.

5.4.2. Microstructures of the crept samples
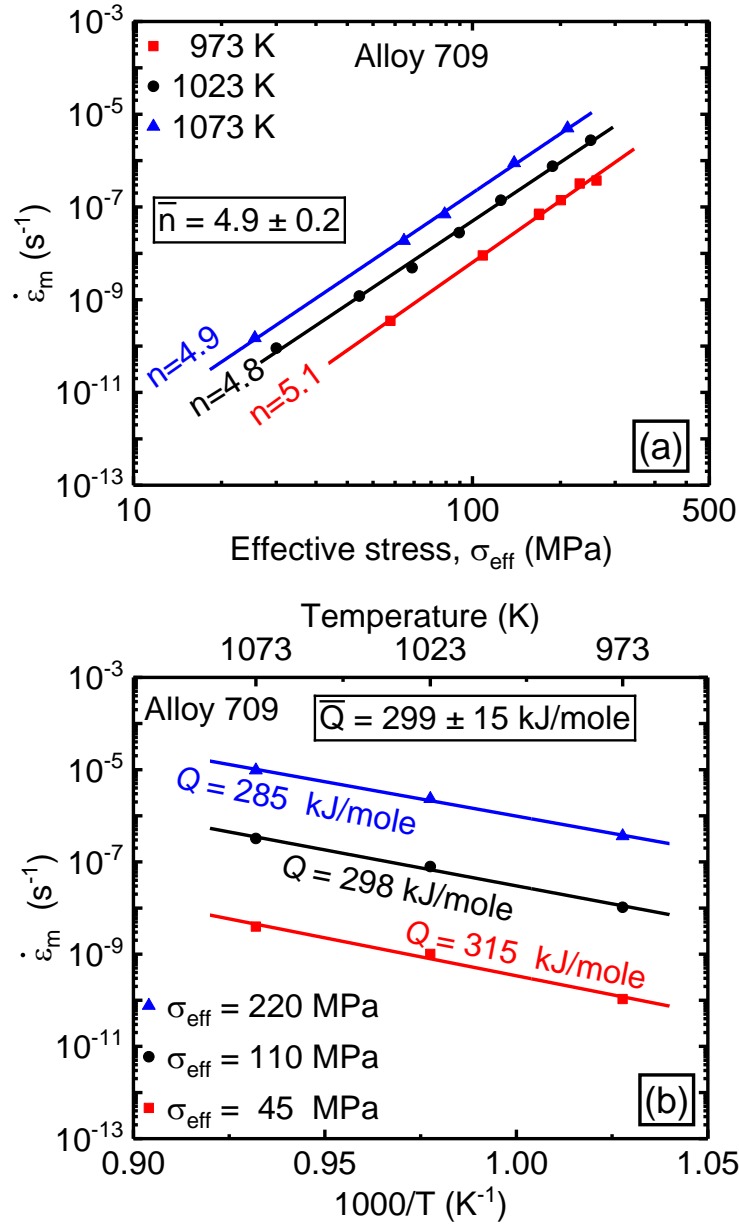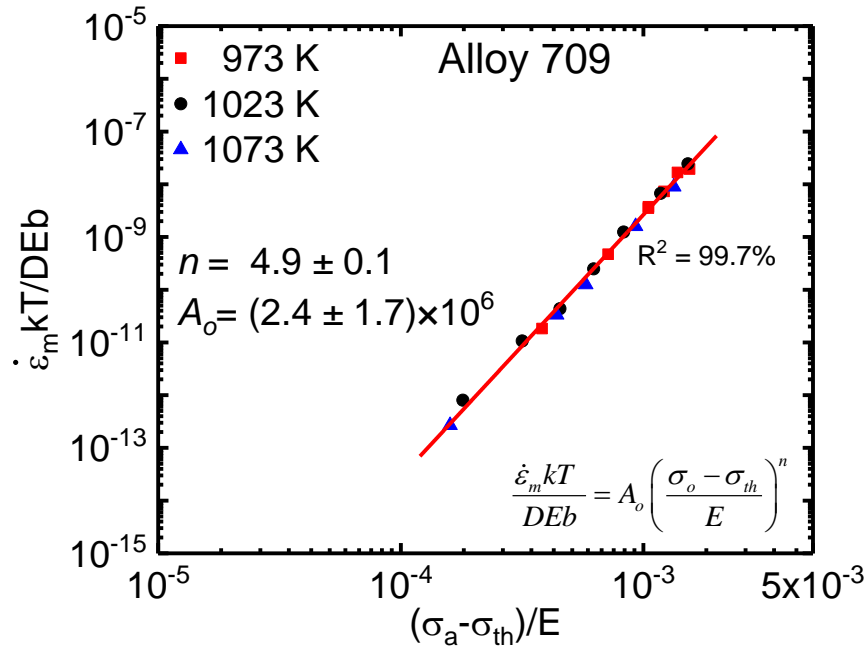
High temperature creep strength in Nb-containing austenitic stainless steels is believed to arise from the fine-scale precipitation in the matrix together with a strengthening of the grain boundaries with grain boundary carbides [12, 13, 20, 47-53]. A small addition of niobium to the AISI 316LN steel resulted in a significant reduction of the minimum creep rate due to Z-phase precipitation [8]. Various precipitates, Nb(C, N), $M_{23}C_6$, and Z-phase observed in this investigation during high temperature creep tests are consistent with those reported for Nb-containing austenitic stainless steels [49, 50, 52, 53] where the restriction of dislocation mobility by fine-scale particles occurs during dislocation creep. Since the precipitation strengthening is inversely proportional to the mean particle spacing, the Nb(C, N) carbonitrides and Z-phases are suggested to be the most predominant strengthening particles in the Alloy 709. The $M_{23}C_6$ precipitates are coarsened very rapidly in the matrix and thus a reduction of its precipitation strengthening is expected. However, extensive $M_{23}C_6$ particles observed at the

138

grain boundaries may contribute to the overall creep strengthening by providing resistance to grain boundary sliding [12, 47, 48].

The presence of subgrain boundary formation in crept specimens shown in Figure 5.10a corroborates the operation of a mechanism controlled by dislocation climb in the Alloy 709. Subgrain formation has been commonly considered as microstructural evidence for the creep due to climb of edge dislocations for various alloys [37, 45, 46, 54]. According to Weertman model [43], edge dislocation dipoles are formed due to the intersections of dislocations originating from different sources of a given density and these dipoles are annihilated towards each other by dislocation climb assisted by lattice diffusion to form low-energy boundaries resulting in subgrain formation.

5.4.3. Creep rupture properties of the Alloy 709

Numerous empirical formulae have been utilized to extrapolate rupture life data. In this study, MGR and LMP are utilized. The validity of the MGR has been demonstrated in a series of single-phase metals as well as precipitation hardened alloys where the constant α is ~ 1 and C_{MG} ranging between 0.05 and 0.5 [55]. The low value of 0.043 ± 0.043 ± 0.005 for the constant C_{MG} observed in the Alloy 709 indicates that the creep strain accumulated during secondary creep rate is relativity smaller than that in tertiary creep regime. Tertiary creep manifested in increased creep rates eventually resulting in failure and is related to the growth of creep damage. It was demonstrated that a modified-MGR by the creep strain to failure gives a better measure of creep ductility [56],

$$\dot{\varepsilon}_m^{\alpha'} \frac{t_f}{\varepsilon_f} = C_{MMG} \tag{5.6}$$

where α' and C_{MMG} are modified-MGR constants. Figure 5.15 shows the log-log plot of the

139

$\dfrac{t_f}{\varepsilon_f}$ as a function of the $\dot{\varepsilon}_m$ for the Alloy 709. A value close to 1 for α' using the best liner fit

exhibits the validity of the modified-Monkman-Grant relation while the C_{MMG} is found to be

0.20 ± 0.08. The inverse of the C_{MMG} is called the creep damage tolerance parameter, λ which

is used as a measure to identify the creep rupture mode. The value of λ ranges from 1 to 20

for engineering alloys depicting the range from brittle fracture mode for materials having low

creep strain without significant plastic deformation to ductile materials that can withstand

strain concentration without local cracking [57]. In 15Ni-14Cr and 316 austenitic stainless

steels, values of 2.5 and 4 were reported, and fracture modes were attributed to the occurrence

of intergranular cavitation and necking respectively. In general, tertiary creep is caused by

intergranular cavitation and the damage is mainly accumulated due to cavity growth when λ

lies in the range of $1 - 2.5$, while fracture is attributed to precipitate coarsening and

microstructural instability for the value of $\lambda > 5$ [58]. A value of λ between 2.5 and 5 is

correlated with necking [58]. In this investigation, the Alloy 709 exhibited a value of $\lambda \sim 5$

suggesting the contribution of necking to the fracture in the tertiary creep. This conclusion is

correlated well by the presence of dimples in the fracture surface of the ruptured sample, which

is reminiscent of ductile fracture during uniaxial tensile testing after necking.
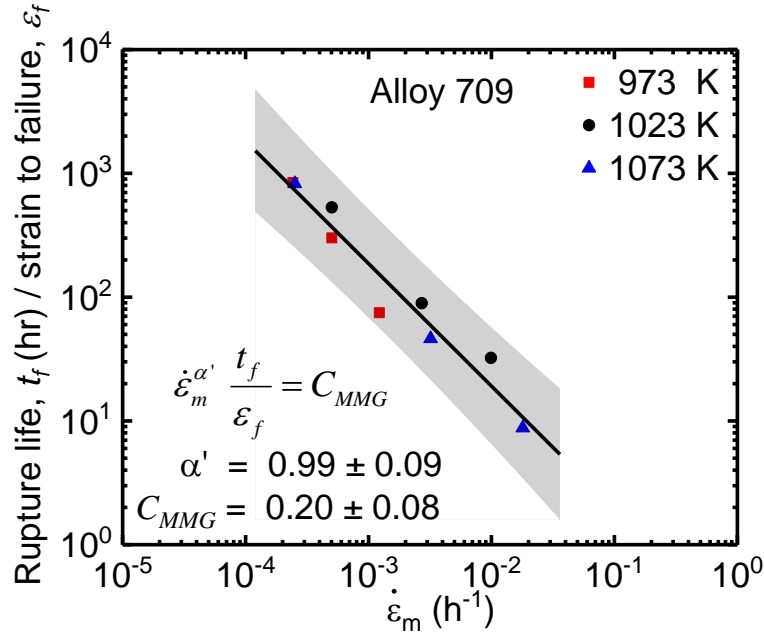
Figure 5.15. The validity of the modified-Monkman-Grant relation in the Alloy 709.
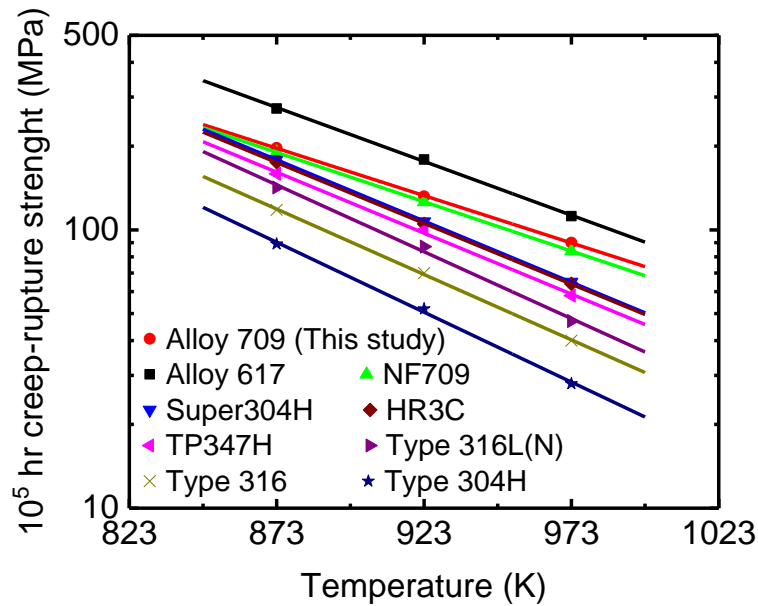
Figure 5.16. 10^5-hour creep-rupture strength estimated from LMP as a function of temperature for the Alloy 709 (Red-circle data). The values for other advanced austenitic stainless steels and the Ni-based Alloy 617 obtained from ECCC data sheets [59] are included for comparison. It is seen that the Alloy 709 exhibits superior creep strengths relative to the other advanced austenitic steels.

Another way of presenting creep rupture data for creep life prediction was also employed through Larson–Miller parameter (LMP) as shown in Figure 5.7b. The LMP was

used to estimate the 10^5-hour creep-rupture strength for the Alloy 709 and Figure 5.16 shows the 10^5-hour creep-rupture strength estimated from LMP as a function of temperature for the Alloy 709 in comparison to other advanced austenitic stainless steels; the Ni-based Alloy 617 obtained from ECCC data sheets [48]. It is clearly seen that the Alloy 709 exhibited superior creep strengths relative to the other advanced austenitic steels, and the data are very close to those obtained in the NF709 steel. Nevertheless, the knowledge of such microstructural instabilities and the performance of longer creep rapture tests are needed to confirm this conclusion since short-term creep tests may lead to significant errors in the extrapolation of the data to far longer times.

5.5. Conclusion

Constant load uniaxial creep tests have been conducted at temperatures ranging from 973 – 1073 K and initial stresses 40 – 275 MPa for a Fe-20Cr-25Ni (mass pct) austenitic stainless steel (Alloy 709), a candidate structural material for Sodium-cooled Fast Reactors. At high stresses (>100 MPa), creep rupture tests were conducted while interrupted testes in the secondary creep regime were carried out at lower stresses. The following conclusions are made:

1. The dependence of the minimum creep rate on the applied stress was found to follow the power-law creep with the apparent stress exponent values ranging between 6.4 – 7.1 with an average value of 6.8 ± 0.4. The apparent activation energy was found to be 385 – 461 kJ/mole with an average value of 421 ± 38 kJ/mole which is relatively high compared to that of lattice self-diffusion of iron in Fe-20Cr-25Ni steel.

2. The presence of dislocation-precipitate interactions in the crept samples together with the observed high value of activation energy for creep suggested the existence of threshold

stresses in the Alloy 709 which were estimated using the linear extrapolation method to be 42.7 ± 10.2 MPa, 33.6 ± 2.4 MPa and 17.2 ± 1.9 MPa at 973 K, 1023 K and 1073 K respectively.

3. As a result of the threshold stress modification, the true stress exponent and the true activation energy were found to be 4.9 ± 0.2 and 299 ± 15 kJ/mole, respectively. Hence, the rate-controlling mechanism in the Alloy 709 at the examined stresses and temperatures was conclusively determined to be the high temperature climb of edge dislocations.

4. Three types of precipitates were identified in the crept samples, namely Nb(C, N), and Z-phases of sizes between $20 - 200$nm within the matrix and $M_{23}C_6$ with sizes between 200 $- 700$ nm within the matrix and at grain boundaries. Further, the microstructures of the crept samples showed evidence for the formation of subgrain boundaries as well as dislocation-precipitate interactions.

5. The analysis of creep rupture data indicated that the Alloy 709 obeys Monkman–Grant and modified Monkman–Grant relationships and displays a high creep damage tolerance factor of ~ 5 suggesting the contribution of necking to the fracture in the tertiary creep. This conclusion was also correlated well by observing dimples on the fracture surface of the ruptured samples.

6. The Larson-Miller parameter was employed to estimates the 10^5-hour creep-rupture strength in this study and the Alloy 709 exhibited superior creep strengths relative to other advanced austenitic steels.

5.6. References

[1] T.R. Allen, K. Sridharan, L. Tan, W.E. Windes, J.I. Cole, D.C. Crawford, G.S. Was, Materials Challenges for Generation IV Nuclear Energy Systems, Nucl. Technol. 162(3) (2008) 342-357.

143

[2] K.L. Murty, I. Charit, Structural materials for Gen-IV nuclear reactors: Challenges and opportunities, J. Nucl. Mater. 383 (2008) 189-195.

[3] J.T. Busby, Economic benefits of advanced materials in nuclear power systems, J. Nucl. Mater. 392(2) (2009) 301-306.

[4] S.L.Mannan, S.C.Chetal, B. Raj, S.B.Bhoje, Selection of Materials For Prototype Fast Breeder Reactor, Transactions- Indian Institute of Metals 56 (2003) 1-35.

[5] J.D. Cook, D.R. Harries, A.C. Roberts, Some factors affecting the creep strength of 20%Cr-25%Ni-Nb austenitic steel at 750 °C, Creep Strength in Steels and High Temperature alloys, The Metals Society, London, 1972, p. 91.

[6] W. Corwin, Advanced Structural Materials (RC-3), Nuclear Energy University Programs (NEUP), Fiscal Year (FY) 2015 Annual Planning Webinar, DOE, 2014.

[7] T.-L. Sham, L. Tan, Y. Yamamoto, Development of Advanced 9Cr Ferritic-Martensitic Steels and Austenitic Stainless Steels for Sodium-Cooled Fast Reactors, Fast Reactors and Related Fuel Cycles: Safe Technologies and Sustainable Scenarios (FR13), IAEA, Vienna, 2015, pp. 1-9.

[8] T. Takahashi, M. Sakakibara, M. Kikuchi, T. Ogawa, H. Sakurai, S. Araki, K. Nagao, H. Yasuda, Development of High-Strength 20Cr-25Ni (NF709) Steel for USC Boiler Tubes,, Nippon Steel Corporation, 1988.

[9] H.E. Evans, D.A. Hilton, Structure and properties of nitrided stainless steel fuel cladding for use in advanced gas-cooled reactors, Nucl. Energy 18 (1973) 33-38.

[10] G. Knowles, The creep strenghth of a 20%Cr-25%Ni-Nb steel containing controlled particle dipersion, Met. Sci. 11 (1977) 117-122.

[11] O.K. Chopra, K. Natesan, Interpretation of high-temperature creep of type 304 stainless steel, Metall. Trans. A 8(4) (1977) 633-638.

[12] J.S. Zhang, P.E. Li, J.Z. Jin, Combined matrix/boundary precipitation strengthening in creep of Fe-15 Cr-25 Ni alloys, Acta Metall. Mater. 39(12) (1991) 3063-3070.

[13] E. Evangelista, C. Guardamagna, L. Kloc, A. Rosen, S. Spigarelli, The Role of Cold Working in the Creep Deformation of Nb Stabilized Stainless Steel. I. Creep Results and Microstructural Evolution, High Temp. Mater. Processes 14 (1995) 151-161.

[14] D.V.V. Satyanarayana, G. Malakondaiah, D.S. Sarma, Steady state creep behaviour of NiAl hardened austenitic steel, Mater. Sci. Eng., A 323(1) (2002) 119-128.

[15] L.J. Meng, J. Sun, H. Xing, Creep and precipitation behaviors of AL6XN austenitic steel at elevated temperatures, J. Nucl. Mater. 427(1) (2012) 116-120.

144

[16] D.-B. Park, S.-M. Hong, K.-H. Lee, M.-Y. Huh, J.-Y. Suh, S.-C. Lee, W.-S. Jung, High-temperature creep behavior and microstructural evolution of an 18Cr9Ni3CuNbVN austenitic stainless steel, Mater. Charact. 93 (2014) 52-61.

[17] P. Ou, L. Li, X.-F. Xie, J. Sun, Steady-State Creep Behavior of Super304H Austenitic Steelat Elevated Temperatures, Acta Metall. Sin. (Engl. Lett.) 28 (2015) 1336–1343.

[18] A.S. Alomari, N. Kumar, K.L. Murty, Investigation on Creep Mechanisms of Alloy 709, Proceedings of the ASME 2017 Power and Engineering Conference, Charlotte, NC, USA, 2017.

[19] J.K. Benz, L.J. Carroll, J.K. Wright, R.N. Wright, T.M. Lillo, Threshold Stress Creep Behavior of Alloy 617 at Intermediate Temperatures, Metall. Trans. A 45 (2014) 3010-3022.

[20] T. Sourmail, H.K.D.H. Bhadeshia, Microstructural evolution in two variants of NF709 at 1023 and 1073 K, Metall. Trans. A 36 (2005) 23-34.

[21] B.K. Kim, L. Tan, C. Xu, Y. Yang, X. Zhang, M. Li, Microstructural evolution of NF709 (20Cr–25Ni–1.5MoNbTiN) under neutron irradiation, J. Nucl. Mater. 470 (2016) 229-235.

[22] C. Degueldre, J. Fahy, O. Kolosov, R.J. Wilbraham, M. Döbeli, N. Renevier, J. Ball, S. Ritter, Mechanical Properties of Advanced Gas-Cooled Reactor Stainless Steel Cladding After Irradiation, J. Mater. Eng. Perform. 27(5) (2018) 2081-2088.

[23] T. Chen, L. Tan, Z. Lu, H. Xu, The effect of grain orientation on nanoindentation behavior of model austenitic alloy Fe-20Cr-25Ni, Acta Mater. 138 (2017) 83-91.

[24] D.S. Smith, N.J. Lybeck, J.K. Wright, R.N. Wright, Thermophysical properties of Alloy 709, Nucl. Eng. Des. 322 (2017) 331-335.

[25] A.S. Alomari, N. Kumar, K.L. Murty, Enhanced ductility in dynamic strain aging regime in a Fe-25Ni-20Cr austenitic stainless steel, Mater. Sci. Eng., A 729 (2018) 157-160.

[26] A.S. Alomari, N. Kumar, K.L. Murty, Serrated plastic deformation behavior in Alloy 709, International Congress on Advances in Nuclear Power Plants (ICAPP), American Nuclear Society, Charlotte, NC, USA, 2018.

[27] S. Upadhayay, H. Li, P. Bowen, A. Rabiei, A study on tensile properties of Alloy 709 at various temperatures, Mater. Sci. Eng., A 733 (2018) 338-349.

[28] K.L. Murty, F.A. Mohamed, J.E. Dorn, Viscous glide, dislocation climb and newtonian viscous deformation mechanisms of high temperature creep in Al-3Mg, Acta Metall. 20 (1972) 1009-1018.

[29] T.G. Langdon, Dislocation and Creep, Dislocations and properties of real materials, The Institute of Metals, London, 1985, pp. 221-238.

[30] K.L. Murty, G. Dentel, J. Britt, Effect of temperature on transitions in creep mechanisms in class-A alloys, Mater. Sci. Eng., A 410-411 (2005) 28-31.

[31] J. Bird, A. Mukherjee, J. Dorn, Correlation Between High Temperture Creep Behavior and Structure Quantitative Relations between Properties and Microstructure, Israel Univ, 1969.

[32] S. Latha, M.D. Mathew, P. Parameswaran, K. Bhanu Sankara Rao, S.L. Mannan, Thermal creep properties of alloy D9 stainless steel and 316 stainless steel fuel clad tubes, Int. J. Press. Vessels Pip. 85(12) (2008) 866-870.

[33] S. Latha, M.D. Mathew, P. Parameswaran, K. Bhanu Sankara Rao, S.L. Mannan, Creep behaviour of 14Cr–15Ni–Ti stainless steel at 923K, Mater. Sci. Eng., A 527 (2010) 5167-5174.

[34] A.F. Smith, G.B. Gibbs, The Volume and Grain-Boundary Diffusion of Iron in 20 Cr/25 Ni/Nb Stainless Steel, Met. Sci. J. 2 (1968) 47-50.

[35] R. Lagneborg, B. Bergman, The stress/creep rate behaviour of precipitation-hardened alloys, Met. Sci. 10(1) (1976) 20-28.

[36] R.S. Mishra, T.R. Bieler, A.K. Mukherjee, Superplasticity in powder metallurgy aluminum alloys and composites, Acta Metall. Mater. 43(3) (1995) 877-891.

[37] T. Shrestha, M. Basirat, I. Charit, G.P. Potirniche, K.K. Rink, U. Sahaym, Creep deformation mechanisms in modified 9Cr–1Mo steel, J. Nucl. Mater. 423(1) (2012) 110-119.

[38] A.F. Smith, G.B. Gibbs, Volume and Grain-Boundary Diffusion in 20 Cr/25 Ni/Nb Stainless Steel, Met. Sci. J. 3 (1969) 93-94.

[39] A.F. Smith, The diffusion of niobium in 20/25 Nb stainless steel, Central Electricity Generating Board, United Kingdom, 1972.

[40] A.F. Smith, The lattice and grain boundary diffusion of manganese in 20/25/Nb stainless steel, Zeitschrift für Metallkunde 66 (1975) 692-696.

[41] S.L. Robinson, O.D. Sherby, Mechanical behavior of polycrystalline tungsten at elevated temperature, Acta Metall. 17(2) (1969) 109-125.

[42] E.G. Wilson, Stress varied creep of 20%Cr-25%Ni-Nb stabilized austenitc stainless steel, Creep strength in steel and high temperature alloys, The Metal Society, London, 1972, pp. 111-121.

[43] J. Weertman, High temperature creep produced by dislocation motion, in: A.K. Mukherjee, J.C.M. Li (Eds.), Rate Processes in Plastic Deformation of Materials, ASM, Cleveland, Ohio, USA, 1972, pp. 315–336.

146

[44] K.L. Murty, Transitions in deformation mechanisms in class-a alloys -historical perspective & recent applications to microelectronic solders and nuclear core materials, in: J.C. Earthman, F.A. Mohamed (Eds.) Creep and fracture of engineering materials and structures, The Minerals, Metals & Materials Society, Irvine, USA, 1997, pp. 69-78.

[45] S. Gollapudi, I. Charit, K.L. Murty, Creep mechanisms in Ti–3Al–2.5V alloy tubing deformed under closed-end internal gas pressurization, Acta Mater. 56(10) (2008) 2406-2419.

[46] B. Kombaiah, K.L. Murty, Coble, Orowan Strengthening, and Dislocation Climb Mechanisms in a Nb-Modified Zircaloy Cladding, Metall. Trans. A 46(10) (2015) 4646-4660.

[47] A. Horsewell, Creep inhibition at grain boundaries in a stainless steel, Metall. Trans. A 9(12) (1978) 1843-1847.

[48] M.D. Mathew, G. Sasikala, K. Bhanu Sankara Rao, S.L. Mannan, Influence of carbon and nitrogen on the creep properties of type 316 stainless steel at 873 K, Mater. Sci. Eng., A 148(2) (1991) 253-260.

[49] N.D. Evans, P.J. Maziasz, J.P. Shingledecker, M.J. Pollard, Structure and Composition of Nanometer-Sized Nitrides in a Creep-Resistant Cast Austenitic Alloy, Metall. Trans. A 41(12) (2010) 3032-3041.

[50] B. Peng, H. Zhang, J. Hong, J. Gao, H. Zhang, J. Li, Q. Wang, The evolution of precipitates of 22Cr–25Ni–Mo–Nb–N heat-resistant austenitic steel in long-term creep, Mater. Sci. Eng., A 527(16) (2010) 4424-4430.

[51] V. Vodárek, Creep behaviour and microstructural evolution in AISI 316LN+Nb steels at 650°C, Mater. Sci. Eng., A 528(12) (2011) 4232-4238.

[52] Y. Zhou, Y. Li, Y. Liu, Q. Guo, C. Liu, L. Yu, C. Li, H. Li, Precipitation behavior of type 347H heat-resistant austenitic steel during long-term high-temperature aging, J. Mater. Res. 30(23) (2015) 3642-3652.

[53] Z. Zhang, Z. Hu, H. Tu, S. Schmauder, G. Wu, Microstructure evolution in HR3C austenitic steel during long-term creep at 650°C, Mater. Sci. Eng., A 681 (2017) 74-84.

[54] H.J. Kestenbach, T. Luiz Da Silvelra, S.N. Monteiro, On subgrain formation during creep of 316 stainless steel, Metall. Trans. A 7(1) (1976) 155-158.

[55] E.C.Monkman, N.J.Grant, An empirical relationship between rupture life and minimum creep rate in creep-rupture tests, Proc. Am. Soc. Test. Mater. 56 (1956) 593.

[56] F. Dobeš, K. Milička, The relation between minimum creep rate and time to fracture, Met. Sci. 10 (1976) 382-384.

[57] M.F. Ashby, B.F. Dyson, Creep damage mechanics and micromechanisms, in: S.R.V.e. al. (Ed.), Advances in Fracture Research, Pergamon Press, Oxford, 1984, pp. 3–30.

[58] B. Wilshire, H. Burt, Damage evolution during creep of steels, Int. J. Press. Vessels Pip. 85 (2008) 47-54.

[59] ECCC Data sheets, European Technology Development, 2005.

6. CONCLUSIONS AND FUTURE WORK

Serrated yielding and creep properties have been thoroughly examined in the Fe-20Cr-25Ni (wt.%) advanced austenitic stainless steel (Alloy 709) which is a candidate structural material for Sodium Fast Reactors.

Tensile tests in a wide range of temperatures (298 – 1073 K) and nominal strain rates (10^{-5} – 10^{-3} s^{-1}) followed by microstructural evaluations were carried out to understand the behavior of the serrated yielding resulting from DSA in the Alloy 709. The following conclusions are made:

1. Serrated flow was observed in the stress-strain curves within a specific regime of test temperatures identified as low-temperature serrated-flow regime (LT-SF) at 498 – 623 K and high temperature serrated-flow regime (HT-SF) at 623 – 973 K separated by mild serrations or smooth flow.

2. Types A and A+B serrations were observed in the LT-SF while types A, A+B, A+C and C serrations were obtained in the HT-SF.

3. At a given temperature, the critical strain, ε_c was found to decrease with a decrease in strain rate with slopes corresponding to exponent $m+\beta$ values of 0.78 ± 0.1 and 1.56 ± 0.2 for the LT-SF and HT-SF regimes respectively.

4. The activation energy, Q, for the onset of the serrated flow was evaluated using different methods and the average Q-values were found to be 103 ± 13 kJ/mole and 204 ± 11 kJ/mole respectively for the LT-SF and HT-SF.

5. Based on the activation energy values, the dependence of the critical strain on strain rate and the literature survey, diffusion of interstitial atoms such as nitrogen and/or carbon is thought to be responsible for serrations in the LT-SF regime while the diffusion of

substitutional atoms such as chromium is operative in the HT-SF region.

6. The disappearance of serrations at high temperatures accompanied by the observation of type C serrations is thought to be due to the formation of carbide precipitates.

7. Plateaus and peaks in flow stresses, negative strain rate sensitivity, planar substructure and increase in the work-hardening rate were observed and ascribed to the DSA at 498 – 973K.

8. A relatively low fraction of LAGBs in deformed samples at intermediate temperatures where serrated flow occurs is believed to be another manifestation for the occurrence of the DSA.

9. Increase in ductility (total elongation to fracture) was observed in the DSA regime compared to lower temperatures where no serrated flow is noted. This observation is opposite to the commonly reported loss in ductility due to DSA. The beneficial effect of the DSA in the Alloy 709 was attributed to the relatively high work hardening rate and strain hardening exponent resulting in large uniform strain and hence increased overall ductility.

In addition, constant load uniaxial creep tests have been conducted at temperatures ranging from 973 – 1073 K and initial stresses 40 – 275 MPa. At high stresses (>100 MPa), creep rupture tests were conducted while interrupted testes in the secondary creep regime were carried out at lower stresses. The following conclusions are made:

1. The dependence of the minimum creep rate on the applied stress was found to follow the power-law creep with the apparent stress exponent values ranging between 6.4 – 7.1 with an average value of 6.81 ± 0.4. The apparent activation energy was found to be 385 – 461 kJ/mole with an average value of 421 ± 38 kJ/mole which is relatively high compared to that of lattice self-diffusion of iron in Fe-20Cr-25Ni steel.

2. The presence of dislocation-precipitate interactions in the crept samples together with the observed high value of activation energy for creep suggested the existence of threshold stresses in the Alloy 709 which were estimated using the linear extrapolation method to be 42.7 ± 10.2 MPa, 33.6 ± 2.4 MPa and 17.2 ± 1.9 MPa at 973 K, 1023 K and 1073 K respectively.

3. As a result of this threshold stress modification, the true stress exponent and the true activation energy were found to be 4.9 ± 0.2 and 299 ± 15 kJ/mole, respectively. Hence, the rate-controlling mechanism in the Alloy 709 at the examined stresses and temperatures is conclusively determined to be the climb of edge dislocations.

4. Three types of precipitates were identified in the crept samples, namely Nb(C, N), and Z-phases of sizes between $20 - 200$nm within the matrix and $M_{23}C_6$ with sizes between 200 – 700 nm within the matrix and on grain boundaries. Further, the microstructures of the crept samples showed evidence for the formation of subgrain boundaries as well as dislocation-precipitate interactions.

5. The analysis of creep rupture data indicated that the Alloy 709 obeys Monkman–Grant and modified Monkman–Grant relationships and displays a high creep damage tolerance factor of ~ 5 suggesting the contribution of necking to the fracture in the tertiary creep. This conclusion was also correlated well by the observation of excess dimples on the fracture surface of the ruptured samples.

6. Finally, the Larson-Miller parameter was employed to estimates the 10^5-hour creep-rupture strength in this study, and the Alloy 709 exhibited superior creep strengths relative to other advanced austenitic steels. However, longer creep rupture data are needed to confirm this conclusion.

6.1. Future work

- *Fracture toughness in the dynamic strain aging regime for the Alloy 709*

The contrasting view observed in the Alloy 709 regarding the ductility enhancement during DSA regime requires further attention and, specifically, the fracture toughness characteristics. During DSA regime, an increase in the work-hardening exponent, *n* has also been noted in the Alloy 709 where it is assumed to be directly related to the formation of a plastic zone ahead of the crack tip, *r*. Hence, the fracture toughness properties for the Alloy 709 deserve a detailed study to confirm that the DSA can also enhance the ductile initiation fracture toughness. Different methods have been employed to evaluate the fracture toughness parameters and the *J*-Integral property of a material can give a good estimate of its resistance to crack nucleation under elastic-plastic conditions. An attractive method to evaluate the *J*-integral is "the single specimen unloading compliance method" where the crack growth is monitored as a function of the compliance experimentally measured from the loading and unloading tests using a single V-notched compact test (CT) specimen.

- *Effect of prior creep on steady state creep behavior of the Alloy 709*

It is interesting to compare the present results of the Alloy 709 with those obtained from the load change creep test in a previous study [1]. Figure 6.1 shows the log-log plot of the minimum creep rate versus applied stress at 1023 K for the Alloy 709 using constant load creep tests obtained from the current study compared to those obtained from load change creep tests on a single specimen [14]. A higher value of the apparent stress exponent of 10.8 at 1023 K was found from the load change creep tests while a value of 6.9 is found here at the same temperature. Similar behavior in 304SS has been reported by Murty and McDonald [2] and attributed to the history-dependent minimum creep rate, based on the effect of prior creep on

152

the substructure. In a Nb-stabilized austenitic SS AISI347 [3], higher dislocation density in a prior strained sample was found to promote the nucleation of NbC and accordingly increase the creep strength.
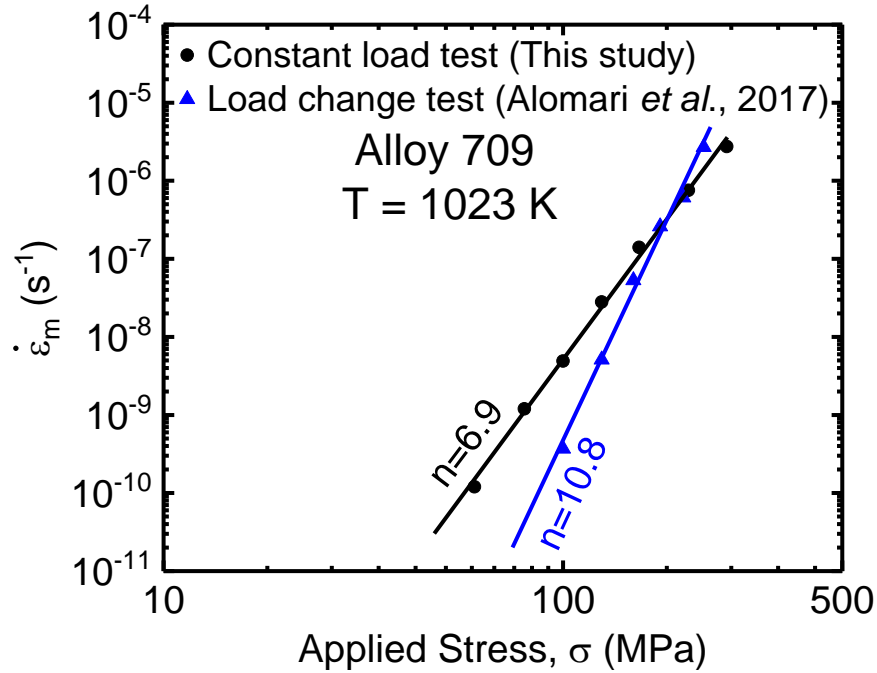

Figure 6.1. Log-log plot of the minimum creep rate versus applied stress at 1023 K for the Alloy 709 using multiple specimens with single load creep tests obtained from the present study and load change creep tests on a single specimen obtained from previous work [1].

The threshold stress was estimated to be about 52 MPa at 1023 K in the Alloy 709 when load change creep test is employed relative to a value of 33.6 MPa in the current study. Although, a higher threshold stress value is obtained from the load change tests, a high temperature climb of the edge dislocation was suggested to be the rate controlling creep mechanism in both. Therefore, a plausible explanation for the history-dependent minimum creep rate observed in the Alloy 709 might be attributed to the effect of prior creep on the threshold stress, A prior creep is found to increase the threshold stress and accordingly enhance the creep strength of the Alloy 709. However, this explanation is only speculative at this time and needs to be further verified.

153

- *Creep-fatigue interaction properties of the Alloy 709*

Creep-fatigue interaction is expected to contribute to the damage mode for many high-temperature components of next-generation nuclear Sodium-Fast Reactors such as reactor vessels and gas turbines. Cyclic loadings originating from the power transients during operation as well as startups and shutdowns lead to degradation of engineering components through fatigue while inherent stress relaxation during steady operation induces creep deformation. Hence; understating the interaction among creep and fatigue degradation mechanisms at high temperatures is essential to determine a component's lifetime and design safety margins. The creep-fatigue deformation behavior is unknown for the Alloy 709. Initial results on evaluating creep-fatigue interaction in the Alloy 709 conducted at 750 °C using triangular waveform following the ASTM standard E2714–13 at 0.1 Hz frequency are presented in the Appendices C and D. However, further studies are needed to carry out creep-fatigue tests at different hold times, strain ranges, and temperatures as well as microstructural characterization of the samples following deformation.

6.2. References

[1] A.S. Alomari, N. Kumar, K.L. Murty, Investigation on Creep Mechanisms of Alloy 709, Proceedings of the ASME 2017 Power and Engineering Conference, Charlotte, NC, USA, 2017.

[2] K.L. Murty, S.G. McDonald, Effect of prior creep on steady state creep behavior of stainless steel type 304, Materials Science and Engineering 55(1) (1982) 105-109.

[3] E. Evangelista, C. Guardamagna, L. Kloc, A. Rosen, S. Spigarelli, The Role of Cold Working in the Creep Deformation of Nb Stabilized Stainless Steel. I. Creep Results and Microstructural Evolution, High Temp. Mater. Processes 14 (1995) 151-161.

ACKNOWLEDGMENTS

APPENDICES

Appendix A
List of selected presentations and publications

Publications:

[1] **A. S. Alomari**, N. Kumar, and K.L. Murty, "Serrated yielding in an advanced stainless steel Fe-25Ni-20Cr (wt. %)," Mater. Sci. Eng., A, 751 (2019) pp. 292–302.

[2] **A. S. Alomari**, N. Kumar, and K.L. Murty, "Creep behavior and microstructural evolution of a Fe-20Cr-25Ni (wt.%) austenitic stainless steel (Alloy 709) at elevated temperatures," Metall. Mater. Trans. A, 50 (2019) pp.641-654.

[3] **A. S. Alomari**, N. Kumar, and K.L. Murty, "Enhanced Ductility in dynamic strain aging regime in a Fe-25Ni-20Cr austenitic stainless steel," Mater. Sci. Eng., A, 729 (2018) pp.157-160.

[4] N. Kumar, **A. S. Alomari** and K.L. Murty, "Understanding thermally activated plastic deformation behavior of Zircaloy-4," J. Nucl. Mater., 504 (2018) pp.41-49.

[5] **A.S. Alomari**, N. Kumar and K.L. Murty, "Investigation on Creep-Fatigue Interaction of Fe-25Ni-20Cr austenitic stainless steel (Alloy 709)," Transactions of the American Nuclear Society, 119, pp. 503-506, June 17-21, 2018, November 11-15, 2018 | Orlando, FL.

[6] N. Kumar, **A. Alomari**, and K.L. Murty, "Understanding creep-fatigue interaction in Fe-25Ni-20Cr (wt.%) austenitic stainless steel," in: Challenges in Mechanics of Time-Dependent Materials, Volume 2, Alex et al. (Eds.), Springer International Publishing (2018) pp.33-38.

[7] **A.S. Alomari**, N. Kumar and K.L. Murty, "Serrated Plastic Deformation Behavior in Alloy 709," in: International Congress on Advances in Nuclear Power Plants (ICAPP 18) Charlotte, NC, April 8-11, 2018, pp.1020-1028.

[8] **A.S. Alomari**, N. Kumar and K.L. Murty, "Investigation on Creep Mechanisms of Alloy 709." ASME Power & Energy/ICOPE-17, Charlotte, NC USA, June 26-30, 2017, Paper No. NUCLRF2017- 3649.

[9] **A.S. Alomari** and A.I. Hawari, "Investigation of Energy Selective Neutron Imaging at the PULSTAR Reactor," Transactions of the American Nuclear Society, 114, p. 345-347, New Orleans, LA, June 12–16, 2016.

Poster/Oral Presentations

[1] **A.S. Alomari**, N. Kumar and K.L. Murty, "High Temperature Deformation Mechanisms in the Alloy 709," Poster Session-NE Graduate Research Symposium, Raleigh, NC, USA, May 2, 2018.

[2] N. Kumar, **A.S. Alomari** and K.L. Murty, "On creep deformation behavior of Nb-containing Fe-Ni-Cr austenitic stainless steel," Material Science and technology MS&T17, Pittsburgh, PA, USA, Oct. 8-12, 2017.

[3] **A.S. Alomari**, N. Kumar and K.L. Murty, "Dynamic Strain Aging in Alloy 709," Poster Session-Triangle Student Research Competition, Research Triangle, Durham, NC, USA, Oct. 4, 2017.

[4] **A.S. Alomari** and K.L. Murty, "Serrated Yielding in Austenitic Stainless Steel," Nuclear engineering research seminar at NCSU, Raleigh, NC, USA, Aug. 17, 2017.

[5**] A.S. Alomari**, N. Kumar and K.L. Murty, "Steady State Creep Behavior of Alloy 709," Poster Session-NE Graduate Research Symposium, Raleigh, NC, USA, Apr. 27, 2017.

[6] **A.S. Alomari**, N. Kumar and K.L. Murty, "Investigation on Creep Properties of Alloy 709 (Fe-25Ni-20Cr) at 1023 K," TMS 2018 Annual Meeting, Phoenix, AR, USA, Mar. 11-15, 2017.

[7] **A.S. Alomari**, N. Kumar and K.L. Murty, "High Temperature Deformation Mechanisms of Austenitic Stainless Steel Alloy 709," The 12th Annual NC State University Graduate Student Research Symposium, Raleigh, NC, USA, Mar. 22, 2017.

Appendix B
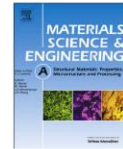# Enhanced ductility in dynamic strain aging regime in a Fe-25Ni-20Cr austenitic stainless steel

Short communication

Enhanced ductility in dynamic strain aging regime in a Fe-25Ni-20Cr austenitic stainless steel

Abdullah S. Alomari[a,b], N. Kumar[a], K.L. Murty[a]

[a] Department of Nuclear Engineering, North Carolina State University, Raleigh, NC, USA
[b] Atomic Energy Research Institute, King Abdulaziz City for Science and Technology, Riyadh, Saudi Arabia

ARTICLE INFO

ABSTRACT

Contrary to the commonly observed embrittlement during dynamic strain aging, we report in this note distinct enhancement in ductility in a Nb-containing and nitrogen stabilized Fe-25(wt%)Ni-20Cr austenitic stainless steel (Alloy 709) at temperatures from 623 K to 873 K at 10^{-4} s^{-1} where serrated flow is noted. This observation is rationalized in terms of the influence of strain hardening parameters and strain rate sensitivity on uniform elongation and ductility respectively.

In both interstitial and substitutional solid solution alloys, stress-strain curves during tensile deformation exhibit serrations known as Portevin-Le Chatelier effect (PLE) within a specific regime of temperature and strain rate [1,2]. The phenomenon is commonly attributed to a macroscopic observation of dynamic strain aging (DSA) resulting from the interaction between moving dislocations and solute atoms during deformation. Dislocations in a crystalline material move in intermittent way during plastic deformation. At elevated temperatures, solute atoms diffuse to the core of mobile dislocations during waiting time at obstacles and pin them leading to repeated locking and unlocking of the mobile dislocations during plastic deformation that give rise to serrated stress–strain curves [3–5]. Other indicators of the occurrence of DSA include peaks and/or plateaux of the flow stresses, decreased or negative strain rate sensitivity and minima in ductility [1,2]. DSA has been shown to cause an adverse effect on other mechanical properties of materials such as fatigue life [6] and fracture toughness [7], in addition to ductility [8–12]. It is believed that the detrimental effect of serrated flow on ductility is caused by the decreased strain rate sensitivity [5]. The embrittlement effect of DSA which is similar to the blue brittleness in ferritic steels is of importance since many engineering materials operate at the temperature range of DSA [13].

Ductility loss in DSA regime during tensile deformation has been numerously reported for various metals including ferritic steels [11], austenitic stainless steels [12], Al-based alloys [10], Ti-based alloys [8], and Zr-based alloys [9]. Contrary to this commonly observed detrimental effect, we report here a significant improvement in ductility during the DSA phenomenon in Alloy 709, a Nb-containing and nitrogen stabilized Fe-25Ni-20Cr austenitic stainless steel at temperatures

ranging from 623 K to 873 K (350–600 °C) where serrated flow is observed.

The material investigated in this study is a highly alloyed austenitic stainless steel (Alloy 709) which is a candidate structural material for next generation sodium fast reactors due to its excellent mechanical properties relative to conventional austenitic stainless steels such as SS304 and SS316 [14]. The Alloy 709 was received in the form of hot forged rectangular bar annealed at 1373 K (1100 °C) for 2 h followed by water-quenching with the following chemical composition (wt%) - C: 0.063, Mn: 0.88, Si: 0.28, P: < 0.005, S: < 0.001, Cr: 19.9, Ni: 25, Mo: 1.46, N: 0.14, Ti: < 0.01, Nb: 0.23, B: 0.0022, and the rest being Fe. The average grain size was determined to be 36.8 ± 7.3 μm using line intercept method. Rectangular pin-loaded tensile specimens with gage length of 20 mm were machined from the as-received plate and were tested using an Instron Universal tester equipped with a three-zone furnace at a constant cross-head velocity. Tensile tests were performed at a wide range of temperatures varying from 298 K to 1073 K (25–800 °C) and at two nominal strain rates of 10^{-3} s^{-1} and 10^{-4} s^{-1}. The temperature was maintained within ± 1 K (± 1 °C) and the soaking time for each sample was kept at 30 min for tests at each temperature. Tensile tests at 10^{-3} s^{-1} were repeated (2–3 times) to ensure the reproducibility of the tensile test data. The average values are reported with error bars corresponding to the standard deviations. The force and extension data during tensile tests were recorded using a load cell and LVDT installed on the testing machine. The microstructure of the as-received and deformed samples was characterized by Transmission Electron Microscopy (TEM) using a JEOL 2000FX S/TEM operated at an accelerating voltage of 200 kV.

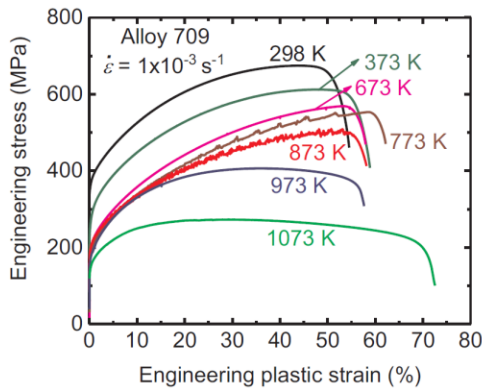Typical engineering stress-engineering strain curves of the Alloy

Fig. 1. Engineering stress – engineering strain curves at a strain rate of $1 \times 10^{-3}\,\mathrm{s^{-1}}$ at different temperatures.

709 as function of temperatures at a strain rate of $10^{-3}\,\mathrm{s^{-1}}$ are shown in Fig. 1. The alloy exhibits serrated flow during tensile deformation at intermediate temperatures depending on the strain rate. At a strain rate of $10^{-3}\,\mathrm{s^{-1}}$, serrations were found to be in the temperature range 573–973 K (300–700 °C) whereas it was confined in the range 523–923 K (250–650 °C) at $10^{-4}\,\mathrm{s^{-1}}$. For each stress-strain curve, the serrated flow commences after a finite amount of plastic deformation and continues until fracture occurs.

The variations of 0.2% yield strength (YS) and the ultimate tensile strength (UTS) with temperature are shown in Fig. 2. To emphasize the influence of temperature on strength values, normalized YS and UTS by Young's modulus are considered. The values of Young's modulus, E at various temperatures for the Alloy 709 have been obtained from $E = 6895(28.73 - 0.01T)$ where E is in MPa and the temperature, T in °C for a 20%Cr-25%Ni-Nb stabilized austenitic stainless steel [15]. At both strain rates, a slight decrease in the normalized UTS from 298 to 373 K (25–100 °C) is observed followed by a peak at intermediate temperatures before it rapidly decreases at higher temperatures. The variation of the normalized YS exhibits a significant decrease with increase in temperature from 298 to 473 K (25–200 °C) followed by a plateau or slight peak depending on the strain rate at intermediate temperatures. With further increase in the temperature, a moderate decrease in YS is observed at both strain rates. It is noted that the peaks and plateaux observed in the YS and UTS coincided very well with the occurrence of serrated flow regime.

Also shown in Fig. 2 are the temperature variations of ductility defined as the elongation-to-fracture, ε_f, uniform elongation, ε_u (i.e. elongation up to maximum load in an engineering stress – engineering strain curve) and non-uniform elongation, ε_{nu} (i.e. post-uniform elongation or necking strain defined as $\varepsilon_{nu} = \varepsilon_f - \varepsilon_u$). A slight decrease in ε_f with temperature ranging from 298 to 673 K (25–400 °C) is found before a significant peak is observed at 773 K (500 °C) in serrated flow regime followed by a rapid increase at high temperatures. Further, the variations of ε_u and ε_{nu} with temperature are also included in Fig. 2, and ε_u shows no significant variation with temperature up to 673 K (400 °C) followed by a pronounced peak at around 773 K (500 °C) before a sharp decrease at higher temperatures. Unlike the ε_f, the ε_{nu} exhibits a slow decrease from 298 to 573 K (25–300 °C) followed by a wide minimum at intermediate temperatures 573–873 K (300–600 °C) followed by a sharp increase at high temperatures.

The microstructure of the Alloy 709 before testing is shown in Fig. 3(a) where relatively low dislocation density and some preexisting fine precipitates of less than 200 nm are typically observed. Fig. 3(b) shows a TEM image of the Alloy 709 strained to failure at a temperature of 573 K (300 °C) and strain rate of $10^{-3}\,\mathrm{s^{-1}}$ within the DSA regime
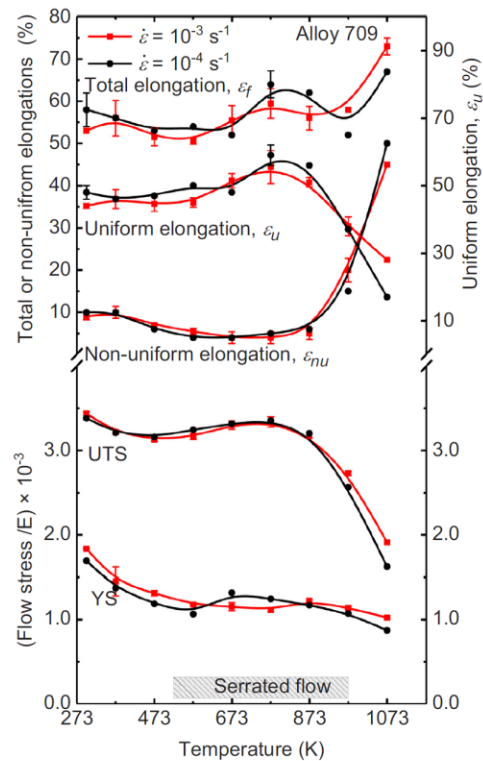

Fig. 2. Effect of test temperature on yield (YS) and tensile strengths (UTS) as well as ductility (ε_f), uniform (ε_u) and non-uniform (ε_{nu}) elongations at two different strain rates.

where a high degree of planarity of dislocation glide is noted. The observed linear dislocation substructure was pronounced as a manifestation of deformation by planar slip of dislocations restricting the cross-slip and recovery due to DSA at intermediate temperatures [16]. For comparison, Fig. 3(c) includes a TEM image of the alloy deformed at 373 K (100 °C) (outside DSA regime) showing non-planar arrangement of dislocation substructure.

The temperature-strain rate regime for the occurrence of serrated flow and the observed peaks/plateaux of the YS and UTS in the Alloy 709 are consistent with the observations reported for various austenitic stainless steels where the diffusivity of solute atoms is comparable to the average velocity of the mobile dislocations during tensile deformation [17,18]. In SS316L(N) austenitic stainless steel, Choudhary reported minima in elongation-to-fracture at temperatures ranging from 523 to 873 K (250–600 °C) and related this effect to the negative strain rate sensitivity observed in this regime [12]. In type AISI 316 steel, Almeida and Monteiro have reported a constant uniform elongation inside the DSA range [19]. They attributed this behavior to the large work hardening rate in DSA regime. In mild steel, the change in the work hardening characteristics of the material in the DSA temperature range leading to the onset of necking at small strains was suggested to be responsible for the loss in ductility [20]. In contrast, we note here a pronounced peak in serrated flow regime for the total and uniform elongations at both strain rates in the Alloy 709.

To develop better understanding about this contradictory observation in the Alloy 709, the strain rate sensitivity (m), the strain hardening exponent (n) and work hardening rate (θ) are examined. The strain rate sensitivity (m) is determined from the equation: $m = \ln(\sigma_1/\sigma_2)/\ln(\dot{\varepsilon}_1/\dot{\varepsilon}_2)$
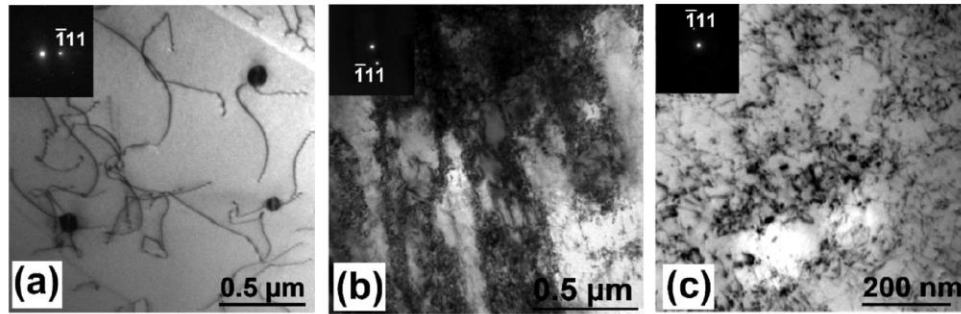
Fig. 3. (a) Bright field TEM image for the undeformed Alloy 709, (b) the deformed Alloy 709 at temperature of 573 K and strain rate of $10^{-3}\,\text{s}^{-1}$ (DSA regime), and (c) the deformed Alloy 709 at temperature of 373 K and strain rate of $10^{-3}\,\text{s}^{-1}$ (non-DSA regime). The insets show corresponding selected area diffraction patterns.
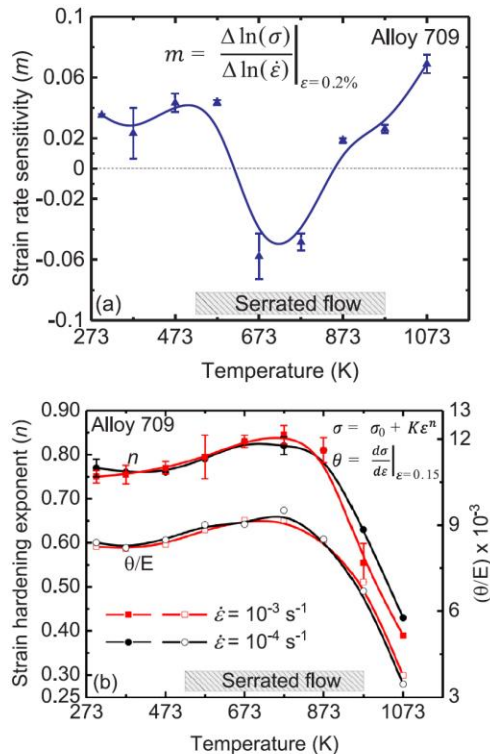

Fig. 4. a. Strain rate sensitivity (m) vs temperature. b. Temperature variations of strain hardening exponent (n) (left scale) and normalized work-hardening rate (θ/E) at true plastic strain of 0.15 at two different strain rates.

where σ_1 and σ_2 are flow stresses at strain rates of 10^{-3} and $10^{-4}\,\text{s}^{-1}$ respectively. The values of m as a function of temperature are shown in Fig. 4(a) where negative strain rate sensitivity is clearly observed in the serrated flow regime. In the absence of DSA, strain rate sensitivity is reported to increase monotonically with temperature inhibiting the growth of localized deformation after necking resulting in high ductility [5]. A proportional relationship between elongation to fracture and strain rate sensitivity is well established in many metals and alloys [21]. In DSA regime, solute atoms diffuse to the mobile dislocations and pin them enhancing the localized deformation leading to a negative strain rate sensitivity. A decreasing value of m in DSA regime would mean diminishing tendency toward preventing localized deformation

resulting therefore in decreased ductility. The reduction in non-uniform elongation in the Alloy 709 at intermediate temperatures can be explained by the negative strain sensitivity found in DSA regime. After the neck formation, the failure is enhanced due to the low m-value. On the other hand, the strain hardening behavior during deformation is a key factor influencing the ductility, particularly the uniform elongation since strain hardening exponent (n) is equal to true uniform strain: $n = \varepsilon_u$.

A high value of strain hardening exponent will enhance the uniform elongation which might also improve the overall ductility [22]. To estimate the strain hardening exponent in the Alloy 709, true stress-true strain curves up to the point of necking were curve-fitted using the least square fit with Ludwik's equation: $\sigma = \sigma_o + K\varepsilon^n$ where σ_o, K and n are constants representing yield stress, strain hardening coefficient and strain hardening exponent respectively; the correlation coefficients, R^2 for all fitting curves, were higher than 0.98. Fig. 4(b) shows the values of n as a function of temperature at different strain rates in the Alloy 709 where a significant peak in the strain hardening exponent is observed in the serrated flow regime depicting the increase in the uniform elongation (Fig. 2). Similarly, the work-hardening rate, θ (where θ is defined as the first derivative of the Ludwik's equation) is influenced by the occurrence of DSA. The variations of the normalized work-hardening rate, θ/E at true plastic strain of 0.15 with temperature at different strain rates are also shown in Fig. 4(b), and θ/E exhibits peaks at intermediate temperatures where serrated flow occurs. Consequently, the net effect was a ductility enhancement in the DSA regime due to the relatively large uniform strain while the negative strain sensitivity was not sufficient to form the necking earlier. Further investigation into this observation and a detailed microstructural evaluation is underway and will be reported along with further details on kinetics of DSA such as the activation energy and correlations between the strain-rate and strain.

It is interesting to compare the current results on Alloy 709 with those reported for 316SS [12] and Fe-14%Cr-15Ni SS [23] and Fig. 5 summarizes the total elongation to fracture for these alloys where the enhanced ductility during DSA in the Alloy 709 is clearly demonstrated. Recently, Calmunger et al. reported improved ductility of a highly alloyed austenitic stainless steel within the DSA regime and concluded that both high Ni content and deformation twining govern the better ductility within DSA [24]. The Alloy 709 has a relatively large amount of Ni which may have bearing on work hardening parameters n and θ responsible for the enhancement of the uniform elongation and hence the ductility in DSA regime.

In summary, the serrated flow in the stress-strain curves were observed in an austenitic stainless steel (Alloy 709) at temperatures ranging from 523 to 973 K (250–700 °C) and at two nominal strain rates of 10^{-3} and $10^{-4}\,\text{s}^{-1}$. Although the peaks/plateaux in the YS and UTS and negative strain sensitivity were observed in the serrated flow
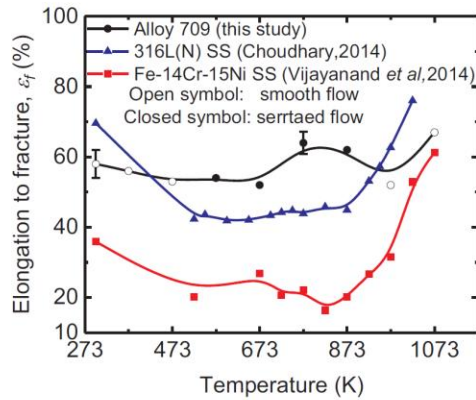
Fig. 5. Temperature variation of ductility in Alloy 709 vs SS.

regime, increased ductility is noted in lieu of ductility minima commonly reported. This contradictory observation was attributed to the increase in the strain hardening exponent and work hardening rate in dynamic strain aging regime illustrating the fact that DSA is not always detrimental to metals [25].

Acknowledgments

References

[1] P. Rodriguez, Serrated plastic flow, Bull. Mater. Sci. 6 (1984) 653–663.
[2] J.M. Robinson, M.P. Shaw, Microstructural and mechanical influences on dynamic strain aging phenomena, Int. Mater. Rev. 39 (1994) 113–122.
[3] P.G. McCormick, A model for the Portevin-Le Chatelier effect in substitutional alloys, Acta Metall. 20 (1972) 351–354.
[4] A. van den Beukel, Theory of the effect of dynamic strain aging on mechanical properties, Phys. Status Solidi A 30 (1975) 197–206.
[5] L.P. Kubin, Y. Estrin, Dynamic strain ageing and the mechanical response of alloys, J. Phys. III 1 (1991) 929–943.
[6] V.S. Srinivasan, M. Valsan, R. Sandhya, K. Bhanu Sankara Rao, S.L. Mannan, D.H. Sastry, High temperature time-dependent low cycle fatigue behaviour of a type 316L(N) stainless steel, Int. J. Fatigue 21 (1) (1999) 11–21.
[7] Y.H. Jung, K.L. Murty, Effect of temperature and strain rate on upper shelf fracture behavior of A533B Class 1 pressure vessel steel, in: T.A. Cruse (Ed.), Fracture Mechanics Nineteenth Symposium, ASTM, STP 969, Philadelphia, 1988, pp. 392–401.
[8] M. Doner, H. Conrad, Deformation mechanisms in commercial Ti (0.5 at. pct oineq) at intermediate and high temperatures (0.3–0.6 tinm), Metall. Trans. 4 (1973) 2809–2817.
[9] S.I. Hong, W.S. Ryu, C.S. Rim, Elongation minimum and strain Ram sensitivity minimum of Zircaloy-4, J. Nucl. Mater. 116 (1983) 314–316.
[10] E. Bouchaud, L. Kubin, H. Octor, Ductility and dynamic strain aging in rapidly solidified aluminum alloys, Metall. Trans. A 22 (1991) 1021–1028.
[11] C. Gupta, J.K. Chakravartty, S.L. Wadekar, J.S. Dubey, Effect of serrated flow on deformation behaviour of AISI 403stainless steel, Mater. Sci. Eng. A 292 (2000) 49–55.
[12] B.K. Choudhary, Influence of strain rate and temperature on tensile deformation and fracture behavior of type 316L(N) austenitic stainless steel, Metall. Mater. Trans. A 45 (2014) 302–316.
[13] K.L. Murty, E.O. Hall, Dynamic strain-aging and neutron irradiation in mild steel, in: Irradiation Effects on the Microstructure and Properties of Metals, ASTM STP611, 1976, pp. 53–71.
[14] T.-L. Sham, L. Tan, Y. Yamamoto, Development of advanced 9Cr ferritic-martensitic steels and austenitic stainless steels for sodium-cooled fast reactors, in: Fast Reactors and Related Fuel Cycles: Safe Technologies and Sustainable Scenarios (FR13), IAEA, Vienna, 2015, pp. 1–9.
[15] E.G. Wilson, Stress Varied Creep of 20%Cr-25%Ni-Nb Stabilized Austenitic Stainless Steel, Creep Strength in Steel and High Temperature Alloys, The Metal Society, London, 1972, pp. 111–121.
[16] W. Karlsen, M. Ivanchenko, U. Ehrnstén, Y. Yagodzinskyy, H. Hänninen, Microstructural manifestation of dynamic strain aging in AISI 316 stainless steel, J. Nucl. Mater. 395 (1) (2009) 156–161.
[17] L.H.D. Almeida, I.L. May, S.N. Monteiro, Effects of carbon and nitrogen levels on the temperature ranges for serrated flow in austenitic stainless steel, in: H.J. McQueen, J.P. Bailon, J.I. Dickson, J.J. Jonas, M.G. Akben (Eds.), Strength of Metals and Alloys (ICSMA 7), Pergamon Press, Oxford, 1985, pp. 337–342.
[18] V. Ganesan, K. Laha, M. Nandagopal, P. Parameswaran, M.D. Mathew, Effect of nitrogen content on dynamic strain ageing behaviour of type 316LN austenitic stainless steel during tensile deformation, Mater. High Temp. 31 (2014) 162–170.
[19] L.H.d. Almeida, S.N. Monteiro, The significance of dynamic strain aging in austenitic stainless steel, in: Proceedings of the second International Conference on Mechanical Behavior of Materials, ASM, Metals Park, 1976, pp. 1697–1701.
[20] B.J. Brindley, The effect of dynamic strain ageing on the ductile fracture process in mild steel, Acta Metall. 18 (1970) 325–329.
[21] D.W. Woodfrod, Strain rate sensitivity as a measure of ductility, Trans. ASM 62 (1969) 291–293.
[22] K.L. Murty, I. Charit, An Introduction to Nuclear Materials: Fundamentals and Applications, Wiley-VCH, Weinheim, 2013.
[23] V.D. Vijayanand, K. Laha, P. Parameswaran, M. Nandagopal, S. Panneer Selvi, M.D. Mathew, Influence of thermo-mechanical treatment on the tensile properties of a modified 14Cr–15Ni stainless steel, J. Nucl. Mater. 453 (2014) 188–195.
[24] M. Calmunger, G. Chai, R. Eriksson, S. Johansson, J.J. Moverare, Characterization of austenitic stainless steels deformed at elevated temperature, Metall. Mater. Trans. A 48 (2017) 4525–4538.
[25] M. Srinivas, G. Malakondaiah, K.L. Murty, P.R. Rao, Fracture toughness in the dynamic strain ageing regime, Scr. Metall. Mater. 25 (1991) 2585–2588.

Investigation on Creep-Fatigue Interaction of Fe-25Ni-20Cr Austenitic Stainless Steel (Alloy 709)

A. S. Alomari,[1, 2]* N. Kumar,[1, 3] K.L. Murty[1]

[1]*Department of Nuclear Engineering, North Carolina State University, Raleigh, NC, USA*
[2]*Atomic Energy Research Institute, King Abdulaziz City for Science and Technology, Riyadh, Saudi Arabia*
[3]*Department of Metallurgical and Materials Engineering, The University of Alabama, Tuscaloosa, AL, USA*
*asalomar@ncsu.edu

INTRODUCTION

Creep-fatigue interaction is expected to be a contributor to the damage mode for many high-temperature components of next-generation nuclear reactors such as reactor pressure vessels and gas turbines [1-5]. Cyclic loadings originating from the power transients during operation as well as startups and shutdowns lead to degradation of engineering components through fatigue while inherent stress relaxation during steady operation induces creep deformation. Hence; understating the interaction among creep and fatigue degradation mechanisms at high temperatures is essential to determine a component's lifetime and design safety margins for nuclear reactors.

Alloy 709, a highly alloyed austenitic stainless steel with base Fe-20Cr-25Ni containing niobium and nitrogen, is an excellent candidate structural material for Sodium Fast Reactor due to good mechanical properties relative to code-approved reference construction materials such as 316 stainless steel [6]. In this summary, the creep-fatigue interaction of the Alloy 709 is investigated by conducting fatigue tests under strain-controlled mode at 1% total strain range, 2×10^{-3} s^{-1} strain rate (0.1 Hz) and 750 °C with hold times of 60, 600, 1800 sec at the tensile strain. The results are reported and creep-fatigue life predictions using the linear summing rule are developed.

MATERIAL AND METHODS

The Alloy 709 used in this investigation was received in the form of a hot-rolled plate annealed at 1100°C followed by water-quenching. Creep-fatigue specimens were machined from the as-received plate samples with 3 mm diameter gage section and 10 mm gage oriented length along rolling direction. Sample geometry is shown in Figure 1(a). The creep-fatigue tests were carried out using an electro-dynamic creep-fatigue machine (Model 810LE3) from TestResources Inc., equipped with a 3-zone furnace to enable high temperature testing. The temperature is measured using a K-type thermocouple attached to the gage section of the sample and maintained within ±2 °C during the test., and experimental set-up are shown in Figure 1(b). The strain is measured with an accuracy of 2 μm displacement (or 0.02% strain) using a Linear Variable Differential Transducer (LVDT) attached to a high temperature extensometer mounted on the grip-section of the sample.

Strain-controlled creep-fatigue tests were performed under constant strain rate of 2×10^{-3} s^{-1} at total strain range of 1% (fully reversed with strain ratio R = −1) at 750 °C in air. All tests were conducted as described in the ASTM standard E2714–13 [7] with hold times of 60, 600, and 1800 s. The hold time was done at the maximum tensile strain every cycle resulted in interrupted creep regimes. When no hold time is introduced (continuous cycling), a triangle waveform was used (Figure 2a). The waveform with hold time is shown schematically in Figure 2(b). Corresponding variation of the stress and hysteresis loops during loading cycles are also shown schematically in Figure 2.

RESULTS AND DISCUSSIONS

Cyclic deformation response

The 1st and 100th cycle of creep-fatigue hysteresis loops for the Alloy 709 at different hold times are shown in Figures 3(a) and 3(b) respectively. The width of the hysteresis loops is found to increase with the hold time suggesting the rise of the inelastic strain with hold time [4]. The shapes of hysteresis loops of creep-fatigue with different hold times are similar; however, the hysteresis loops exhibit serrations at 100th cycle in continuous cycling deformation (0 hold time). It is not confirmed yet if these serrations are related to the dynamic strain aging found in this alloy [8].
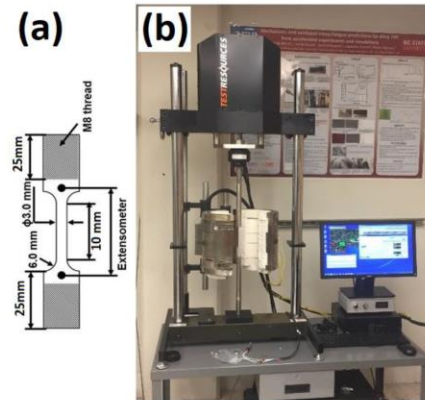

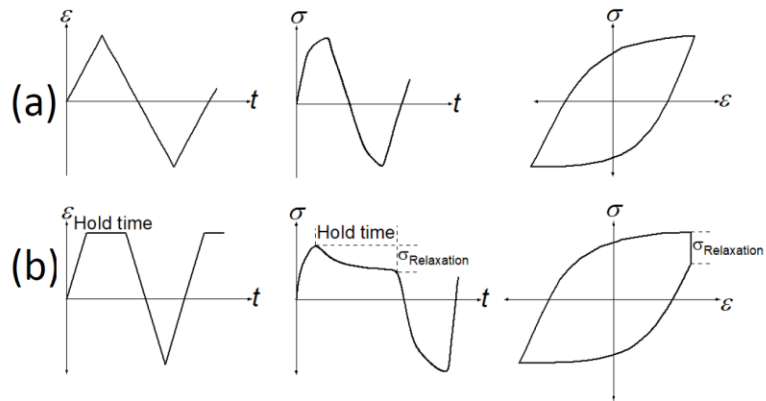Fig.1. (a) sample geometry and (b) Experimental set-up.

Fig.2. Schematic of loading cycle of the strain-controlled creep-fatigue test showing strain–time, stress–time and stress–strain (hysteresis loop) curves (a) without hold time and (b) with hold time imposed at the peak tensile strain.
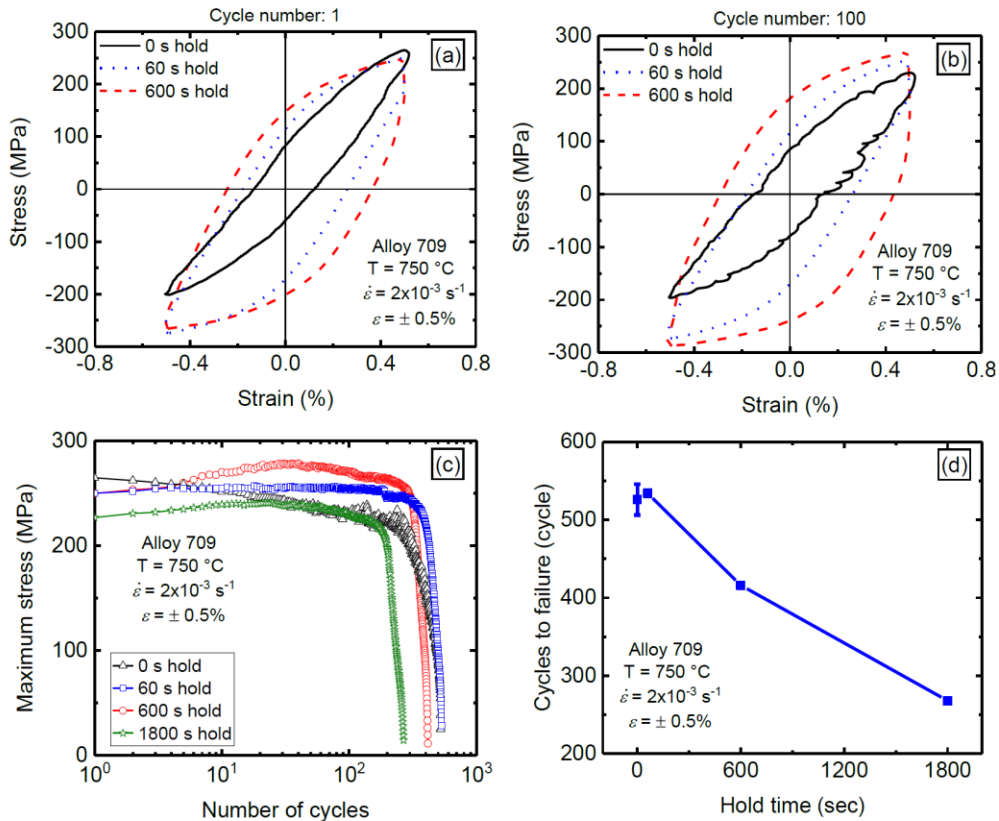

Fig.3. (a) and (b) Hysteresis loops for the creep-fatigue tests of the Alloy 709 at different hold times showing the 1st and 100th cycles respectively. (c) Maximum stress (tesnsle) vs. member of cycle. (d) Cycle to failure vs. hold time in the Alloy 709.

To get a complete picture of cyclic deformation behavior during creep-fatigue tests for the Alloy 709, maximum stresses during tension in the loading cycles were plotted versus the number of cycles for 0, 60, 600 and 1800 sec hold times and are shown in Figure 3(c). In continuous cyclic loading without imposing hold time, the alloy exhibits cyclic softening behavior while cyclic hardening response was observed for deformation with hold time. Moreover, the degree of cyclic hardening becomes more pronounced with increased hold time. The change of the cyclic behavior is linked with the microstructure and can be due to (i) dislocation-dislocation interaction, (ii) dislocation–precipitate interaction and (iii) dislocation–solute atom interaction [9]. The variation of creep-fatigue life as a function of hold time is shown in Figure 3(d). In general, the creep-fatigue life of the alloy decreases with increasing in hold time. For the slowest hold time-tested (60 sec), the creep-fatigue life showed life similar to the test conducted with no hold time. Hold time sensitivity may be attributed to the accumulated creep deformation and damage during hold period at tensile strain [4, 9].

Stress relaxation during creep-fatigue tests

Figure 4 shows the stress relaxation curves of the Alloy 709 for 60, 600 and 1800 sec hold times where all the stress relaxation curves are quite similar with the stress dropping rapidly at the beginning followed by a relatively stable state of stress relaxation. However, the minimum stress during relaxation is found to be reduced significantly with the increased hold time. The function of stress (σ) during relaxation period (t) was fitted with the power-law equation as following

$$\sigma = b_\circ (t + t_\circ)^{b_1}. \qquad (1)$$

where $b_\circ$, $t_\circ$ and b_1 are fitted parameters. The fitted-curves are plotted as solid lines in Figure 4.
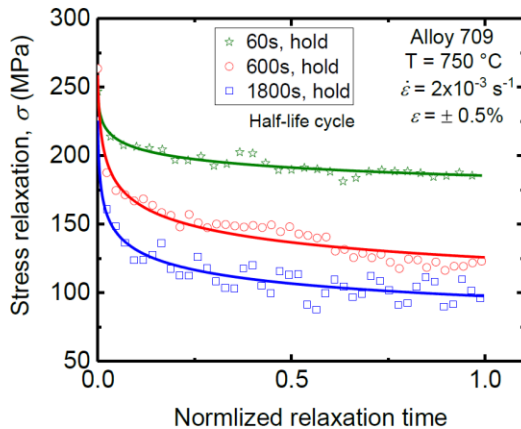

Fig. 4. Stress relaxation with time at different hold times.

Since the creep-fatigue tests were conducted under strain controlled (*i.e.,* constant total stain, $\varepsilon_t = Constant$), it is possible to determine the creep rate ($\dot{\varepsilon}_c$) during hold time from the slope of the stable state of stress relaxation curve. In other words

$$\dot{\varepsilon}_t = \dot{\varepsilon}_E + \dot{\varepsilon}_c = 0 \quad \rightarrow \quad \dot{\varepsilon}_c = -\dot{\varepsilon}_E - \frac{1}{E}\dot{\sigma} \qquad (2)$$

where $\dot{\varepsilon}_t$, $\dot{\varepsilon}_E$, $\dot{\varepsilon}_c$ and $\dot{\sigma}$ are total strain rate, elastic strain rate, plastic strain rate and stress rate respectively and E is the elastic modulus. The creep rate during relaxation was determined to be in the range of $5 \times 10^{-4} - 4.2 \times 10^{-6}$ sec^{-1} for the hold time of 60 and 600 sec whereas creep rate reached 5.9×10^{-8} sec^{-1}. The dependence of the creep rate on the stress was found to follow Norton's power law with stress exponent (n) between 5.9–10.5 which is comparable to the value obtained for this alloy ($n = 7$) [10].

Creep-fatigue life prediction

During cycling loading, fatigue damage occurs whereas creep damage is expected to be accumulated during the hold time; hence, the interaction of creep and fatigue damage may occur. Different methods have been used to predict creep-fatigue life [2, 5] while the most widely selected approach for many engineering alloys is the linear damage summation developed by the assumption that the creep and fatigue damage mechanisms act independently. The linear damage summation rule is as follows

$$\underbrace{\sum_{j=1}^{p} \left(\frac{N_{cf}}{N_f} \right)_j}_{Fatigue\ damage,\ D_f} + \underbrace{\sum_{k=1}^{q} \left(\frac{\Delta t}{t_f} \right)_k}_{Creep\ damage,\ D_c} \leq D. \qquad (3)$$

where N_{cf} and N_f are the number of cycles of creep-fatigue tests with and without hold time respectively performed under the same test condition of type j (same type of material, total strain range, strain rate, and temperature), Δt and t_f are the actual time at a certain stress- temperature level k and the creep life time at corresponding stress-temperature level, respectively and D is the allowable combined damage fraction where the total damage is usually assumed to be equal to one. Fatigue damage calculation is relatively straightforward and the ratio of the cycles to failure for each hold time to the cycles to failure under continuous cycling condition was employed in the present study. However, the calculation for creep damage is quite complicated since the stress during hold time is no longer constant. In a creep test, the stress/load is kept constant for obtaining the rupture life whereas stress relax during the hold time in the imposed test condition. In the present investigation, two approaches have been used for the

calculation of creep damage viz. (i) minimum stress and (ii) integration of creep damage over the hold time duration at the half-life cycle. The first approach is simple where the stress at the end of relaxation for half-life cycle and the time to rupture at this level of stress from creep data were employed. However, the second approach needs integration of stress relaxation curve with respect to time over the hold period. To perform the integration, the correlation between the rupture time, temperature, and applied stress for the Alloy 709 are required. Following the analysis by Wright *et al.* [3], and using Eq.1 and the Larson-Miller relation developed for this alloy [10], creep damage was calculated as

$$D_c = \frac{b_\circ^{-m}}{A(1 - b_1 m)}\left[\left(t_h + t_\circ\right)^{1 - b_1 m} - \left(t_\circ\right)^{1 - b_1 m}\right] \quad (4)$$

where t_h is the stress relaxation hold time in seconds. A and m are the fitting parameters in the Larson-Miller parameter as a function of stress. The creep damage in Equation 4 was calcuated only at the half-life cycle and then multiplied by the corresponding creep-fatigue life. Figure 5 shows the creep-fatigue interaction diagram for the Alloy 709 where creep damage is plotted as a function of the fatigue damage at different hold times using the minimum stress and integration methods. In this figure, the linear damage summation failure criterion is also plotted. It is seen that the minimum stress method underestimated the creep-fatigue life in comparison to the integration method. Due to very limited testing and availability of creep-fatigue data for the Alloy 709, we cannot at present make any conclusions based on this comparison.
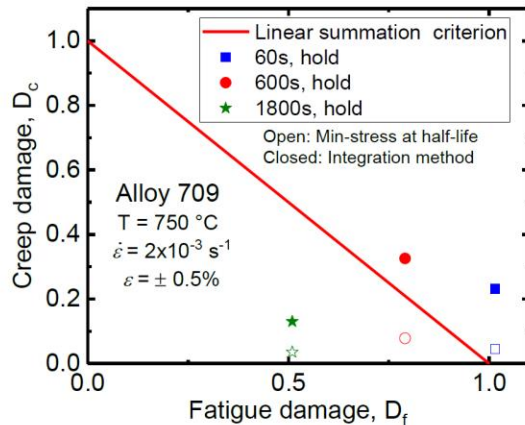

Fig. 5. Creep-fatigue interaction diagram based on linear damage summation. The solid red line shows the linear damage summation.

CONCLUSIONS

Creep-fatigue tests have been carried out on the Alloy 709, a candidate structural material for next-generation Sodium Fast Reactor, under strain-controlled mode at 1% total strain range, 2×10^{-3} s^{-1} strain rate and 750 °C without

hold time (Continuous cyclic loading) and with hold times of 60, 600, 1800 sec at the maximum strain. The alloy exhibits cyclic softening behavior under continuous cyclic loading whereas cyclic hardening response was observed with imposed hold times. The creep-fatigue life is found to decrease with increased hold time. Linear damage summation rule was employed to predict the creep-fatigue life where creep damage was calculated using the minimum stress during relaxation and integration of stress relaxation curve. Minimum stress method is found to underestimate the creep-fatigue life. However, further studies are underway to carry out creep-fatigue tests at different hold times, strain ranges, and temperatures as well as microstructural characterization of the samples following deformation.

REFERENCES

1. K.L. Murty and I. Charit, *An Introduction to Nuclear Materials : Fundamentals and Applications*, Wiley-VCH, Weinheim, (2013).
2. X. Zhang, et al., "Creep–fatigue endurance of 304 stainless steels," *Theor. Appl. Fract. Mech.*, **71**, pp. 51-66, (2014).
3. J.K. Wright, et al., "Determination of the Creep–Fatigue Interaction Diagram for Alloy 617," *Proc. of the ASME 2016 Pressure Vessels and Piping Conference*, p.255, Vancouver, Canada, (2016).
4. R.T. Dewa, et al., "High-Temperature Creep-Fatigue Behavior of Alloy 617," *Metals*, **8**, p. 103, (2018).
5. R.-Z. Wang, et al., "Creep-Fatigue Behaviors and Life Assessments in Two Nickel-Based Superalloys," *J. Pressure Vessel Technol.*, **140**, (2018).
6. T.-L, Sham, L. Tan, and Y. Yamamoto, "Development of Advanced 9Cr Ferritic-Martensitic Steels and Austenitic Stainless Steels for Sodium-Cooled Fast Reactors, in in: Fast Reactors and Related Fuel Cycles: Safe Technologies and Sustainable Scenarios (FR13), IAEA: Vienna. pp. 1-9, (2015).
7. ASTM Standard E2714 -13, "*Standard Test Method for Creep-Fatigue Testing*," ASTM International, (2013).
8. A.S. Alomari, et al., "Enhanced ductility in dynamic strain aging regime in a Fe-25Ni-20Cr austenitic stainless steel," *Mater. Sci. Eng. A*, **729**, pp. 157-160, (2018).
9. M.C. Carroll and L.J. Carroll, "Developing Dislocation Subgrain Structures and Cyclic Softening During High-Temperature Creep–Fatigue of a Nickel Alloy," *Metall. Mater. Trans. A*, **44**, pp. 3592-3607, (2013).
10. A.S. Alomari, et al., "High Temperature Creep Properties of Alloy 709," *To be published*.

Chapter 5
Understanding Creep-Fatigue Interaction in Fe-25Ni-20Cr (wt%) Austenitic Stainless Steel

N. Kumar, A. Alomari, and K. L. Murty

Abstract Gen-IV nuclear reactors require materials to operate under much harsher conditions necessitating the development of advanced structural materials. Sodium-cooled Fast Reactor (SFR) is a Gen-IV nuclear reactor with a high level of technology readiness. Alloy 709, Fe-25Ni-20Cr (wt%) alloyed with Nb and stabilized with nitrogen, is an advanced austenitic stainless steel having promising set of properties for SFRs. However, the creep-fatigue deformation behavior is unknown for this alloy. This work focuses on evaluating creep-fatigue interaction in this alloy. We report here a creep-fatigue study conducted at 750 °C using triangular waveform following the ASTM standard E2714–13 at 0.1 Hz frequency. The creep-fatigue tests were conducted in strain-controlled mode where strain amplitudes of 0.2% and 0.5% were used. The micro-structural examination in as-received and post-deformation conditions were carried out using scanning and transmission electron microscopes. The creep-fatigue lives at 0.2% and 0.5% strain amplitudes were 17,416 and 526 cycles, respectively. The comparison of the TEM micrographs between as-received and creep-fatigue deformed at 0.5% strain amplitude showed higher dislocation density and loosely defined subgrains in the deformed alloy. The fractographs indicated that for the samples deformed at 0.2% strain amplitude, fatigue might have been the dominant mode of deformation whereas for the sample deformed at 0.5% strain amplitude, fatigue and creep both might have contributed to the overall deformation of the alloy.

Keywords Austenitic stainless steel · Gen-IV nuclear reactor · Mechanical properties · Creep-fatigue · Plastic deformation

5.1 Introduction

Advanced materials are needed to perform satisfactorily in much harsher service conditions envisioned to exist in Gen-IV nuclear reactors [1, 2]. In last few decades, to address the need of such advanced reactors, advanced materials such as modified austenitic stainless steels, ferritic/martensitic steels, and nickel based superalloys have been developed with desired combination of properties [3]. To ensure structural integrity of engineering structures in such harsh conditions for their safe and economical operation, it becomes imperative to understand their deformation behavior fully under the prevailing loading conditions.

In many engineering structures such as reactor pressure vessels and gas turbines, load variations particularly thermal load during start-up and shut-down periods lead to degradation of engineering components through fatigue and evidence suggests that such components fail at low number of cycles (usually less than 10^4 cycles) [4]. The degradation of materials by low-cycle fatigue (LCF) is exacerbated by other high temperature degradation phenomena such as microstructural instability, creep, oxidation, and dynamic strain aging. The synergy between different degradation processes leads to accelerated degradation of such engineering structures [5]. It, therefore, calls upon studying interaction among different degradation mechanisms at high temperatures and underlying mechanism(s) controlling the properties of metallic materials under such loading conditions.

In this context, understanding interaction between LCF and creep is important by simulating real steady and varying load conditions during operation and shut-down periods of a reactor. The present work focuses on creep-fatigue deformation behavior of a Nb-modified Fe-25wt%Ni-20Cr stabilized with nitrogen (here afterwards referred to as Alloy 709) at elevated temperature in strain-controlled mode. The Alloy 709 is an advanced next-generation austenitic stainless steel found suitable for use in sodium cooled fast reactors (SFR). Although preliminary investigation on the mechanical properties does support its use in SFR, a detailed micro-mechanistic understanding is yet to evolve specially under creep-fatigue loading conditions.
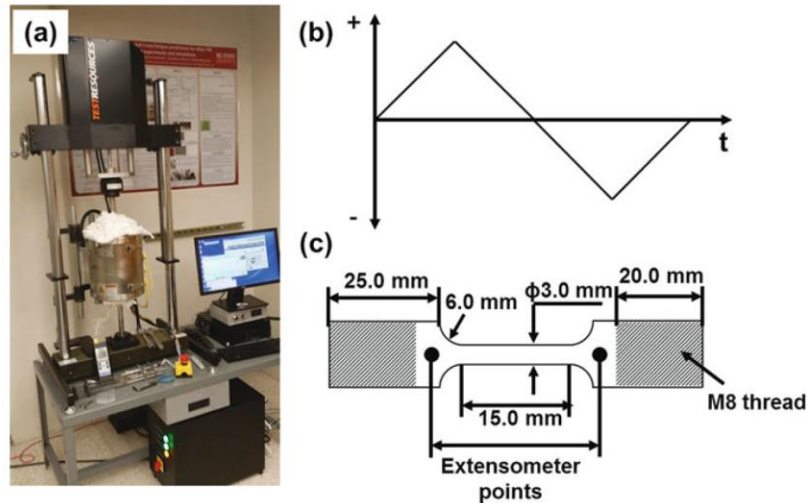
N. Kumar (✉) · A. Alomari · K. L. Murty
Department of Nuclear Engineering, North Carolina State University, Raleigh, NC, USA

Table 5.1 Chemical composition (wt%) of Alloy 709 used in this study

Element	C	Mn	Si	P	S	Cr	Ni	Mo	N	Ti	Nb	B	Fe
(Wt%)	0.07	0.91	0.44	<0.014	<0.000	19.93	24.98	1.51	0.148	0.04	0.26	0.0045	bal.

Fig. 5.1 Experimental set-up; (**a**) creep-fatigue machine, (**b**) low frequency triangular wave form, and (**c**) sample geometry

5.2 Experimental Methods

The as-received plate of the Alloy 709 had undergone hot-rolling followed by solution-annealing heat-treatment at 1100 °C followed by water quenching. The chemical composition of the alloy is given in Table 5.1. It is a next generation austenitic stainless steel developed by Oak Ridge National Lab and is being considered for Sodium-Cooled Fast Reactors (one of Gen-IV reactor types).

The creep-fatigue tests were carried out using an electro-dynamic creep-fatigue machine (Model 810LE3) from TestResources, Inc. The machine is equipped with fatigue rated load cell with a maximum capacity of ± 1000 lb. To enable high temperature testing, a furnace from Applied Testing Systems was used during creep-fatigue tests. The temperature during the test was controlled using a K-type thermocouple wrapped around the gage section of the cylindrical test sample. All the tests were conducted in constant-amplitude strain-controlled mode as described in the ASTM standard E2714 – 13. The strain was measured and controlled using an extensometer mounted on the grip-section of the sample. The experimental set-up is shown in Fig. 5.1 which includes creep-fatigue testing machine, a schematic of the strain-controlled loading cycle, a 2-dimensional drawing of the test sample, and the grip positions of the extensometer on the sample.

For microstructural examination, transmission electron microscope (TEM) and scanning electron microscope (SEM) were used. The sample for the TEM was prepared using twin-jet electro-polishing in 10 vol% perchloric acid + 90 vol% methanol solution at ~ -35 °C at a voltage of 20 V. The TEM examination of the sample was done using JEOL 2000FX TEM. The fractured samples were cleaned in acetone before performing fractography in the SEM. The fractography was carried out in the FEI Quanta 3D FEG.

5.3 Results and Discussions

5.3.1 Microstructure of the As-Received Material

Figure 5.2a shows an SEM image taken in backscattered electron imaging mode. Microstructural features such as annealing twins and grain-boundaries can be noted from this figure. Grain morphology is irregular and some of the grains seen in the micrographs are larger than 50 μm. Electron backscattered diffraction is being carried out to obtain information on grain size

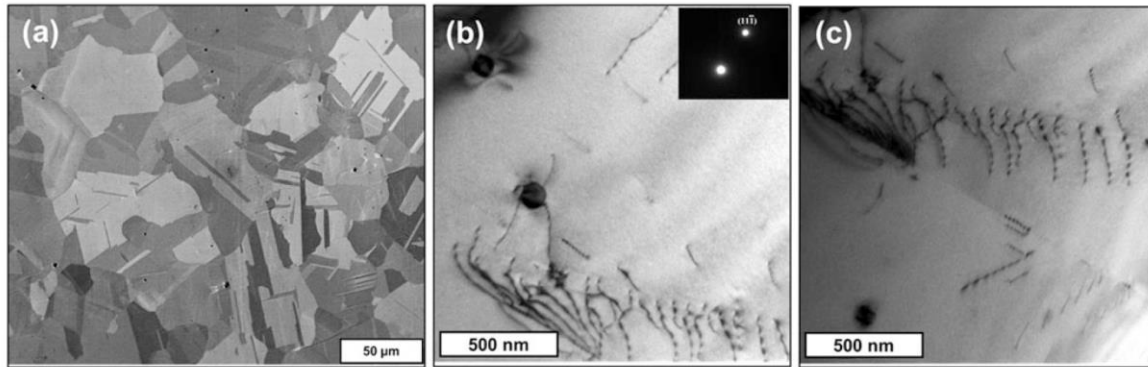**Fig. 5.2** (**a**) An SEM micrograph of the as-received Alloy 709 taken in backscattered electron mode and (**b**, **c**) bright-field TEM micrographs at zone axis [112] showing dislocations
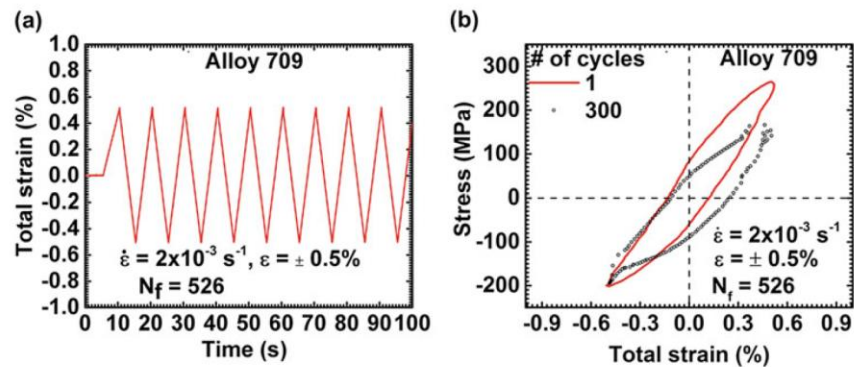

Fig. 5.3 (**a**) Triangular waveform used during the creep-fatigue test, frequency = 0.1 Hz (strain-rate = 2×10^{-3} s^{-1}) (**b**) stress-strain hysteresis loops for cycles 1 and 300 for the Alloy 709

and its distribution. Two bright-field TEM images taken from two different regions of the TEM sample in two-beam condition are shown in Fig. 5.2b, c. The TEM analysis of the as-received material indicated a very low density of dislocations. In Fig. 5.2b, c the pile-up of dislocations should be noted.

A part of the experimental strain-controlled triangular waveform recorded using the LVDT is shown in Fig. 5.3a. Clearly, the control system of the machine was able to impose a triangular loading cycle. Figure 5.3b shows hysteresis loops corresponding to cycles 1 and 300. It shows softening during the tensile part of the cyclic loading. The extent of such change in stress is relatively less in the compressive part of the loading cycle.

To get a complete picture of softening behavior of the alloy during cyclic deformation, peak stresses during tension and compression parts of the loading cycles were plotted as a function of number of cycles as shown in Fig. 5.4a. Clearly, the alloy in this loading conditions exhibited cyclic softening right from the start of cyclic deformation. The sample fractured after 526 cycles. For the sample tested at 0.2% total strain amplitude, the cyclic softening was noted continuously after 325 cycles of cyclic deformation (softening curve not shown here). In this case, the fracture of the sample took place at 17,416 cycles. The dependence of creep-fatigue life on strain amplitude is shown in Fig. 5.4b. It also shows creep-fatigue life of SS316 tested under very similar conditions [6]. Due to very limited testing and availability of creep-fatigue data for the Alloy 709, at present, we are not able to make any conclusions based on this comparison.
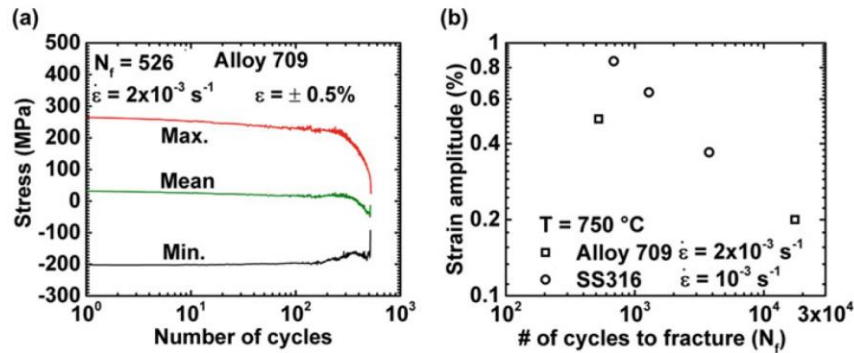
Fig. 5.4 (**a**) Variation in peak and mean stresses as number of cycle during creep-fatigue test and (**b**) plot showing dependence of creep-fatigue life on strain amplitude for the Alloy 709 and its comparison with SS316 [6]
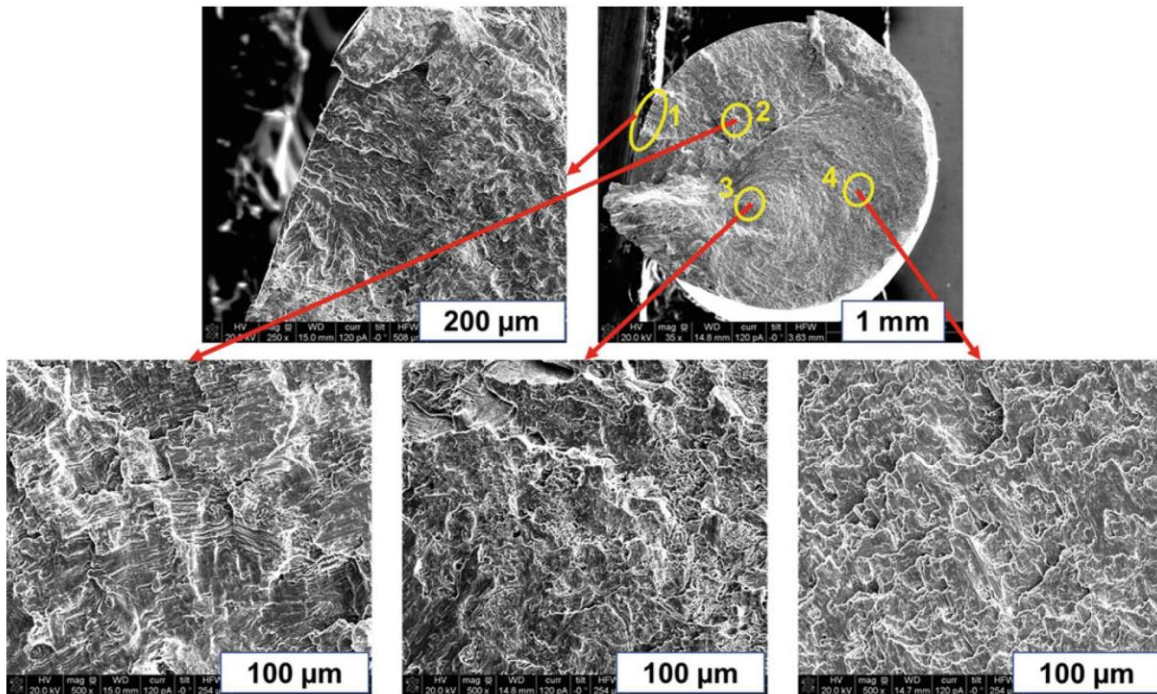
Fig. 5.5 Fractographs for the sample tested under 0.5% strain amplitude at 750 °C showing different microscopic features representative of different modes of failure during creep-fatigue testing

5.3.2 Fractographs and Micrographs of the Deformed Alloy

The fractographs corresponding to the sample tested at 0.5% total strain amplitude are shown in Fig. 5.5. The high magnification fractograph corresponding to region 1 in Fig. 5.5 shows one of possibly multiple crack nucleation sites. The high magnification fractograph of region 2 shows striations indicative of fatigue crack propagation. The fractograph taken from region 4 was representative of ductile failure under shear stress. The dimple feature of the fractograph captured from region 3 was reminiscent of ductile fracture during uniaxial tensile testing. Such dimpled features on the fractured surface are commonly observed during the last stage of pure fatigue test.
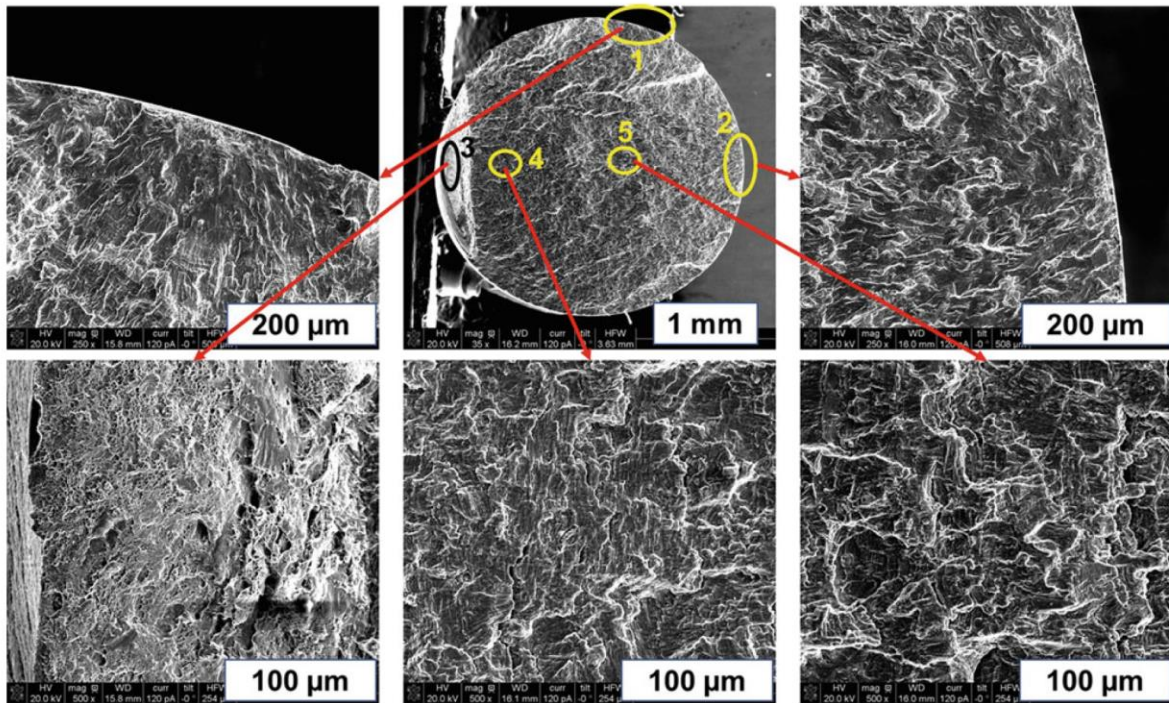
Fig. 5.6 The fractographs obtained for the sample tested under 0.2% strain amplitude at 750 °C showing striations on most of the fractured surface
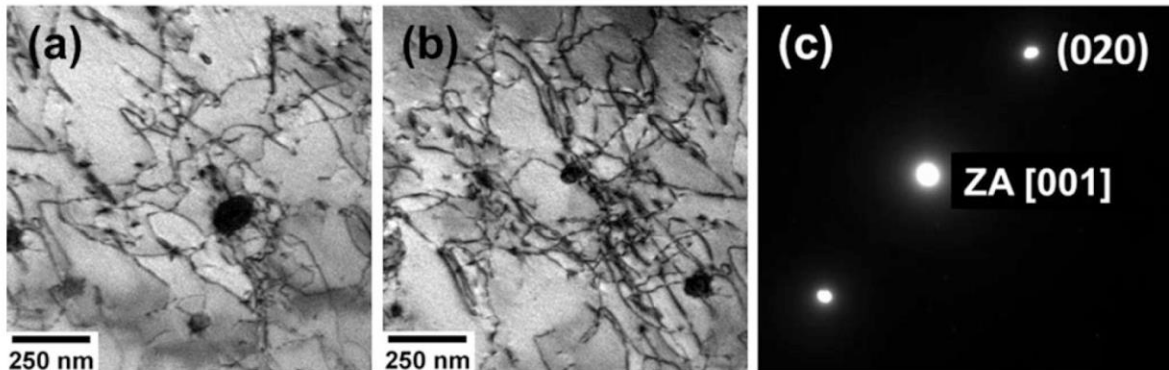

Fig. 5.7 (**a**, **b**) TEM micrographs of the sample deformed at 0.5% total strain amplitude and (**c**) selected area diffraction corresponding to [001] zone axis

The fractographs obtained for the sample tested at 0.2% total strain amplitude is shown in Fig. 5.6 and regions 1 and 2 show probable crack nucleation sites. The fractographs corresponding to regions 4 and 5 showed presence of striations indicative of fatigue crack propagation. Unlike the sample tested at 0.5% strain amplitude, more than 90% of the fractured surface contained fatigue striations. The dimpled features were only observed in region 3 of the sample. The presence of striations on the fractured surface was indicative of fatigue as the dominant mode of deformation in this case.

The TEM micrographs of the deformed samples (0.5% strain amplitude) are shown in Fig. 5.7. The images were taken at [001] zone axis. These micrographs are representative of lightly deformed alloys and loosely defined sub-grains should be noted in the micrographs revealing creep dominance.

5.4   Summary and Conclusion

We have carried out creep-fatigue tests of the Alloy 709 at 0.2% and 0.5% strain amplitudes in strain-controlled mode at 750 °C. The sample fractured at 17,416 cycles at 0.2% strain amplitude whereas the number of cycles to fracture decreased to 526 cycles at 0.5% strain amplitude. The microscopy of the deformed samples indicated that fatigue might have been the dominant deformation mode at 0.2% strain amplitude whereas at 0.5% strain amplitude, both fatigue and creep might have interacted.

The future work involves repeating the tests being reported here in addition to carrying out creep-fatigue tests at different frequencies, strain amplitudes, and temperatures with and without hold times. In addition to SEM and TEM, electron backscattered diffraction will be utilized for microstructural characterization of the samples following deformation.

References

1. Zinkle, S.J., Busby, J.T.: Structural materials for fission & fusion energy. Mater. Today. **12**, 12–19 (2009)
2. Zinkle, S.J., Was, G.S.: Materials challenges in nuclear energy. Acta Mater. **61**, 735–758 (2013)
3. Allen, T., Balbaud-Celerier, F., Asayama, T., Pouchon, M., Busby, J., Maloy, S., Park, J., Fazio, C., Dai, Y., Agostini, P.: Status Report on Structural Materials for Advanced Nuclear Systems. Organization for Economic Co-Operation and Development, France, NEA – 6409 (2013)
4. Dieter, G.E.: Mechanical Metallurgy, 3rd edn. McGraw-Hill, New York (1986)
5. Rodriguez, P., Rao, K.B.S.: Nucleation and growth of cracks and cavities under creep-fatigue interaction. Prog. Mater. Sci. **37**, 403–480 (1993)
6. Yagi, K., Kanemaru, O., Kubo, K., Tanaka, C.: Life prediction of 316 stainless steel under creep-fatigue loading. Fatigue Fract. Eng. Mater. Struct. **9**, 395–408 (1987)